

**PREPARATION AND CHARACTERIZATION OF DOPED
LEAD ZIRCONATE TITANATE $\text{Pb}(\text{Zr}_x\text{Ti}_{1-x})\text{O}_3$ FILMS**

by

Jhing-Fang Chang

Thesis Submitted to the Faculty of the
Virginia Polytechnic Institute and State University
in partial fulfillment of the requirement for the degree of

MASTER OF SCIENCE

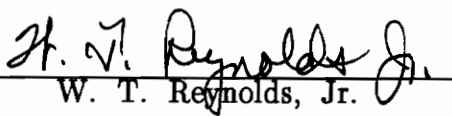
in

Materials Science and Engineering

APPROVED:



S. B. Desu, Chairman



W. T. Reynolds, Jr.



D. F. Cox

August, 1992

Blacksburg, Virginia

C.2

LD
5655
V855
1992
C524
C.2

**PREPARATION AND CHARACTERIZATION OF DOPED
LEAD ZIRCONATE TITANATE $\text{Pb}(\text{Zr}_x\text{Ti}_{1-x})\text{O}_3$ FILMS**

by

Jhing-Fang Chang

Committee Chairman: Seshu B. Desu

Materials Science and Engineering

(ABSTRACT)

Undoped and doped $\text{Pb}(\text{Zr}_x\text{Ti}_{1-x})\text{O}_3$, i. e. PZT, ferroelectric thin films were prepared by chemical solution deposition and spin-coating method. The precursors for making the undoped PZT films were derived from lead acetate, zirconium n-propoxide, and titanium iso-propoxide. In addition, lanthanum acetylacetonate, neodymium acetate, and niobium ethoxide were introduced into the precursor solution to accomplish doping of the corresponding elements. Both doped and undoped PZT films were coated onto Pt/Ti/SiO₂/Si, RuO_x and single-crystal sapphire substrates of various thickness and annealed at a range of temperatures and times. The effects of dopants were studied in terms of the Curie temperature, crystal distortion, transformation temperature, microstructure, optical properties, and electrical properties. In addition to the dopant effect, the effects of substrates were also investigated with regard to crystallization and preferred orientation.

The Curie temperature of the doped and undoped PZT films was determined

by in-situ hot-stage transmission electron microscope (TEM) and compared with those of bulk ceramics. Lattice distortion and phase transformation were determined by x-ray diffraction (XRD). Microstructure of the films was characterized by using optical microscopy, scanning electron microscopy (SEM), and scanning transmission electron microscopy (STEM). Optical properties were characterized by a UV-VIS-NIR scanning spectrophotometer and electrical properties and fatigue testing were measured on a standardized RT66A using a Virtual-Ground circuit.

It was observed that the addition of Nd and La dopants tends to enhance perovskite phase formation and improve electrical properties of PZT films. Higher refractive indices in La and Nd-doped PZT films imply that packing densities of PZT films are improved by adding dopants. Furthermore, the lower leakage currents and improved fatigue properties in PZT films were also observed by the addition of Nb dopants.

ACKNOWLEDGEMENT

I would like to express my greatest appreciation to Dr. Seshu B. Desu for his guidance and patience. Appreciation is also expressed to Dr. William T. Reynolds, Jr. and Dr. David F. Cox for their reviewing this thesis and suggestions. Special thanks to the all members of the thin film laboratory in the Department of Materials Science and Engineering, especially Mr. Chien-Hsiung Peng and Mr. Chi Kong Kwok, for their friendship and assistance. Finally, I would like express my deepest thanks to my family and friends for their mental support and encouragement.

Table of Contents

Chapter 1: Introduction.....	1
1.1 Objectives.....	6
Chapter 2: Literature Review.....	7
2.1 PZT Crystal Structure.....	7
2.1.1 Perovskite Structure.....	7
2.1.2 PZT Phase Diagram.....	11
2.2 Ferroelectric Properties.....	13
2.2.1 Ferroelectric Hysteresis loop.....	14
2.2.2 Domain Structure.....	17
2.2.3 Fatigue Properties.....	19
2.3 Compositional Modifications.....	20
2.4 Chemical Solution Deposition: MOD and Sol–Gel Process.....	27
2.4.1 Advantages.....	27
2.4.2 Selections of Precursors.....	28
2.4.3 Film Formation.....	31
2.4.4 Structure Development.....	33
2.4.4.1 Pyrochlore to Perovskite Phase Transformation.....	35
Chapter 3: Experimental Procedure.....	36
3.1 Preparation and of Precursor Solution.....	36

3.2	Characterization of Precursor Solution.....	40
3.3	Preparation of Thin Film and TEM Specimen.....	41
3.4	Thin Film Characterization.....	44
3.4.1	General.....	44
3.4.2	Optical Property Measurement.....	45
3.4.3	Electrical Property Measurement.....	46
3.5	Preparation and Characterization of Bulk Ceramics.....	46
Chapter 4: Results and Discussion.....		49
4.1	Precursor Characterization.....	49
4.2	Composition.....	56
4.3	Microstructure.....	61
4.4	Domain Structure.....	70
4.5	Dopant Effects on Curie Temperature and Crystal Tetragonality.....	72
4.5.1	Effect on Curie Temperature.....	72
4.5.2	Effect on Crystal Tetragonality.....	76
4.6	Optical Properties.....	78
4.7	Electrical Properties.....	82
4.7.1	Effect of Processing Conditions.....	82
4.7.1.1	Effect of Annealing Temperature.....	82
4.7.1.2	Effect of Film Thickness.....	91
4.7.1.3	Effect of Electrode.....	91
4.7.2	Dopant effects.....	95
4.7.2.1	Effect on Polarization and Coercive Field.....	95

4.7.2.2	Effect on Leakage Current.....	99
4.7.2.3	Effect on Fatigue Property.....	103
4.8	Substrate Effects.....	106
4.8.1	Effect on Preferred Orientation.....	107
4.8.2	Effect on Microstructure.....	107
4.8.3	Effect on Transformation Temperature.....	112
Chapter 5: Summary.....		114
Appendix A.....		116
Appendix B.....		119
References.....		120
Vita.....		129

List of Figures

Figure 2.1	(a) A cubic ABO_3 perovskite unit cell for PZT materials and (b) a three-dimensional network of BO_6 - octahedra.....8
Figure 2.2	Classification of the perovskite $A^{2+}B^{4+}O_3^{2-}$ compounds according to the constituent ionic radii.....10
Figure 2.3	Phase diagram of the $PbTiO_3$ – $PbZrO_3$12
Figure 2.4	The hysteresis loops of (a) polarization versus electric field and (b) displacement charge versus electric field in ferroelectric materials.16
Figure 2.5	Room temperature phase diagram of PLZT system.....24
Figure 2.6	A simple model of the structure development in MOD PZT films.34
Figure 3.1	A flow chart for the preparation of undoped and doped PZT films by MOD process.....31
Figure 3.2	A flow chart for the preparation of undoped, PLZT and PNZT precursor solutions by the MOD process.....38
Figure 3.3	Film thickness as a function of molar concentration of the solution.42
Figure 3.4	Film thickness as a function of spin speed.....43
Figure 3.5	An alternating square wave pulse used for fatigue measurements.47
Figure 4.1	Thermogravimetric analysis of the PZT (50/50), 0.5 M, precursor

	solution heated at 10 ⁰ C/min (a) in air and (b) in nitrogen.....	50
Figure 4.2	A differential scanning calorimetry curve of the PZT (50/50) precursor solution.....	52
Figure 4.3	The X-ray diffraction patterns of the MOD PZT (50/50) powders heated at 411 ⁰ C, 486 ⁰ C and 650 ⁰ C.....	54
Figure 4.4	The structure change as a function of temperature for the PZT (50/50).....	55
Figure 4.5	STEM microrgraphs of the PNZT (1/50/50) film on a Pt substrate, annealed at 700 ⁰ C for 1 hour: (a) a combination image obtained from both backscattering electrons and secondary electrons and (b) a micrograph obtained from backscattering electrons.....	60
Figure 4.6	Typical XRD patterns of undoped PZT films on sapphire substrates annealed at the temperatures ranged from 300 to 700 ⁰ C.	63
Figure 4.7	The average grain size as a function of dopant concentration in PLZT and PNZT thin films on sapphire substrates.....	64
Figure 4.8	Transmission electron micrographs of the MOD PNZT (2/50/50) films, annealed at 650 ⁰ C for 15 minutes, show the coexistence of pyrochlore and perovskite phases: (a) bright field image, (b) selected area diffraction patterns of perovskite and (c) pyrochlore phases.....	66
Figure 4.9	A transmission electron micrograph of PNZT (2/50/50) film, annealed at 500 ⁰ C for 15 minutes.....	68
Figure 4.10	Microstructures of PZT (50/50) films on sapphire substrates	

	annealed at 650°C for 30 minutes in (a) a box and (b) a tube furnace.....	69
Figure 4.11	The domain structure of (a) PZT (50/50), (b) PLZT (2/50/50) and (c) PNZT (2/50/50) thin foils.....	71
Figure 4.12	Transmission electron micrographs of the PZT (50/50) thin foil showing the presence of domain structure at (a) 25°C and (b) 305°C, the disappearance at (c) 390°C upon heating, and (d) the reappearance at (d) 25°C after cooling.....	73
Figure 4.13	The crystal tetragonality factor of PLZT and PNZT thin foils at room temperature, determined from electron diffraction patterns, as a function of dopant concentration.....	77
Figure 4.14	The linear relationship between the Curie temperature and the crystal tetragonality factor for PLZT and PNZT thin foils determined by hot-stage TEM.....	79
Figure 4.15	The crystal tetragonality factor as a function of temperature for PLZT thin foils determined from electron diffraction patterns.....	80
Figure 4.16	The refractive index of PLZT and PNZT films as a function of dopant concentration.....	81
Figure 4.17	Comparison of hysteresis loops for PZT films annealed at 550°C and 575°C.....	85
Figure 4.18	Remanent polarization as function of annealing temperature for PZT films on Pt electrodes.....	86
Figure 4.19	Comparison of remanent polarization as function of applied voltage for PZT films annealed at 600°C and 650°C.....	87

Figure 4.20	Comparison of coercive field as a function of applied voltage for PZT films annealed at 600°C and 650°C.....	88
Figure 4.21	Log–log plot of current as function of voltage for PZT films.....	90
Figure 4.22	Polarization as a function of film thickness for PZT films.....	92
Figure 4.23	Coercive field as a function of film thickness for PZT films.....	93
Figure 4.24	Log–log plot of coercive field as a function of film thickness for PZT films.....	94
Figure 4.25	Comparison of remanent polarization as a function of applied voltage for PZT films on RuO _x and Pt electrodes.....	96
Figure 4.26	Comparison of coercive field as a function of applied voltage for PZT films on RuO _x and Pt electrodes.....	97
Figure 4.27	Log–log plot of leakage current as a function of applied voltage for PZT films on RuO _x and Pt electrodes annealed at 650°C.....	98
Figure 4.28	Comparison of hysteresis loops in PLZT and PZT films annealed at 550°C.....	100
Figure 4.29	Log–log plot of leakage current as a function of applied voltage for PZT and Nb–doped PZT films.....	102
Figure 4.30	Comparison of hysteresis loops before and after fatigue testing for (a) undoped and (b) Nb–doped PZT films on Pt electrodes.....	104
Figure 4.31	Comparison of fatigue properties of undoped and Nb–doped PZT films on Pt electrodes.....	105
Figure 4.32	{100}/{110} x–ray peak height ratio for PNZT (1/50/50) films on Pt substrate annealed at (a) 500°C, (b) 550°C, (c) 600°C, and (d) 700°C for 1 hour, respectively.....	109

Figure 4.33 Typical microstructure of PNZT (1/50/50) films subjected to a final heat treatment at 700°C for 1 hour (a) on Pt substrate with a combination photograph of scanning electron and backscattering electron images and (b) on sapphire substrate with a SEM photograph.....110

Figure 4.34 X-ray diffraction patterns of PNZT (1/50/50) films, on (a) sapphire and (b) Pt substrates.....111

Figure 4.35 X-ray diffraction patterns of PNZT (1/50/50) films, annealed at 500°C for 1 hour, on (a) sapphire and (b) Pt substrates.....113

List of Tables

Table 2.1	Radii of substitutions and dopants in PZT materials.....	22
Table 2.2	Chemical solution deposition method for PZT and PZT-related thin films.....	30
Table 3.1	Selective properties of starting materials.....	39
Table 4.1	The bulk compositions of PLZT and PNZT films on sapphire substrates analyzed by EPMA along with the compositions of corresponding precursor solutions.....	57
Table 4.2	The results of EPMA for the PZT (50/50) films on sapphire substrates at different heat treatment conditions.....	59
Table 4.3	Comparison of Curie temperature of PLZT and PNZT thin foils obtained by hot-stage TEM method with those of PLZT bulk ceramics.....	75
Table 4.4	Packing densities of undoped and doped PZT films.....	83
Table 4.5	A summary of electrical properties for PLZT films.....	101
Table 4.6	{100}/{110} x-ray peak height ratio for PLZT and PNZT films heat treated at 700°C for 1 hour on both Pt and sapphire substrates.....	108

Chapter 1: INTRODUCTION

Lead zirconate titanate (PZT) thin films have been extensively investigated and used for fabricating many devices including ferroelectric nonvolatile memories [1–2], optical display devices, optical modulators, optical image storage devices, and optical switches [3] primarily due to their remarkable ferroelectric, piezoelectric, pyroelectric, and electrooptic properties [4]. Recently, PZT thin films have received a lot of attention for the fabrication of nonvolatile memory devices owing to their potential for exhibiting high density, high access speed, low operating voltage, nonvolatility, and radiation hardness. Especially, with favorable properties like high permittivity and large remanent polarization PZT is also a potential candidate for very large-scale integrated (VLSI) and ultra large-scale integrated (ULSI) devices.

A number of techniques such as thermal evaporation, electron beam evaporation, rf sputtering, magnetron sputtering, ion beam sputtering, laser ablation, pulsed laser deposition, metalorganic chemical vapor deposition (MOCVD), sol-gel processing, and metalorganic decomposition (MOD) have been investigated for the deposition of PZT thin films [5–13]. There are advantages and disadvantages associated with each technique. The evaporation methods provide high deposition rates and film uniformity; however, stoichiometry control of multicomponent films is difficult due to the different vapor pressures of the components. For laser ablation process, uniformity is a significant issue. Sputtering, CVD, and chemical solution deposition are some of the promising

techniques which can produce good quality ferroelectric thin films and can be scaled and applied for industrial applications. There are some problems associated with sputtering such as film damaged by the ions, stresses in resultant film, and poor step coverage of the film. MOCVD is limited by the availability of precursor materials. Of all the deposition techniques proposed, chemical solution deposition (e.g. sol-gel process and MOD) is one of the simplest techniques to prepare pure stoichiometric thin films of multicomponent oxides and therefore is used in this study.

The chemical solution deposition consists of following steps [14–15]: (1) preparation of metalorganic precursor solution, (2) hydrolysis (only for sol-gel), (3) deposition onto a substrate by spin or dip-coating method, (4) removal of solvent and pyrolysis, and (5) crystallization of the films. The precursor solution used for the chemical solution deposition is prepared by dissolving metalorganic compounds in a suitable organic solvent. Since the starting materials are mixed at molecular level, it can be expected that the compound formation temperatures and times can be significantly reduced. Furthermore, higher levels of compositional homogeneity can be obtained from this technique. Additionally, trace elements, which are important in adjusting the microstructure and improving the properties of the films, can be easily introduced into the solution by adding the corresponding metalorganic compounds. Therefore, ease of compositional control, easy introduction of dopants, homogeneity at molecular level, and short processing cycle are some advantages provided by the chemical solution deposition over the other thin film deposition techniques. Furthermore, the films prepared by chemical solution deposition have displayed ferroelectric and optical properties comparable to those of bulk ceramics

[16–17]. In fact, recent work on the PZT films made by sol–gel processing in conjunction with novel ceramic electrodes have exhibited fatigue–free behavior with polarization reversal up to 10^{12} cycles [18]. In spite of providing the fast and easy way to investigate the interrelationship between processing, microstructure and property of the films, the chemical solution deposition has not been commercialized for any electronic films. One of primary problems is the film cracking during film formation. To solve the problem of cracking, many methods such as the use of surfactants, drying control chemical additives, and chelating organic ligands have been suggested [19]. The microstructure and ferroelectric properties of the PZT films with good reproducibility have been investigated earlier [20]. The crystal structure and the ferroelectric properties of PZT materials depend strongly on Zr/Ti ratio. The composition near morphotropic boundary (MPB), with Zr/Ti ratio of 53/47, is especially important because most of the interesting properties are optimized along it; e.g. dielectric constant, remanent polarization, and piezoelectric coefficient increase to their maximum values [21]. For this reason, the composition of PZT thin films in this study was chosen to be near MPB. Although PZT thin films fabricated by the chemical solution deposition are considerable interest due to the short processing cycle, dopant effects on PZT film properties have not been investigated.

For PZT bulk ceramics, most studies involved dopant effects were confined to two types of dopants [22]. Type one dopants act as acceptors and are characterized by an increase in the coercive field, electrical and mechanical quality factors of PZT ceramics. Type two dopants are donors e.g. lanthanides or rare earths, La^{3+} , Nd^{3+} and Nb^{5+} and tend to increase the dielectric constant and reduce

the coercive field. The resulting effects of dopants can be explained on the basis of valency compensation in the perovskite lattice. In conclusion, donor doped PZT materials are desirable for ferroelectric memory applications due to their lower coercive field, higher resistivity, higher dielectric constant and lower dielectric aging rates compared to undoped PZT materials.

Among donor dopants, lanthanides are unique in producing desirable properties, such as increased squareness of the hysteresis loop, decreased coercive field and increased dielectric constant. La^{3+} is known to promote uniform grain growth and homogeneous densification of a single phase, pore-free microstructure in PZT ceramics [23]. Further, the addition of Nd^{3+} ions in PZT ceramics were found to increase both the dielectric constant, inhibit the grain growth due to impeding the grain boundary mobility, and enhance the sintering process [24]. For PZT films, both Carim et al. [25] and Griswold et al. [26] have shown that the addition of niobium in PZT films tends to improve ferroelectric properties resulting from the densification of structure. Scott et al. [27] has also found that adding yttrium can reduce space charge and leakage current in PZT films. Most recently, Melnick et al. [28] indicated that an anomalous fatigue free behavior has been seen in some zinc doped PZT thin films. For these reasons, donor (e.g. La, Nd and Nb) doped PZT thin films were investigated in this study.

It has been observed that the electrical degradations of the PZT films are strongly correlated to domain size and structure [22]. Several investigators [29–30] have reported that the strain, due to the phase transformation from a cubic to a tetragonal phase upon cooling below the Curie temperature, was accommodated by

the twin-like domain structure. Therefore, it is interesting to study the effect of dopant concentration on lattice distortion and domain structure in the films. A simpler TEM specimen fabrication method was used in the present study for the observation of the ferroelectric domains of the MOD derived films [31]. Utilize this method, some side effects such as induced stress and surface damage resulting from the conventional specimen preparation (e.g. chemical etching, replica techniques and mechanically ion thinning) can be eliminated. Additionally, imaging the ferroelectric domains in these specimens was not difficult as long as the specimens were tilted to the right orientation.

In this study, a modified version of the sol-gel process developed by Budd [32] is used. The process parameters such as thermal processing conditions on the microstructure and ferroelectric properties of the films were studied and optimized in order to meet the requirements for ferroelectric memory applications. For the memory applications, Parker et al. [33] have suggested the desirable parameters of ferroelectric materials are: (1) compositions which do not change phase in the operating temperature range, (2) films with smaller grain size, (3) compositions with near cubic phase, i.e. smaller lattice distortion and lower internal strain, and (4) careful choice of electrode materials. Composition modifications such as doping of the PZT films provides one of the important methods to meet these requirements. Therefore, the effect of dopants were studied in terms of the Curie temperature, crystal distortion, transformation, microstructure, optical properties, ferroelectric properties, and fatigue properties. Additionally, the effect of substrates was also investigated as with regard to crystallization and preferred orientation.

1.1 Objectives

The primary objective of this study was to investigate the effects of donor dopants on PZT thin films. Three aspects of the dopant effects on the characteristics of the PZT thin films were emphasized:

- (1) To study the effects of donor dopants on the phase transformation of PZT films. The phase transformation of the MOD PZT films with increasing annealing temperature was determined in the order of amorphous, pyrochlore and finally perovskite phase. The desirable phase used for the ferroelectric memory applications was studied and found to be the perovskite. Therefore, the effects of donor dopants on the transformation temperatures from pyrochlore to perovskite phase was investigated.
- (2) To understand the effects of donor dopants on the Curie temperature, lattice distortion and microstructure of PZT films. In-situ experiments on transmission electron microscopy (TEM) were developed in this study to determine the Curie temperature. A nondestructive optical method was conducted to study the packing density of the films.
- (3) To understand the effects of donor dopants on the properties of PZT films such as polarization, coercive field, leakage current, and fatigue properties.

To accomplish the objectives of this study, the MOD process was used to study the interrelationship between structure, processing and properties of the films because it provides the easy introduction of dopants and the easy route to prepare doped PZT thin films.

Chapter 2: LITERATURE REVIEW

2.1 PZT Crystal Structure

2.1.1 Perovskite Structure

Ferroelectric PZT materials exhibit a perovskite type structure, which has the general chemical formula ABO_3 , where A represents a cation with a larger ionic radius, B a cation with a smaller ionic radius, and O is oxygen. Figure 2.1(a) shows a cubic ABO_3 perovskite unit cell for PZT materials. As shown in the figure, the Pb ions occupies A sites at the cubic unit cell corners, the Zr or Ti occupy the B sites at or near the cell centers, and O is located in the cell faces. Most of the ferroelectric materials with perovskite structure are compounds with either $A^{2+}B^{4+}O_3^{2-}$ or $A^{1+}B^{5+}O_3^{2-}$ formula. A perovskite structure is essentially a three-dimensional network of BO_6 - octahedra as shown in Figure 2.1(b). Since the A site cation is coordinated with 12 oxygen ions and the B site cation with 6, the A cation is normally found to be larger than the B cation [34].

One of the primary requirements for the stability of perovskite structure is that the ionic radii difference between the cations and oxygen should be within certain limits. This limit can be described by a tolerance factor (t), which is given by the following equation [35]:

$$t = (R_a + R_o) / \sqrt{2} (R_b + R_o) \quad (2.1)$$

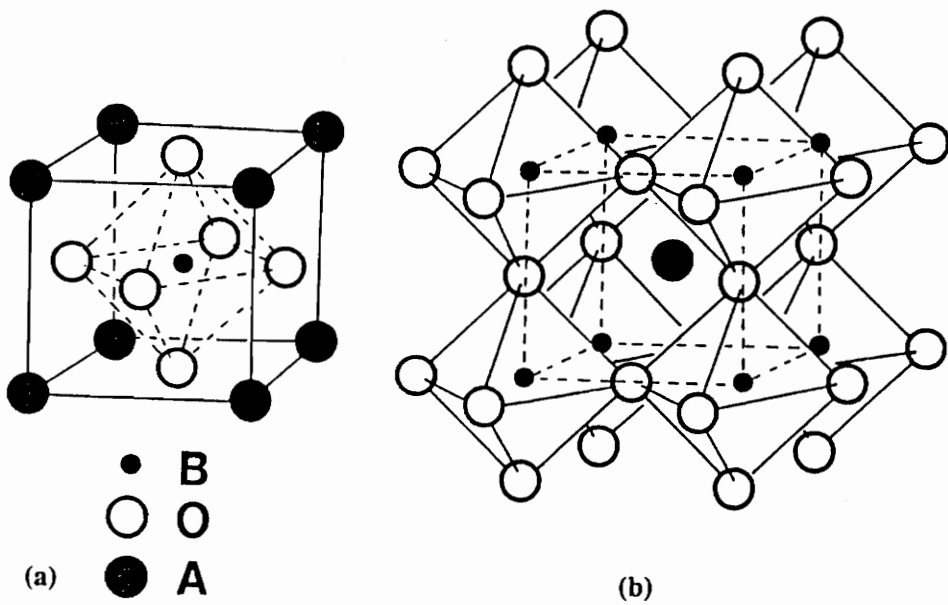


Figure 2.1(a) a cubic ABO_3 perovskite unit cell for PZT materials and (b) a three-dimensional network of BO_6 -octahedra [34].

where R_a and R_b are the ionic radii of cations of A and B, respectively, and R_o is the ionic radius of oxygen. In general, to form a stable perovskite structure, the requirement is that t should be in the range of $0.9 < t < 1.1$ [35]. Besides the ionic radii, other factors, such as bond character, bond strength and polarizability, also influence the stability of perovskite structure. The chemical bonding strength is proportional to the value of electronegativity difference between the cations and anions. The electronegativity difference is expressed by the following equation:

$$(X_{a-o} + X_{b-o})/2 \quad (2.2)$$

where X_{a-o} is electronegativity difference between the A-site cation and oxygen, and X_{b-o} is electronegativity difference between the B-site cation and oxygen. It has been shown that ideal perovskite compounds have a tolerance factor $t \approx 1$ and a high electronegativity difference; that is, strong ionic bonding. The classification of $A^{2+}B^{4+}O_3^{2-}$ compounds by considering the polarizability of the A^{2+} ions and radii of B^{4+} ions is shown in Figure 2.2 [22]. Among these compounds, $PbZrO_3$ was reported as an antiferroelectric material with a pseudo-tetragonal phase, whereas $PbTiO_3$ a ferroelectric material with a tetragonal phase. Due to the difference in their relative electronic bond strength, it is expected that the ferroelectric perovskite phase in PZT materials can be suppressed by substituting La^{3+} or Nd^{3+} for Pb^{2+} . In other words, the addition of La or Nd will tend to stabilize the paraelectric, cubic and antiferroelectric phase in the PLZT or PNZT systems. Consequently, Curie temperature of PLZT or PNZT should decrease with increasing the La or Nd concentration.

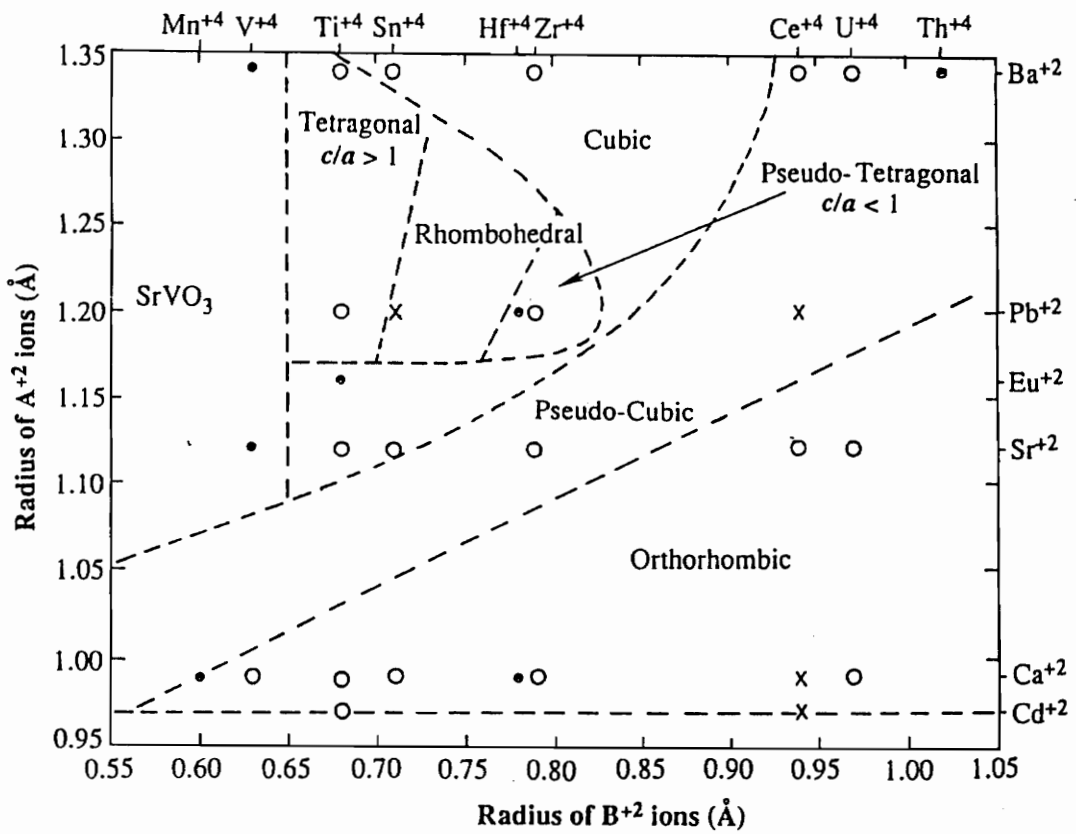


Figure 2.2 Classification of the perovskite $A^{2+}B^{4+}O_3^{2-}$ compounds according to the constituent ionic radii [22].

2.1.2 PZT Phase Diagram

Jaffe et al. [21] reported the discovery of the ferroelectric ceramic $\text{Pb}(\text{Zr}_x\text{Ti}_{1-x})\text{O}_3$ (PZT). The crystal structure and the ferroelectric property of PZT materials was found to depend strongly on Zr/Ti ratio. As seen from the PZT phase diagram shown in Figure 2.3, the Curie temperature increases with increasing Ti content to about 390°C for PZT (52/48) and about 490°C for PbTiO_3 . When below the Curie temperature, the structure of the PZT phase is rhombohedral in the zirconium rich region whereas it is tetragonal in the titanium rich region. The adjacent boundary corresponding to the transition from tetragonal to rhombohedral phase is called the morphotropic boundary (MPB), whose composition is around $x = 0.53$. Compositions located on the tetragonal side of the phase boundary are usually "hard" with high coercive field (E_c), whereas those on the rhombohedral side are "soft" with low E_c . The polarization axis of tetragonal PZT is parallel to [001] axis while that of rhombohedral one is parallel to the [111] axis. The composition near MPB is especially important because most of the properties of interest are optimized along MPB; e.g. dielectric constant, remanent polarization, and piezoelectric coefficient increase to their maximum values. Bulk PZT ceramics have large remanent polarization ($P_r = 40\text{--}50 \mu\text{C}/\text{cm}^2$) and reasonable coercive field ($E_c = 20\text{--}30 \text{ kV}/\text{cm}$) on MPB. The lattice parameters of PZT ceramics near MPB (Zr/Ti = 52/48) have been determined as the following [36]:

$$a_0 = 4.036 \text{ \AA}$$

$$c_0 = 4.146 \text{ \AA}$$

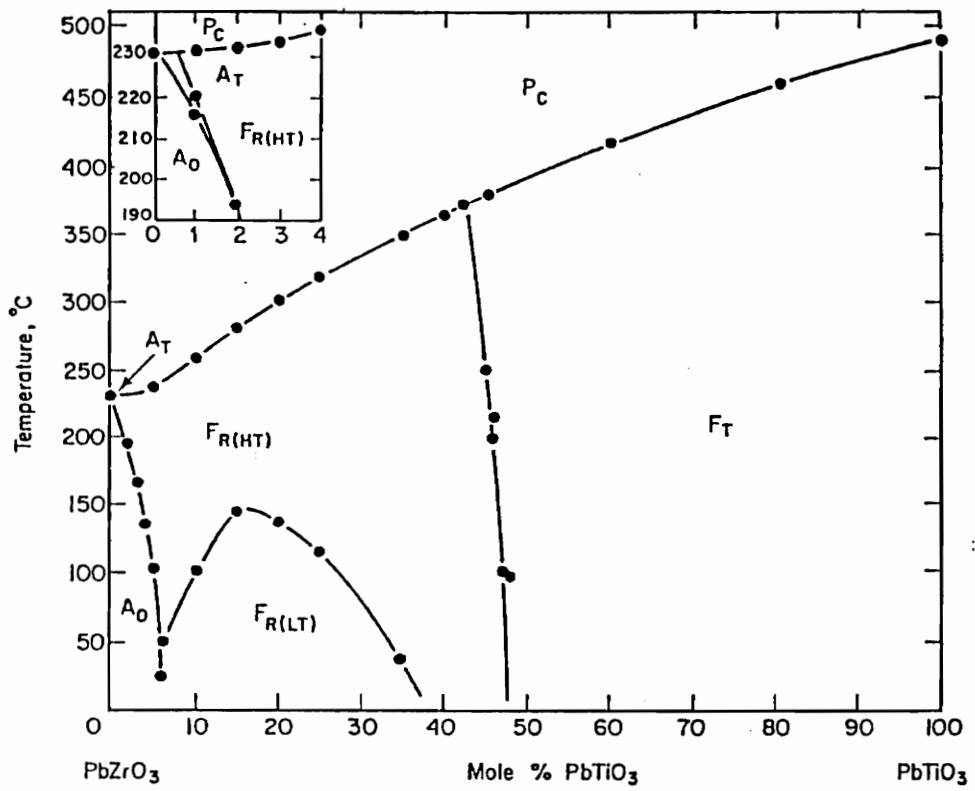


Figure 2.3 Phase diagram of the PbTiO_3 - PbZrO_3 [21].

Therefore, the lattice distortion (crystal tetragonality, c/a ratio) of PZT ceramics is 1.028, which is much smaller compared to that of PbTiO_3 (1.064).

2.2 Ferroelectric Properties

Ferroelectric materials exhibit a number of interesting properties including mechanical, optical, piezoelectric (stress/strain dependent polarization), pyroelectric (temperature dependent polarization), electro-optic (electric field dependent optical birefringence), and ferroelectric (electric field dependent polarization) properties. A ferroelectric model has been discussed in detail for the case of barium titanate (BaTiO_3). For ferroelectric materials, the relationship between the polarization (P) and the local electric field (E') is given by [34]:

$$P = \alpha N E' \quad (2.3)$$

where N is the number of dipoles per unit volume and α the polarizability.

In dielectrics, there are four primary mechanisms of polarization which contribute to α : (1) electron polarization, due to the shift of valence electron cloud of the ions within the material with respect to the positive nucleus, (2) atomic or ionic polarization due to the displacement of positive and negative ions with respect to each other, (3) dipole or orientation polarization which involves the perturbation of the thermal motion of ionic or molecular dipoles, producing a net dipolar orientation in the direction of the applied field, (4) interfacial or space charge polarization, which occurs when mobile charge carriers are impeded by a physical

barrier that inhibits charge migration. Therefore, the total polarization of the dielectrics can be represented as the sum of these contributions:

$$P = P_e + P_a + P_d + P_i \quad (2.4)$$

where P_e = electronic polarization
 P_a = atomic or ionic polarization
 P_d = dipole or orientation polarization
 P_i = interfacial or space charge polarization

For ferroelectric materials, P_e , P_a and P_d are major contributors to the dielectric constant. At the Curie temperature, the thermal energy is sufficient to impart freedom of oscillation of ions and electrons to reach a maximum; therefore, P_e and P_a increase with increasing temperature and give rise to a maximum dielectric constant and a minimum dielectric loss at the Curie temperature. At room temperature (or below the Curie temperature), P_d is especially important because the spontaneous alignment of dipoles, produced by the displacement of Zr^{4+} or Ti^{4+} ion between the two equivalent equilibrium positions, gives rise to the nonlinear polarization behavior. The dipole polarization is thus the dominant response of the ferroelectric materials when an external electric field is applied.

2.2.1 Ferroelectric Hysteresis Loop

One of the important characteristic of ferroelectric materials is the ferroelectric hysteresis loop, i.e. the response of the polarization (P) to the electric

field (E). The displacement charge density (D) is related to the polarization by

$$D = \epsilon_0 E + P \quad (2.5)$$

where ϵ_0 ($= 8.854 \times 10^{-12}$ F/m) is the permittivity (dielectric constant) of free space. Figures 2.4(a) and (b) show the hysteresis loops of polarization versus electric field and displacement charge versus electric field, respectively. Because $\epsilon_0 E \ll P$ in most ferroelectric materials, the D - E loop is similar to the P - E loop [33]. As shown in the figures, as the electric field increases, the negative domains, which have a polarization opposite to the direction of the field, get switched along the positive (field) direction. Later the polarization increases until all the domains are aligned in the positive direction and reach a state called the saturated polarization. As the electric field decreases, the polarization decreases but does not return to zero. When the field is reduced to zero, some of the domains remain aligned along the positive direction and the crystal exhibits a remanent polarization (P_r). The P_r in a crystal cannot be removed until a field is applied in the opposite or negative direction. The field required to reduce the polarization to zero is called the coercive field (E_c). As the field increases in the negative direction, the dipoles eventually completely align in this direction and the cycle is completed by reversing the field direction. When the direction of the applied field is opposite to the direction of polarization in a domain, the nucleation and growth of a new domain occurs in the old domain. The nucleation of a domain is a function of electric field and temperature. The growth of a domain is related to the motion of the domain wall, which is a function of the space charge, stress distribution, and defects in the ferroelectric material [22].

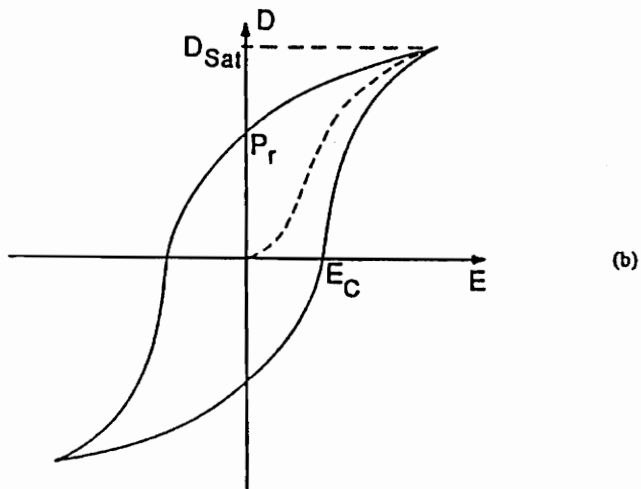
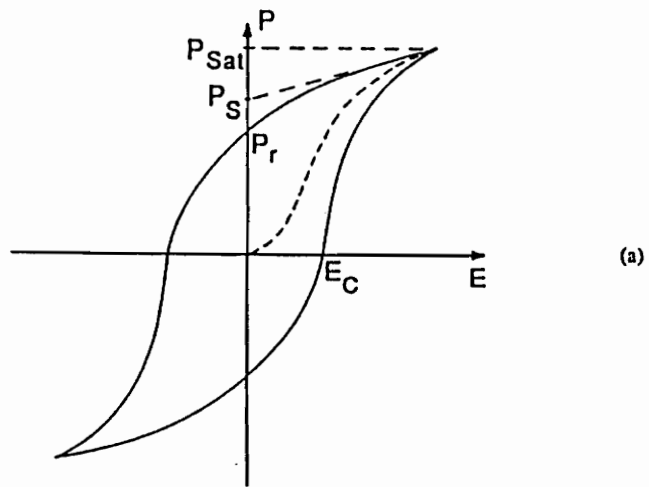


Figure 2.4 The hysteresis loops of (a) polarization versus electric field and (b) displacement charge versus electric field in ferroelectric materials [33].

2.2.2 Domain Structure

PZT materials have a cubic perovskite structure above its Curie temperature. However, when cooled below the Curie temperature they transform from cubic to tetragonal or rhombohedral structure depending upon the composition ratio of Zr/Ti. The ferroelectric tetragonal and rhombohedral phases occur simultaneously at the MPB corresponding to a Zr/Ti ratio of 53/47. The strain associated with this phase transformation is accommodated by the formation of twins. Also, each twin plate is believed to be a ferroelectric domain in the tetragonal structure. The domain structure in PZT materials has been studied by using SEM on etched bulk specimens and TEM replica or direct thin foils. For PZT bulk ceramics, both 90° and 180° domains are observed. The predominant 90° domains are observed to be deformation twins with displacement along $\langle 110 \rangle$ directions on $\{110\}$ planes, whereas the 180° domains orient in a zig-zag configuration along about $\langle 110 \rangle$ directions on $\{100\}$ planes [29–30]. However, for the PZT thin films, only the 90° domains are observed [38]. This phenomenon is explained by a model of ferroelectric domains proposed by Lucuta et al. [39–40]. In this model, crystallography of the transformation from paraelectric to ferroelectric phase in PZT is analyzed on the basis of the martensitic transformation theory, from which the habit-plane orientation of the twin-like domains can be predicted. This model predicts that due to the coexistence of a rhombohedral domain between two tetragonal 90° domains the required energy for the rotation of the polarization vector is smaller [41].

The structure of the domain walls in PZT is similar to that suggested for

BaTiO₃ [42]. The model states: (1) the domain wall has a finite thickness, (2) the structure of the wall region is considered as a noncentrosymmetric and two-dimensional distorted crystal, and (3) the rotation of the tetragonal distortion at the adjacent walls are opposite to each other.

Additionally, several other parameters found to significantly influence the formation of domains include: equilibrium domain thickness, domain wall energy, thickness of the thin foil, and critical grain size. Khachatryan [43] has derived an expression of the equilibrium domain width for 90° domains as following:

$$d = \left[\frac{\gamma_t D}{\lambda \epsilon_0^2} \right]^{0.5} \quad (2.6)$$

where D is the tetragonal inclusion width, which is equal to the foil thickness in the TEM studies (approximately 200 nm), λ the elastic modulus, ϵ_0 the transformation strain ($= \frac{(c/a)^2 - 1}{(c/a)^2}$), and γ_t the twin wall energy per unit area. The theoretical estimates for the wall thickness ranges from 1 to 4 nm. The measured domain width of PZT thin films ranges from few nm to 20 nm depending on the grain size and the deposition methods used [29,38].

Arlt et al. [42] have also proposed a model which estimates an approximate value for the elastic energy density per unit length W_s/h , stored in domain walls, by using the following relation:

$$\frac{W_s}{h} = \frac{C_{11} S_s^2 d^2}{64\pi} \quad (2.7)$$

where C_{11} is the average longitudinal elastic constant, S_s the spontaneous of crystal lattice, and d the domain wall thickness. Lucuta et al. have calculated the elastically stored energy in the domain walls for PZT with the composition near MPB to range from 0.6×10^{-3} to 2×10^{-3} erg/cm.

Goo et al. [29] have observed that in the ultrathin regions of the TEM foil (≤ 70 nm), i.e. the area near the free surfaces, the transformation strain required for twinning is relieved at the free surface. The reason is, the depolarization energy can no longer be minimized by the multidomain formation when the crystal thickness approaches the domain thickness. The other observation is that the ferroelectric domain formation requires a minimum grain size, below which the domain formation is energetically unfavorable [38,41]. The grain size is a function of surface energy, shear modulus, Young's modulus, and tetragonality of the materials. Demczyk et al. [38] have observed that the minimum grain size for twinning in La-doped lead titanate ceramics is 300 nm.

2.2.3 Fatigue Properties

One of the major limiting factors for the fabrication of ferroelectric memory applications is reliability issues. Fatigue is one of the important electrical degradation problems with regarded to the reliability issues. Generally, the fatigue occurs due to the decrease in polarization and the increase in coercive field. In addition, the following fatigue characteristics in ferroelectric memories have been reported [44,45]:

- (1) Fatigue decreases at high temperature and has a thermal activation

energy 0.4 to 1 eV.

(2) Thermally annealing PZT thin films makes the memories restore to its unfatigued state.

(3) Growth of conducting oxygen-deficient regions is observed.

(4) The films become conductive after they are sufficiently fatigued.

(5) Microcracking of the films is found after the films are fatigued and can be hindered by composition modifications.

Many mechanisms were proposed for fatigue in ferroelectric materials: (1) migration of impurities and vacancies to the highly stressed areas of domain walls, (2) accumulation of charges at grain boundaries, (3) ordering of defects in the bulk of the domain, and (4) nucleation of new domains at the existent stressed domain walls and defects. Although the exact nature of the fatigue mechanisms are not known, it is believed that the fatigue is strongly related to the film characteristics e.g. composition, stoichiometry, dopant, grain size and orientation, film thickness, and film stress. Therefore, the uniform composition control is also very important. Additionally, it has been found that the appropriate selection of electrode materials and dopants has significant improvements in the fatigue properties of PZT films [18,28,46].

2.3 Compositional Modifications

A review of different compositional modifications in PZT materials can be used as a guide to meet the requirements for the ferroelectric memory applications since most of the preferable parameters in PZT films such as smaller grain size,

lower internal strain, higher dielectric constant, lower coercive field, and reliability can be accomplished by the compositional modifications. The effects of the compositional modifications in PZT materials have been explored in depth and discussed in detail by Jaffe et al. [21]. Primarily, the methods used in compositional modifications of PZT materials include substitution and doping. The substitution involves the replacements of Pb^{2+} , Zr^{4+} or Ti^{4+} cation in the perovskite lattice by other cations with the same chemical valence and similar ionic radii as those of the replaced ions. Usually, the substitutional cation occupies the position of replaced cation in the perovskite structure and a substitutional solid solution is thus formed. The doping is accomplished by adding ions with different chemical valence from those of original ions or adding compounds with a chemical formula $\text{A}^+\text{B}^{5+}\text{O}_3^{2-}$ or $\text{A}^{3+}\text{B}^{3+}\text{O}_3^{2-}$. Xu [22] generally classified the dopants into different types: soft dopant, hard dopant and other dopants, e.g. complex dopant (two or more elements) in terms of the effects of dopants on material properties. The soft dopants tend to enhance the ferroelectric properties in PZT such as higher dielectric constant, higher bulk resistivity, and lower coercive field while the hard dopants usually lower dielectric constant, lower bulk resistivity, and increase coercive field. Due to the charge changes in the lattice caused by the introduction of the dopants, the dopants are usually considered as donors (soft) or acceptors (hard). The complex dopants are frequently used for better results, as they can introduce the beneficial properties of their constituents.

Table 2.1 lists the substituents and dopants commonly used in PZT materials [35]. Their ionic radii are also listed in Table 2.1 because they affect the stability and lattice distortion of perovskite structure. Additionally, these

Table 2.1 Radii (Å) of substitutions and dopants in PZT materials [35].

Substitution		Soft dopant				Hard dopant					
A	B	A	B	A	B	A	B				
Mg ²⁺	0.78	Sn ⁴⁺	0.74	La ³⁺	1.22	Nb ⁵⁺	0.69	K ⁺	1.33	Fe ³⁺	0.67
Ca ²⁺	1.06	Hf ⁴⁺	0.78	Nd ³⁺	1.15	Ta ⁵⁺	0.68	Na ⁺	0.94	Al ³⁺	0.57
Sr ²⁺	1.27			Sb ³⁺	0.90	Sb ⁵⁺	0.63			Sc ³⁺	0.83
Ba ²⁺	1.43			Bi ³⁺	1.14	W ⁶⁺	0.65			In ³⁺	0.92
				Y ³⁺	0.92					Y ³⁺	0.77
				Th ⁴⁺	1.10					Cr ³⁺	0.64
Pb ²⁺	1.32	Zr ⁴⁺	0.79								
		Ti ⁴⁺	0.68								

substitutions or dopants also have significant influence on the PZT phase diagram, e.g. shifting the phase boundary and introducing additional antiferroelectric or paraelectric phases. Therefore, it is desirable to control the concentration of substitutions or dopants within their solubility limit. For example, Tandon et al. [24] have shown the effects of Nd^{3+} ions on the dielectric and electromechanical properties of PZT ceramics whose compositions are near MPB ($\text{Zr}/\text{Ti} = 53/47$). The resistivity of PZT ceramics was observed to increase with increasing addition of Nd_2O_3 content up to 4 mole%, above which it starts decreasing slowly due to the formation of the second phase.

Among these methods of the compositional modifications, soft dopants and complex dopants are more desirable for improving the ferroelectric properties e.g. higher dielectric constant, higher resistivity and lower coercive field. Further, dielectric aging rates in donor doped PZT ceramics are found to be much lower than that in undoped ceramics. La^{3+} ions are well known and unique among the soft dopants for improving both properties and microstructure of PZT materials e.g. increased squareness of the hysteresis loop, lower coercive field, higher dielectric constant, promoting uniform grain growth, and homogeneous densification of a single phase, pore-free microstructure. The La-doped PZT materials (i.e. PLZT) have been extensively studied by Haertling et al. [47] and have found to exhibit characteristic properties depending upon the compositions. The room temperature phase diagram of the PLZT system is shown in Figure 2.5 [47]. By adjusting the compositions the PLZT materials have significant applications including ferroelectrics, piezoelectrics and electro-optics due to the distinct difference in the hysteresis loops of the various phases within their regions of stability (Figure 2.5).

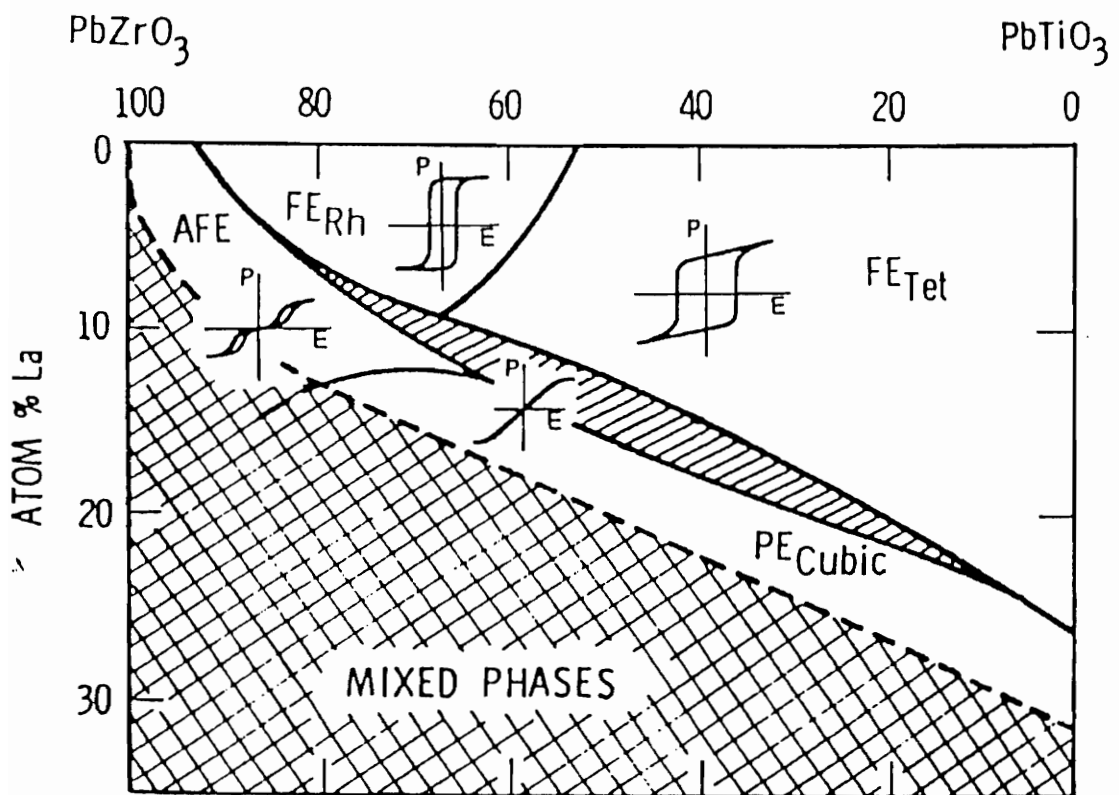
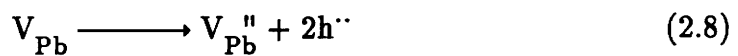


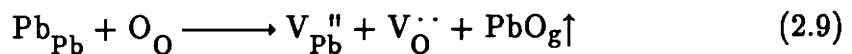
Figure 2.5 Room temperature phase diagram of the PLZT system [47].

There are several important features of the PLZT phase diagram. They are: (1) small variations in La content produces rather large changes in the areas of phase stability, (2) increasing La content suppresses the stability of the ferroelectric phases (rhombohedral and tetragonal) in favor of the nonferroelectric (cubic) and antiferroelectric phases, and (3) La additives reduce Curie temperature linearly. Other dopants such as Nd^{3+} ions are found to increase both the dielectric constant and the dielectric loss, inhibit the grain growth due to impedance of the grain boundary mobility, and enhance the sintering process in PZT ceramics [24].

It has been confirmed that undoped PZT ceramics exhibit p-type conduction and have a resistivity on the order of 10^{10} ohm-cm [21]. The p-type conduction in these materials is caused by the creation of lead vacancies due to lead oxide evaporation from the PZT materials during the sintering. Owing to this intrinsic excess of lead vacancies compared to the oxygen vacancies, holes are in turn formed in the vicinity of these lead vacancies as shown in the following defect equation:

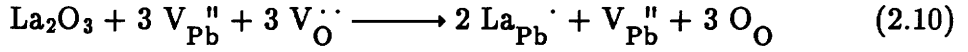


For the undoped PZT materials, the creation of vacancies are caused by lead oxide volatility during the sintering as following:



The compensation of these intrinsic vacancies can be achieved by the donor dopants. In case of La and Nb-doped PZT ceramics, where Pb^{2+} ions are partially replaced

by La^{3+} ions or Ti^{4+} (or Zr^{4+}) partially replaced by Nb^{5+} , the extra charges in the lattice caused by the dopants are compensated by the creation of lead vacancies to maintain electroneutrality as following:



Therefore, by introducing the donor dopants in PZT materials the vacancy concentration can be reduced. It has been noticed that oxygen vacancy plays an key role in the degradation phenomena of PZT films including fatigue, aging and low voltage breakdown. For this reason, the addition of these donor dopants has been found to reduce the dielectric degradation such as lower dielectric aging rates, improve fatigue properties and reduce leakage currents.

However, the defect mechanisms of PZT bulk ceramics are found to be very different from that of thin films [48]. One of the important factors is the processing temperature. Generally, in PZT bulk ceramics high sintering temperature (800°C or above) [49] is required to form the ferroelectric perovskite phase while PZT ferroelectric thin films, prepared by chemical solution deposition, can be completely formed at about 600°C [50]. PbO volatility in PZT thin films is thus negligible or nonexistent compared to bulk ceramics. Therefore, fewer lead vacancies in the intrinsic PZT films may subsequently lower hole concentrations and increase the resistivity. In addition, since lead vacancies are thought to facilitate the domain motions, the E_c of the PZT films, required for the domain motions, is expected to be

higher than that of bulk ceramics.

2.4 Chemical Solution Deposition: MOD and Sol–Gel Process

Chemical solution deposition methods including MOD and sol–gel process have received a lot of attention for the production of powders, spheres, thin films, coatings, and fibers for a variety of applications. In recent years this technique has been extended to the fabrication of thin films or coatings on different substrates. The applications of thin films include ferroelectric thin films, high–temperature superconductors, conductive coatings, optical coatings, and protective coatings [14,15,19].

2.4.1 Advantages

The chemical solution methods exhibits many advantages over other conventional ceramic or film processing. They are:

- (1) high chemical homogeneity can be maintained on an atomic scale in a multicomponent system.
- (2) excellent stoichiometry control as long as the different metalorganic compounds can be dissolved in a suitable, common organic solvent.
- (3) the compound formation temperatures and times can be significantly lowered compared to bulk ceramics due to the fact that the starting materials are mixed at the molecular level in the solution.
- (4) the film can be made under ambient conditions, therefore the processing cost can be reduced compared to most of vacuum deposition techniques.

(5) dopants, which are important for adjusting the microstructure or for improving the properties of the films, can be easily introduced into the solution in the form of soluble metalorganic compounds.

(6) a variety of techniques such as dipping, spinning, spraying, painting can be applied to deposit thin films on the substrate, which allows the process to be tailored for specific requirements.

Although the chemical solution deposition provides a fast and easy route for preparing ceramic thin films, it has not been commercialized for electronic films. The reason is, some disadvantages have been noticed in the chemical solution deposition such as film cracking due to large shrinkage occurring in film formation, limited availability of some precursor materials, and some high cost precursor materials. Further improvements and modifications of the process have been extensively investigating to conquer these problems.

2.4.2 Selection of Precursors

There are a lot of processing variables involved in the selection of precursors for the chemical solution deposition: nature of precursor and solvent, concentration, temperature, pH value, composition, and viscosity. These parameters influence the structure of the resulting solution or gel, which in turn affects the characteristics of the films due to the reactions occurring during solution preparation. To control the thickness and volatility of the films during firing parameters like viscosity, surface tension, concentration, and boiling point of the solution can be adjusted by a careful selection of the materials [51–53].

Some general rules can be used as a guide to choose the precursor used for the MOD and sol-gel processing. The ideal precursors used for chemical solution deposition should possess the following characteristics [54]: (1) high metal content, (2) high solubility in common organic solvents, (3) stability under ambient conditions, (4) capability of thermal decomposition without evaporating or melting, (5) no contamination from the organics of the precursors, (6) compatibility between each precursor in the case of multicomponent materials, and (7) nontoxicity. However, not all of the required properties can be simultaneously achieved; for example, the solubility usually increases with the chain length of organic ligand whereas the metal content decreases with that. Therefore, in the selection of MOD and sol-gel precursors these requirements have to be compromised. Haertling [4] summarized several precursor systems developed for the chemical solution deposition of PZT and PZT-related thin films (Table 2.2) [4,13,51,53].

Basically, there are three different classes of precursors used in MOD and sol-gel: (1) metal alkoxides, $M(OR)_x$; (2) metal carboxylates, $M(OOCR)_x$; and (3) metal acetylacetonates, $M(C_5H_7O_2)_x$; where M is metal, R is an alkyl group, and x is the valence of the metal. Metal alkoxides were commonly used in sol-gel and MOCVD. The degree of moisture sensitivity of the titanium and zirconium alkoxides is a function of the metal atom size. The smaller Ti^{4+} ion (0.68 Å) is somewhat shielded from atmospheric moisture by its organic ligands, whereas the larger Zr^{4+} ion (0.79 Å) is not completely shielded by its ligands, and react with atmospheric moisture [55].

MOD process usually uses carboxylates, which are formed by the bonding of

Table 2.2 Chemical solution deposition method for PZT and PZT-related thin films [4].

Process	Composition [*]	Precursor	Solvent
MOD	PZT	Pb 2-ethylhexanoate Zr acetylacetonate Ti tetrabutoxide	butyl alcohol
Sol-gel	PLZT PZT PT	Pb acetate La acetate Zr isopropoxide Ti isopropoxide	2-methoxyethanol
MOD	PLZT PZT PT	Pb neodecanoate La acetate Zr n-propoxide Ti dimehtoxy dineodecanoate	xylene
MOD	PT	Pb oxyacetate Ti n-butoxide	acetylacetone
MOD	PLZT	Pb subacetate La acetate Zr acetate Ti acetylacetonate	methanol

* Composition Designations:

PLZT: $(\text{Pb}_{1-x}\text{La}_x)(\text{Zr}_y\text{Ti}_{1-y})\text{O}_3$

PZT: $\text{Pb}(\text{Zr}_x\text{Ti}_{1-x})\text{O}_3$

PT: PbTiO_3

a metal ion to a carboxylic acid. A typical carboxylate structure is $M-O-C(=O)-R$, where M is a metal atom bonded to oxygen and R is a hydrocarbon chain. The solubility, viscosity, and volatility of the carboxylate precursor is strongly dependent on the species of metal atom and the length, number and structure of the hydrocarbon chain (R) attached to the metal ions [14]. It was found that cracking problems might occur due to the high organic content of the films. Haertling [4] has developed an MOD method, using acetate-based and water-soluble precursors with small organic ligands, which minimizes the tendency toward cracking. Since the precursors are typically water insensitive, MOD is more straightforward as compared to sol-gel.

Recent investigations [52,56,57] have used fourier transform infrared spectroscopy (FTIR), Raman spectroscopy, and nuclear magnetic resonance (NMR) techniques to identify the structures of precursors and hydrolysis/condensation products in situ; whereas mass spectromeric experiments, e.g. electron impact and chemical ionization, were employed for molecular formula determination. The studies regarding solution aging and mixing order effects on thin film microstructure and ferroelectric properties have been developed at Sandia National Laboratories [52]. It has been found that the solution chemistry dramatically affect the microstructures and properties of resulting films.

2.4.3 Film Formation

The chemical solution deposition process consists of following steps: (1)

preparation of the precursor solution, (2) hydrolysis, (3) deposition onto a substrate, (4) removal of solvent and pyrolysis, and (5) crystallization of the film. For MOD process, there is no hydrolysis step prior to pyrolysis. There are some differences between the MOD and sol-gel process [32,55]. The MOD process only involves pyrolysis and annealing of the films whereas the sol-gel consists of hydrolysis, dehydrolysis, and final polymerization to a gel or a film. Usually, the metalorganic compounds used for MOD have oxygen as a bridge between a metal and an organic ligand. Therefore, for MOD, the M-O-M bonds are formed during thermal decomposition of metalorganic compounds on the substrates for MOD while the sol-gel produces the M-O-M bonds in the gel. In sol-gel, the gelation of the solution is formed by hydrolysis and condensation of alkoxide precursors. Further polymerization occurs via dehydrolysis after the hydrolysis step, and a network of M-O-M is thus formed. In MOD process, following deposition of the film on the substrate from the precursor solution, the removal of solvent and pyrolysis occurs.

The as-deposited, wet film is converted into a dry and stiff film after significant shrinkage during pyrolysis, where the variations in physical morphology such as thickness, cracking, surface roughness, residual stress, and inhomogeneous nucleation become important. Yi et al. [19] presented a simple model for the drying of the gel in the sol-gel process. The model states that: (1) a gel is basically composed of a solid phase of continuous network and a continuous liquid phase, (2) the gel shrinks under capillary force as the liquid evaporates, (3) cracking might occur in the region with a stress concentration under surface tension and later the cracking propagates along the film. To solve the cracking problems, many methods have been proposed which include the use of surfactants, drying control chemical

additives (DCCA), cross-linking agents, and hypercritical drying. Additionally, based on thermogravimetric studies, it is believed that gradual change in weight loss can prevent cracking [15,19]. After the removal of residual organics by decomposition or polycondensation reactions, the wet film is converted into a dry film composed of complex oxides (amorphous phase). Further crystallization of the film is achieved by the sintering mechanism in which the pores in the film collapse and the dense film is thus obtained [19].

2.4.4 Structure Development

Peng et al. [59] have developed a nondestructive optical method for the structure development in MOD PZT films. Based on a simple model (Figure 2.6) proposed by Peng, the structure changes of MOD PZT films upon annealing are illustrated in the order of metalorganic compounds (MO), amorphous phase (A), pyrochlore phase (Py), and perovskite phase (Per). Each structure has both initiation and completion formation temperatures. The designations of the transformation temperature (T) from one structure to the other are: the subscript i and c represent the initiation and completion formation, respectively, whereas the superscript represents the phase of interest. For instance, T_i^{Per} and T_c^{Per} respectively represent the temperatures at which the perovskite formation is initiated and completed. Additionally, the structure presented in the temperature intervals T_i^{A} to T_c^{A} , T_i^{Py} to T_c^{Py} , and T_i^{Per} to T_c^{Per} are assumed as the regions of two phase mixtures MO/A, A/Py, and Py/Per, respectively. Utilizing this method the initiation and completion temperatures of pyrochlore and perovskite phases in PZT films can be identified by plotting refractive index as a function of the annealing

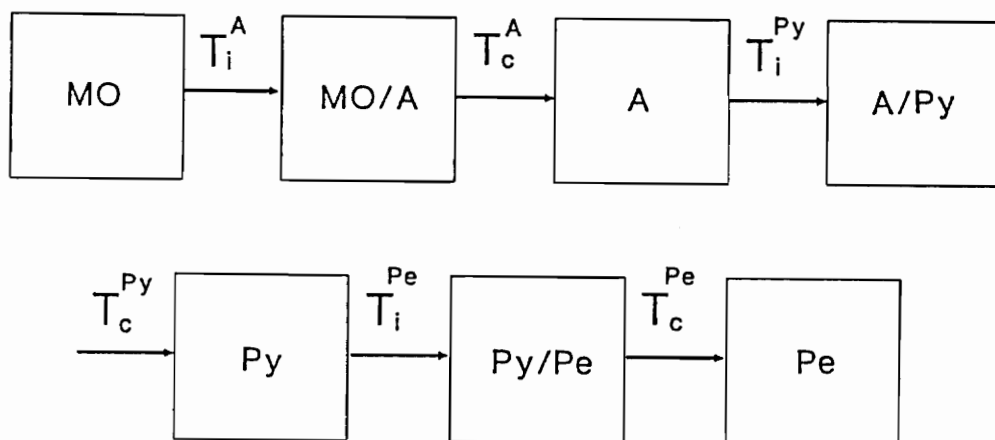


Figure 2.6 A simple model of the structure development in MOD PZT films [59].

temperature.

2.4.4.1 Pyrochlore to Perovskite Phase Transformation

Most of the PZT bulk ceramics are fabricated by solid state reaction using PbO, ZrO₂ and TiO₂ powders, which usually required high sintering temperature to form the ferroelectric perovskite phase. Prior to the formation of the perovskite, an intermediate phase, PbTiO₃, is formed. In contrast to the solid state reaction, an intermediate pyrochlore phase is also found for sputtered films at annealing temperature between 450°C and 575°C [38], as well for sol-gel derived films during annealing at 350°C to 600°C [60]. X-ray diffraction analysis shows that with increasing annealing temperature the structure of the MOD PZT films changes from amorphous to pyrochlore and finally perovskite phase. As seen in the x-ray diffraction pattern, the pyrochlore phase (A₂B₂O_{7-x}, where x ≈ 1 for PZT) is found to be a highly defective (oxygen deficient) and nanocrystalline structure with a relatively broad peak. The transformation temperature from pyrochlore to perovskite phase in PZT films is a function of both precursor types and the preparation methods used. Additionally, the crystallization process of the films is dependent on the substrate, e.g. silicon, sapphire, quartz, MgO, and MgAl₂O₄, and/or barrier used [61,62].

Chapter 3. EXPERIMENTAL PROCEDURE

Undoped, La and Nd-doped PZT (i.e. PLZT and PNZT) and Nb-doped PZT ferroelectric thin films were prepared by chemical solution deposition methods. Most of the films were fabricated using metalorganic decomposition (MOD) which is a modification of the process developed by Budd et al. [12]. Figure 3.1 shows a flow diagram for the preparation of MOD undoped and doped PZT films. The detailed procedures in the flow chart will be discussed in the subsequent sections. Unlike sol-gel process, no hydrolysis step was included in our technique, hence the name MOD.

3.1 Preparation of Precursor Solution

A flow chart for the preparation of undoped, PLZT and PNZT precursor solutions by the MOD process is shown in Figure 3.2. High-purity lead acetate trihydrate, lanthanum acetylacetonate, neodymium acetate, niobium ethoxide, zirconium n-propoxide, and titanium iso-propoxide (AESAR/Johnson Matthey) were used as the starting materials, with 2-methoxyethanol (Fisher) as the solvent. Table 3.1 lists selective properties of the starting materials. A 10% excess lead oxide was included in all precursors to control the stoichiometry during heat treatment of the films. The Zr/Ti ratio for all systems was kept constant at 50/50, which is close to the morphotropic boundary (MPB). The dopant concentration was kept below 6 at.% such that the films remained in the ferroelectric region.

MOD processing

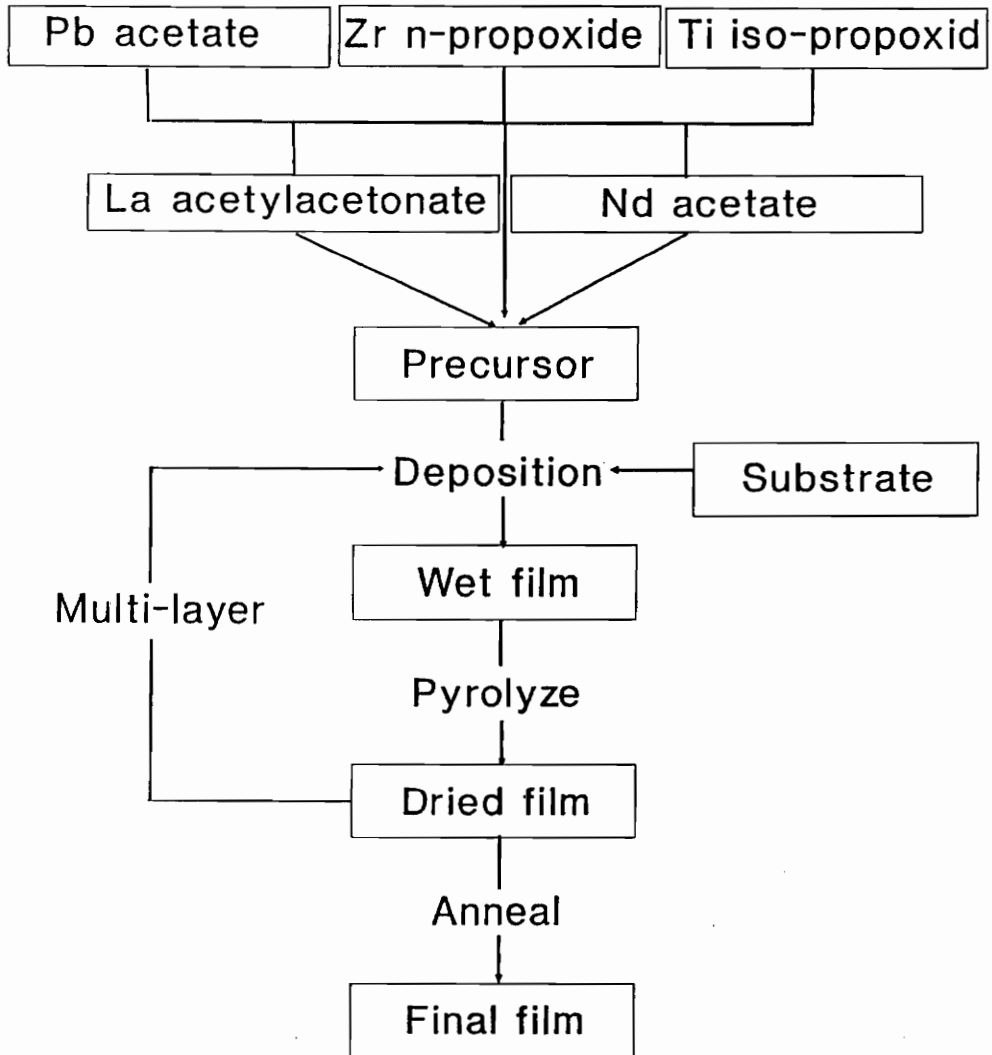


Figure 3.1 A flow chart for the preparation of undoped and doped PZT films by MOD process.

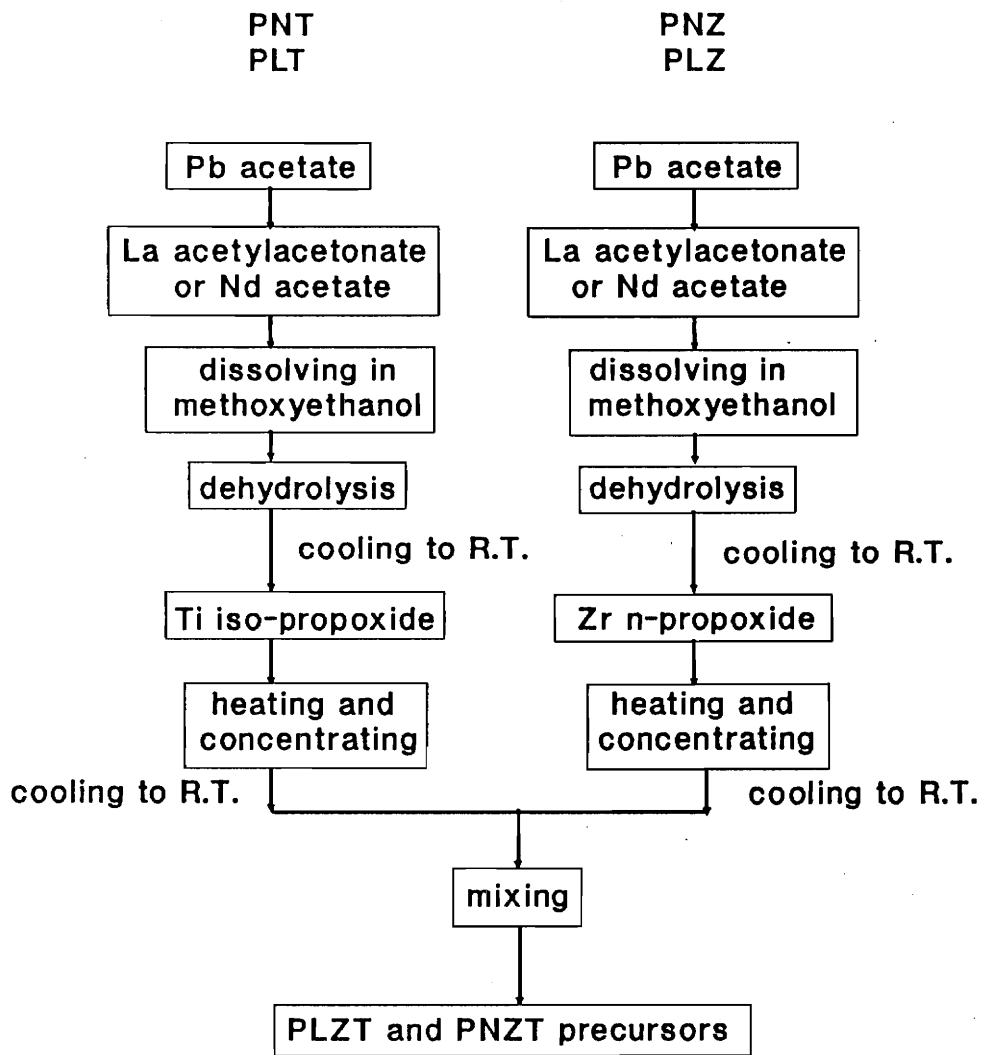


Figure 3.2 A flow chart for the preparation of undoped, PLZT and PNZT precursor solutions by the MOD process.

Table 3.1 Selective properties of the starting materials.

Chemicals	Metal content(wt.%)	m.p./b.p.(°C)
Lead acetate trihydrate $\text{Pb}(\text{C}_2\text{H}_3\text{O}_2)_2 \cdot 3\text{H}_2\text{O}$	64	75/280
Lanthanum acetylacetonate $\text{La}(\text{C}_5\text{H}_7\text{O}_2)_3 \cdot 1.5\text{H}_2\text{O}$	32	—
Neodymium acetate $\text{Nd}(\text{C}_2\text{H}_3\text{O}_2)_2 \cdot x\text{H}_2\text{O}$	45	—
Niobium ethoxide $\text{Nb}(\text{OC}_2\text{H}_5)_5$	29	6/—
Zirconium n-propoxide $\text{Zr}(\text{OC}_3\text{H}_7)_4$ in 30% propanol	28	—
Titanium iso-propoxide $\text{Ti}(\text{OC}_3\text{H}_7)_4$	17	20/58
2-methoxyethanol	—	—/125

One molar solutions of La and Nd-doped lead titanate (PLT and PNT) and lead zirconate (PLZ and PNZ) were separately prepared. Equal amounts of PLT and PLZ and PNT and PNZ solutions were then mixed and diluted with 2-methoxyethanol to form 1 molar PLZT and PNZT precursor solutions, respectively. The solution were filtered by using 0.5 μm syringes and were then diluted to various concentrations for fabricating thin films.

Part of the samples were made by a sol-gel process, which has been developed at our laboratory and discussed in detail in the Ph.D dissertation of Kwok [20]. The undoped and doped PZT precursor solutions were made as described in his dissertation. The compositions of precursors in sol-gel process were controlled similar to those in MOD.

3.2 Characterization of Precursor Solution

Some of the processing variables for the film fabrication such as the drying and crystallization temperatures were selected on the basis of the information obtained from the solution characterization. The vaporization and decomposition temperatures of the PZT (50/50) solution were determined by thermogravimetric analysis (TGA), executed on a DuPont 2100 thermogravimetric system. Temperatures were ranged from 30°C to 750°C, at 10°C/min increments. Solution sample size was kept constant at 2 mg. The TGA experiments were executed under an ambient condition (air) and nitrogen atmosphere. Dry nitrogen was chosen as the purge gas to eliminate reactions of the precursor with oxygen or water, which interfere with vaporization or decomposition of the sample.

The crystallization temperatures for the different phases of the PZT (50/50) were determined using a differential scanning calorimeter (DSC) for the pretreated precursor solution and an x-ray diffractometer (XRD) with $\text{CuK}\alpha$ radiation for the residual powder of the solution. The DSC experiments were executed on a Delta Series DSC7 system under an ambient condition. Temperatures were ranged from 30°C to 700°C in a heating rate of $10^\circ\text{C}/\text{min}$. The DSC sample was prepared by drying the solution at 120°C for 8 hours and 250°C for 8 hours for the removal of the solvent and organic. To identify the phase changes occurring in the solution, the pretreated solution (after $120^\circ\text{C}/8\text{h}$ and $250^\circ\text{C}/8\text{h}$ drying) was annealed at the temperatures corresponding to the first two exotherms in the DSC curves, i.e. 411°C and 468°C , for 8 hours. The residual solutions were then ground into powders and were subjected to XRD characterization.

3.3 Preparation of Thin Film

Three different substrates were chosen in this study: single-crystal sapphire, RuO_x and $\text{Pt}/\text{Ti}/\text{SiO}_2/\text{Si}$. The undoped and doped films were prepared by spin-coating the solution onto these substrates at different rpm for 30 seconds under ambient conditions. To evaporate the solvent, the spin-coated specimens were subjected to a low temperature heat treatment at 150°C for 5 minutes on a hot plate. In order to obtain thicker films, the process of coating and drying was repeated 2 to 5 times. The required film thickness was achieved by adjusting either the concentration of the precursor solution (Figure 3.3), the spin speed (Figure 3.4) [63], or the number of the coat-bake cycle. Usually, the solution concentration of 0.5 M, spin speed of 2000 rpm and 3 coat-bake cycles were chosen for comparison.

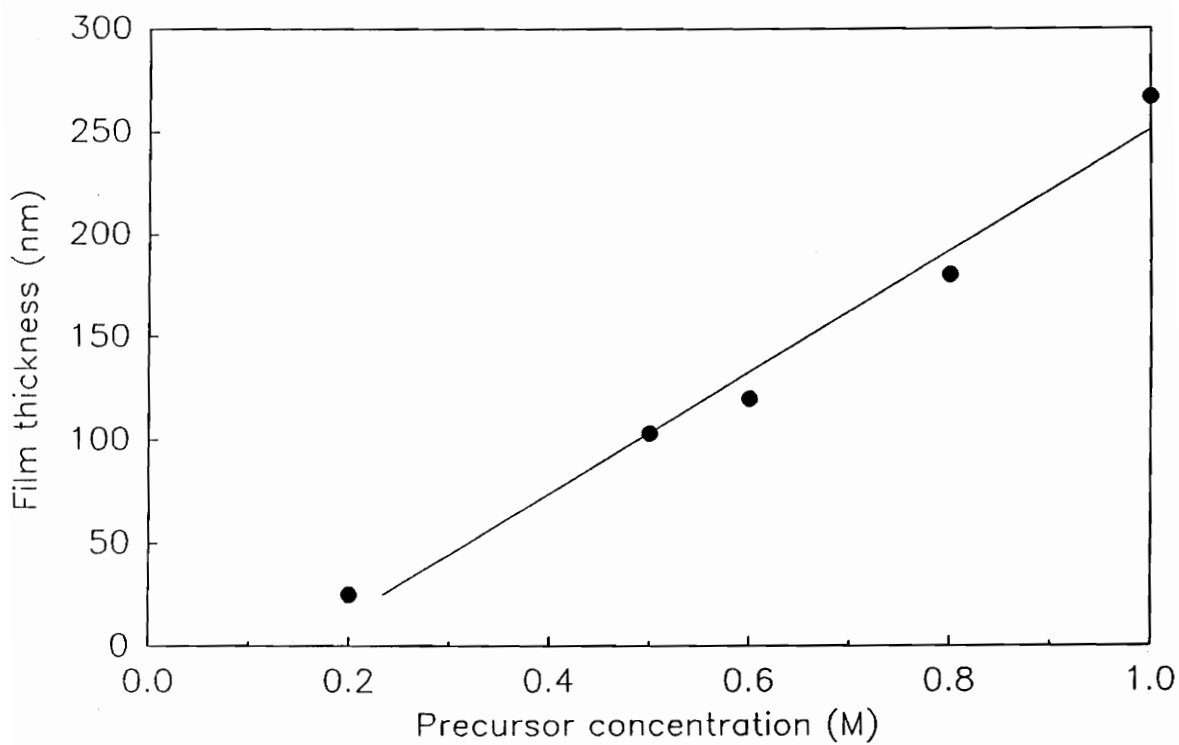


Figure 3.3 Film thickness as a function of molar concentration of the solution.

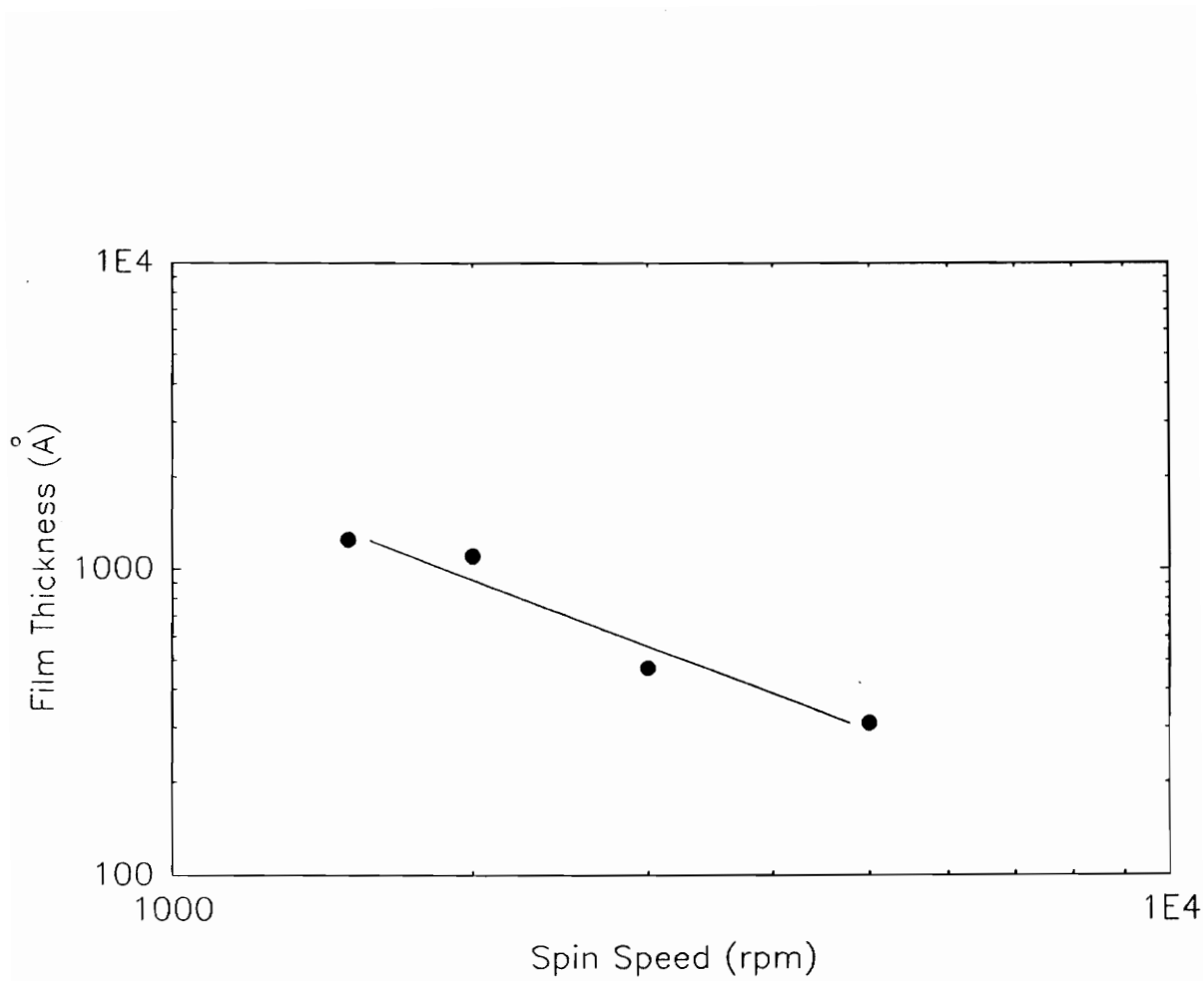


Figure 3.4 Film thickness as a function of spin speed.

Later the specimen were subjected to a high temperature heat treatment ranged from 300°C to 750°C for 30 to 60 minutes in a box or a quartz tube furnace under ambient conditions.

3.3.1 Preparation of TEM specimen

Both undoped and doped PZT thin foils used for TEM observation were prepared by spin-coating method. The 0.5 M solution was spin-coated on platinized-nickel TEM grids with 400 mesh at 2000 rpm for 30 seconds. The as-coated foil was supported by surface tension and dried in air and then annealed at the temperatures ranged from 500°C to 650°C for 15 minutes in a quartz tube furnace under ambient conditions.

3.4 Thin Film Characterization

3.4.1 General

The bulk compositions of the films were characterized by using electron probe microanalysis (EPMA). Quantitative analysis of Pb, Nd, La, Zr, and Ti ions was performed using a 8 kV, 50 mA source. Ten measurements were made at different areas of each sample and averaged to obtain the final data points. The compositional heterogeneity analysis was carried out by using energy dispersive x-ray (EDX) spectroscopy.

The Curie temperature was determined by in-situ hot-stage experiments

using a Phillips 420 transmission electron microscope (TEM) operating at 120 kV ($\lambda = 0.3348 \text{ \AA}$). Lattice parameter determination and phase identification were made by x-ray and electron diffractions. For the tetragonal phase, the crystal tetragonality (c/a ratio) of the films were thus determined by measuring the d spacing and calculating based on following equation:

$$\frac{1}{d_{hkl}} = \frac{h^2 + k^2}{a^2} + \frac{l^2}{c^2} \quad (3.1)$$

where h , k , and l are elements of Miller index. Microstructure of the films was characterized by using optical microscopy, scanning electron microscopy (SEM), and scanning transmission electron microscopy (STEM).

3.4.2 Optical Property Measurement

Optical properties of undoped and doped PZT films were investigated using UV–VIS–NIR scanning spectrophotometer (Shimadzu UV–3101PC). For optical property measurement, the samples were made by spin-coating the solution on transparent sapphire substrates under the same processing conditions. Later the specimens were subjected to a heat treatment at 650°C for 30 minutes in a tube furnace. Specular transmission spectra were taken in a range of 200 nm and 2000 nm for each sample. The refractive index and thickness of the film were calculated from the measured transmission using the envelope method. In addition, the packing density of the films were determined using the effective medium approximation. The detailed calculations of refractive index, thickness and packing density of the film are listed in Appendix A [59].

3.4.3 Electrical Property Measurement

For electrical property measurements, both Pt and RuO_x bottom electrodes were used. Palladium top electrodes, 0.00021 cm² area and 400 nm thickness dots, were deposited on the post-annealed films by electron beam evaporation under 10⁻⁷ Torr. The ferroelectric properties and hysteresis loops of the films were measured using a standardized RT66A tester operating in a Virtual-Ground circuit with a 0.0047 μF internal capacitor at 60 Hz. For fatigue measurements, an alternating square wave pulse was used with a pulse of 8.6 μsec, pulse period of 21 μsec and an applied voltage of 5 volts. The alternating square wave pulse is described in Figure 3.5.

3.5 Preparation and Characterization of Bulk Ceramics

For dielectric property measurements, the powder was synthesized by evaporating the solvent from the solution at 120°C for 1 hour, grinding the residue and calcining the residue in a covered alumina crucible at 650°C for 8 hours to obtain perovskite phase. Synthesized powders were mixed with binders (3 wt% methocel) and then were uniaxially pressed as pellets. The binder of pellets was burned out at 300°C. The pellets were covered with lead zirconate powders (10% excess PbO) and sintered in alumina crucibles at 950°C for 4 hours.

The resulting pellets were polished on both sides. Epoxy resins and hardeners (Epo-Tek p-10, Epoxy Technology Inc.) were used to contact copper wire electrodes on both sides and cured at 150°C for 1 hour. The dielectric

Alternating:

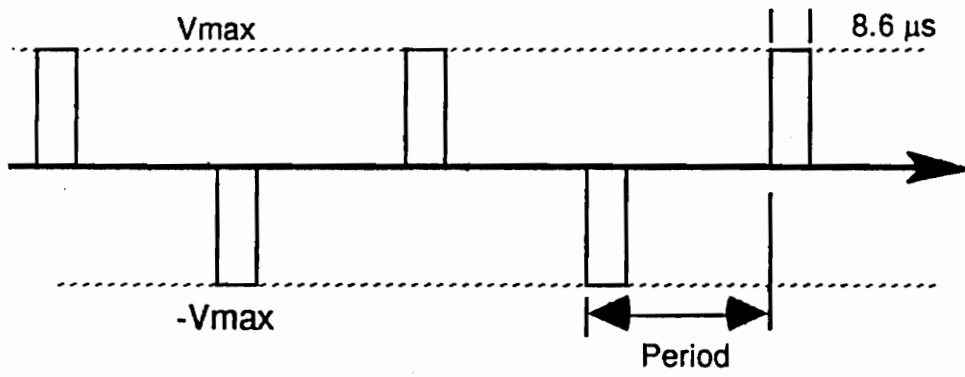


Figure 3.5 An alternating square wave pulse used for fatigue measurements.

properties such as dielectric constant and dielectric loss versus temperature were measured at frequencies of 1, 10, and 100 kHz using an LF impedance analyzer (Model HP 4192A, Hewlett-Packard Co.) with a furnace (Thermodyne type 1300) and a temperature controller (Omega CN 900). Prior to X-ray diffraction characterization, the powders were heated in a boiling acetic acid (5 wt%) solution to remove any excess lead oxide.

Chapter 4. RESULTS AND DISCUSSION

4.1 Precursor Characterization

The processing temperatures of the films were selected using the information obtained from thermogravimetric analysis (TGA) and differential scanning calorimetry (DSC) of the precursor solutions.

Figures 4.1(a) and (b) show the results of TGA for PZT (50/50) precursor solution heated in air and nitrogen, respectively. The heating rate used in this TGA experiment was 10⁰C/min. Three different weight loss regions are observed when the precursor solution is heated in both air and nitrogen. The initial rapid weight loss between 25 and 100⁰C in air and between 25 and 60⁰C in nitrogen corresponds to the removal of most of the solvent (2-methoxyethanol) and/or moisture from the solution. The maximum rate of weight loss as seen in Figure 4.1(a) occurs at 73⁰C in air. The second region between 100⁰C and 200⁰C (60⁰C and 100⁰C in nitrogen) shows a slower rate of weight change and is a result of the removal of the remaining solvent and/or moisture. In the third region following the removal of the solvent, the metalorganic solution combines with the moisture in air and decomposes slowly between 200 to 400⁰C. In comparison (Figure 4.1(b)), when the solution is heated in nitrogen (in the absence of moisture) the solution actually decomposes in a narrower range of temperature between 200 and 273⁰C. The completion reaction of decomposition occurs around 273⁰C, indicating the complete removal of organics from metalorganic compounds. After 600⁰C, for both in air and nitrogen

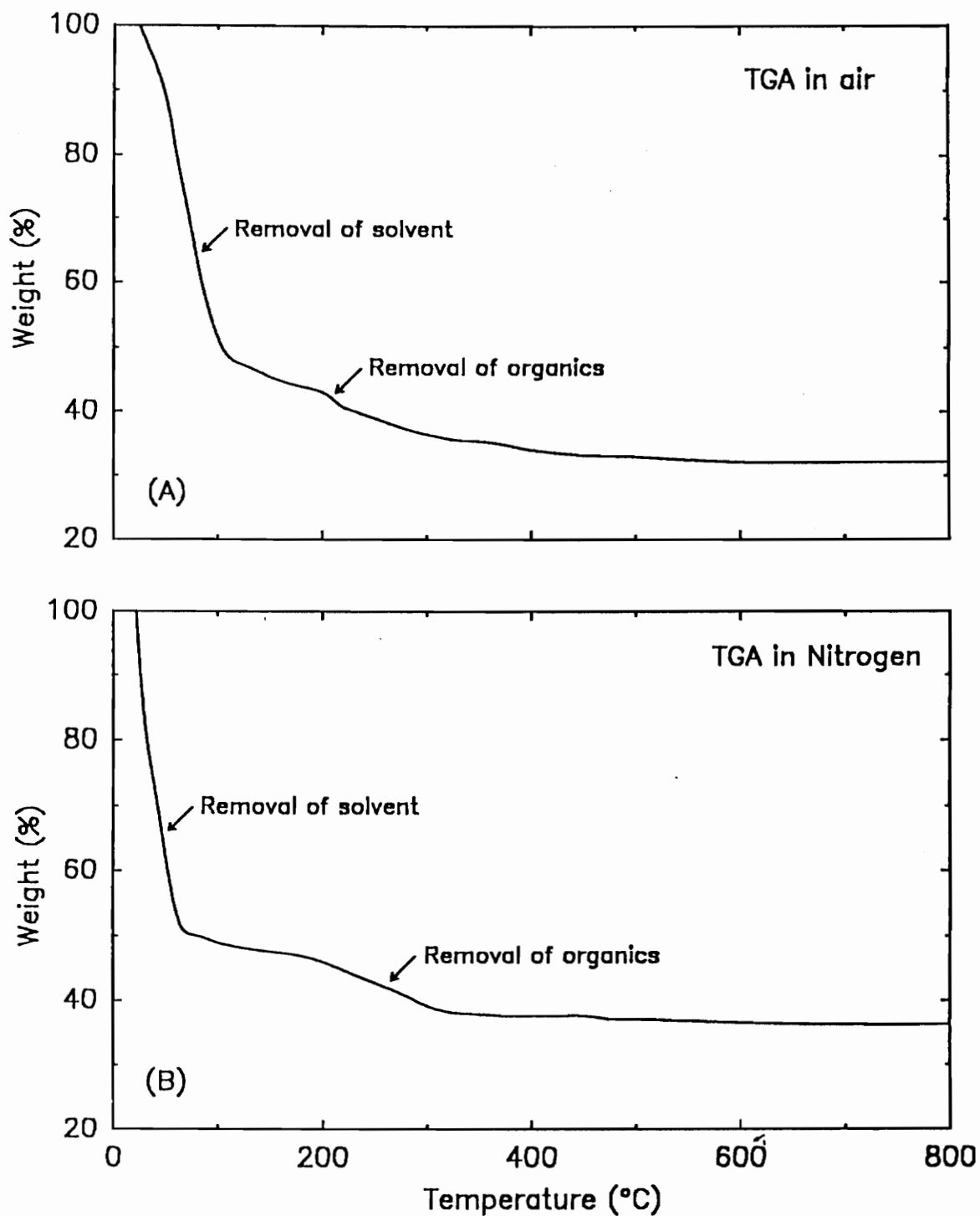


Figure 4.1 Thermogravimetric analysis of the PZT (50/50), 0.5 M, precursor solution heated at 10°C/min in (a) air and (b) nitrogen.

atmospheres, the weight of the residual precursor remains constant. This indicates that any other changes occurring in the film after 600°C are not accompanied by a resultant weight change. In fact, after the organics are removed, the precursor undergoes transformation from amorphous to pyrochlore to finally perovskite phase. This thermal decomposition behavior of the PZT precursor solution is in agreement with the observations made by Lipeles et al. [64]. As can be seen, it is difficult to define the evaporation and decomposition temperatures of the precursor because of the continuous change in slope of the TGA curves. The gradual weight loss upon heating implies that the solution is stable and water-insensitive when stored in ambient conditions and therefore alleviates the cracking problem of the film during drying. The results also show that the weight loss percentage is smaller in nitrogen than that in air. The difference in the rate of weight loss in air and nitrogen atmospheres also implies that oxidation plays a role in pyrolysis. Based on the results from TGA of the precursor solution, the drying temperature of the as-coated film was chosen at 150°C prior to annealing to ensure the complete removal of solvent and any residual moisture.

The crystallization temperatures for the different phases of the PZT (50/50) were determined using the information obtained from the DSC of the pretreated precursor solution and XRD of the residual powders. Figure 4.2 shows the results of DSC for the powder derived from the PZT (50/50) precursor heated in air. The DSC sample was prepared by drying the precursor at 120°C for 8 hour and then 250°C for 8 hour to ensure the removal of the solvent and organics. The solid line (DSC curve) in Figure 4.2 indicates the heat flow as a function of temperature while the dash line the first derivative of the DSC curve. As seen in the DSC curve, a

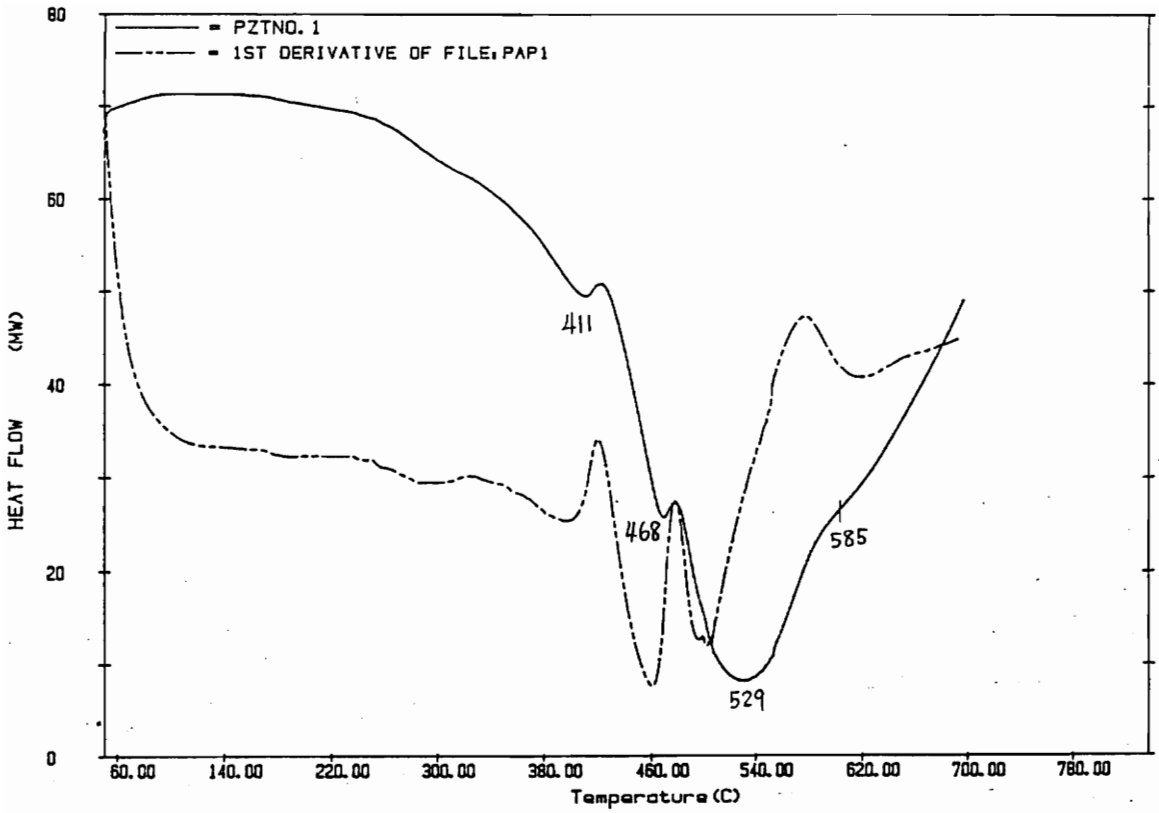


Figure 4.2 A differential scanning calorimetry curve of the PZT (50/50) precursor solution.

number of exotherms can be observed, corresponding to the phase changes occurring in precursor. To identify these phase changes the pretreated solution was heat treated at the temperatures corresponding to these exotherms for 8 hours. Figure 4.3 shows the XRD patterns for the precursor heated at 411°C and 468°C corresponding to the peaks of the first two exotherms in the DSC curve. For comparison, the XRD pattern of complete perovskite phase for the powder dried at 650°C is also included. From the XRD results the first exotherm of the DSC curve observed at 411°C corresponds to phase transformation from the amorphous phase to the pyrochlore phase. The second exotherm at 468°C marks the initiation of phase transformation from the pyrochlore to the perovskite phase. The other exotherms observed at higher temperatures correspond to the transformation to the perovskite phase. Based on this study, the initiation formation temperatures of pyrochlore and perovskite phases were determined as 411°C and 468°C, respectively.

The information obtained from these results can be used in conjunction with a structure development model of MOD PZT films proposed by Peng et al. [59] to systematically follow structure changes occurring in the precursor during annealing. As illustrated in Figure 4.4, the structure changes of the MOD derived PZT powders upon annealing are in the order of solution (SOL), metalorganic compounds (MO), amorphous phase (A), pyrochlore phase (Py), and perovskite phase (Per). The SOL is composed of various metalorganic compounds and solvent. The solvent is removed from SOL at T_i^{MO} (73°C as observed in the TGA curve), at which the formation of MO is initiated. Following the formation of MO, the decomposition reaction (the removal of organics) occurs at T_i^A (273°C obtained from the TGA curve), indicating the initiation formation of amorphous phase. Similarly, T_i^{Py}

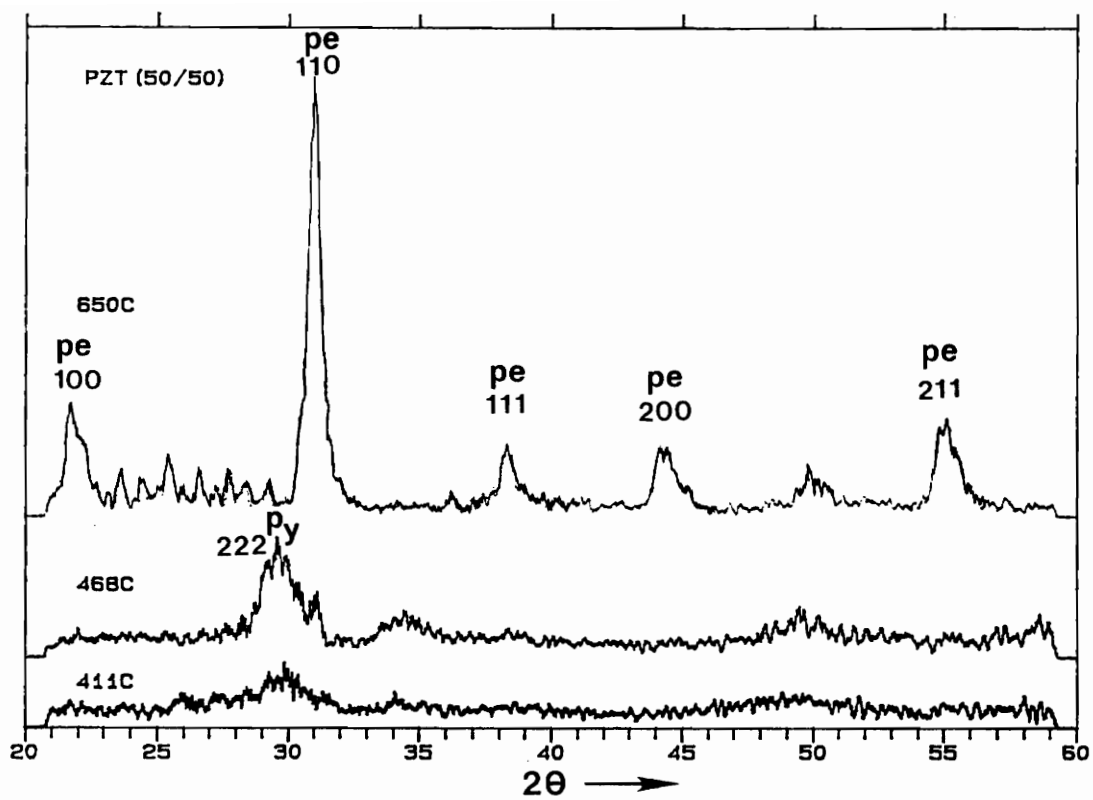


Figure 4.3 The x-ray diffraction patterns of the MOD PZT (50/50) powders heated at 411°C, 486°C and 650°C.

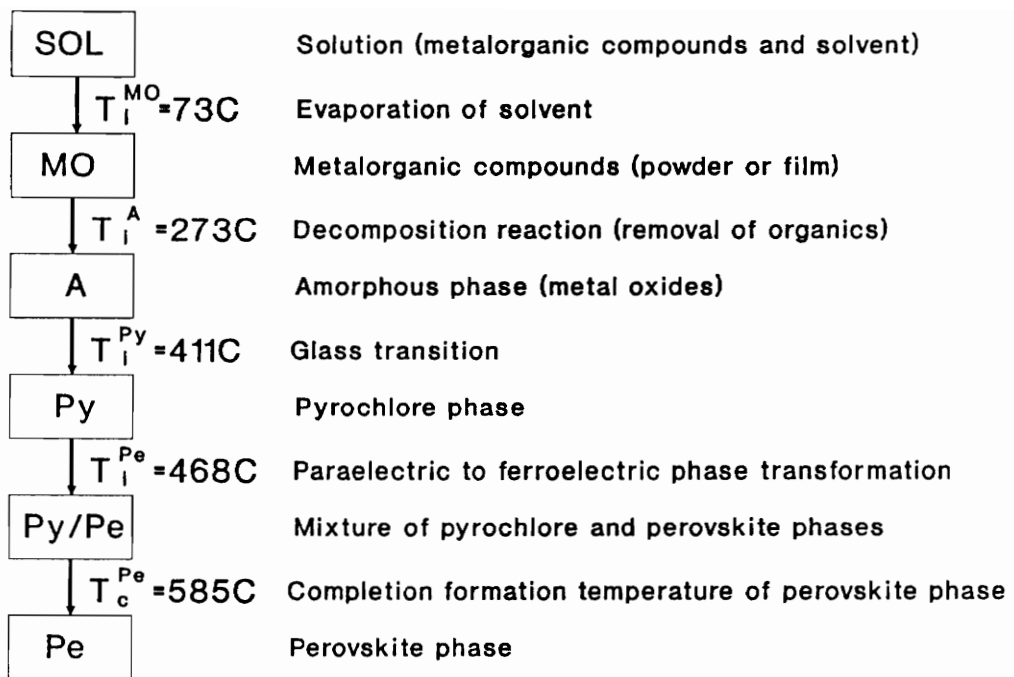


Figure 4.4 The structure change as a function of temperature for the PZT (50/50).

(411°C) indicates the initiation formation temperature of pyrochlore phase from amorphous while T_i^{Per} (468°C) the initiation formation temperature of perovskite from pyrochlore. Later the formation of perovskite is completed at T_c^{Per} (585°C). The initiation formation temperature of pyrochlore phase was also found to be 450°C for sputtered PZT films and 350°C for sol–gel films, whereas completion temperature of pyrochlore was 575°C for sputtered films and 600°C for sol–gel films [38,60]. The difference between the behavior such as transformation temperature of PZT bulk ceramics and that of thin films has been observed in most of studies.

4.2 Composition

One of the advantages the MOD process offers over other methods is the ease of compositional control. The composition of the final film is dependent on the starting precursors and the thermal processing conditions. As the drying or annealing temperature is increased, the structure of the MOD film changes from amorphous to pyrochlore and finally perovskite phase. Therefore, in this study, the composition was investigated in each phase of the MOD film using EPMA, STEM and EDX.

The bulk compositions of the final films analyzed by EPMA are presented in Table 4.1 along with the compositions of the corresponding precursor solutions. All the films that were deposited on sapphire substrates were annealed at 650°C to complete the formation of perovskite phase. The film thickness as determined by UV–VIS–NIR transmittance spectrum analysis was found to be about 300 nm. The EPMA data indicates that the film thickness is sufficient to avoid any substrate

Table 4.1 The bulk compositions of PLZT and PNZT films on sapphire substrates analyzed by EPMA along with the compositions of corresponding precursor solutions.

Compositions	La or Nd	Zr	Ti
PZT(50/50)	—	53.3	46.7
PLZT(2/50/50)	1.909	50.2	49.8
PLZT(4/50/50)	4.028	49.5	50.5
PLZT(6/50/50)	6.048	48.2	51.8
PNZT(2/50/50)	1.922	53.2	46.8
PNZT(4/50/50)	3.803	54.0	46.0
PNZT(6/50/50)	5.595	50.7	49.3

effect on composition. A one-to-one correspondence can be seen from Table 4.1 between the film composition and the composition of the precursor from which the film is made. Especially, the concentrations of the trace elements (La and Nd) are in a good agreement with the expected values.

For comparison, in addition to the bulk composition of the final film, the composition of as-deposited film was also studied. The results of EPMA for the PZT (50/50) film made at different thermal processing conditions are listed in Table 4.2. As seen from the results, the composition of the as-made film with 3 coat-bake (150°C) cycle is similar to that of the post-annealed (650°C) film. The as-made film is believed to be a mixture of various metalorganic compounds, whereas the annealed sample consists of the perovskite phase. Although there is a 4 at.% lead loss and a slight change in Zr/Ti ratio, the results indicates that adding 10 at.% excess lead to the precursor is sufficient for maintaining the desirable film stoichiometry. In fact, it has been found that the PZT film with excess lead oxide ranged from 5 to 10 % exhibits the best ferroelectric properties [20,60].

Figures 4.5(a) and (b) show STEM micrographs of the PNZT (1/50/50) film on a Pt substrate, subjected to a final annealing at 700°C for 1 hour. Figure 4.1(a) is a combination image obtained from both backscattering electrons and secondary electrons, whereas (b) an image only from backscattering electrons. Both photographs were taken in the same area of the specimen. In Figure 4.5(a), the well-formed grains are known to be perovskite phase, while most of the surrounding region is pyrochlore. The identification of these phases was carried out using TEM and is discussed in detail in a later section. Figure 4.5(b) shows the similarity in

Table 4.2 The results of EPMA for the PZT (50/50) films on sapphire substrates at different heat treatment conditions.

Conditions	Pb	Zr	Ti
Precursor(expected)	20.00	10.00	10.00
As-made(150°C)	20.89	9.75	9.39
Annealed(650°C)	19.99	9.75	10.26

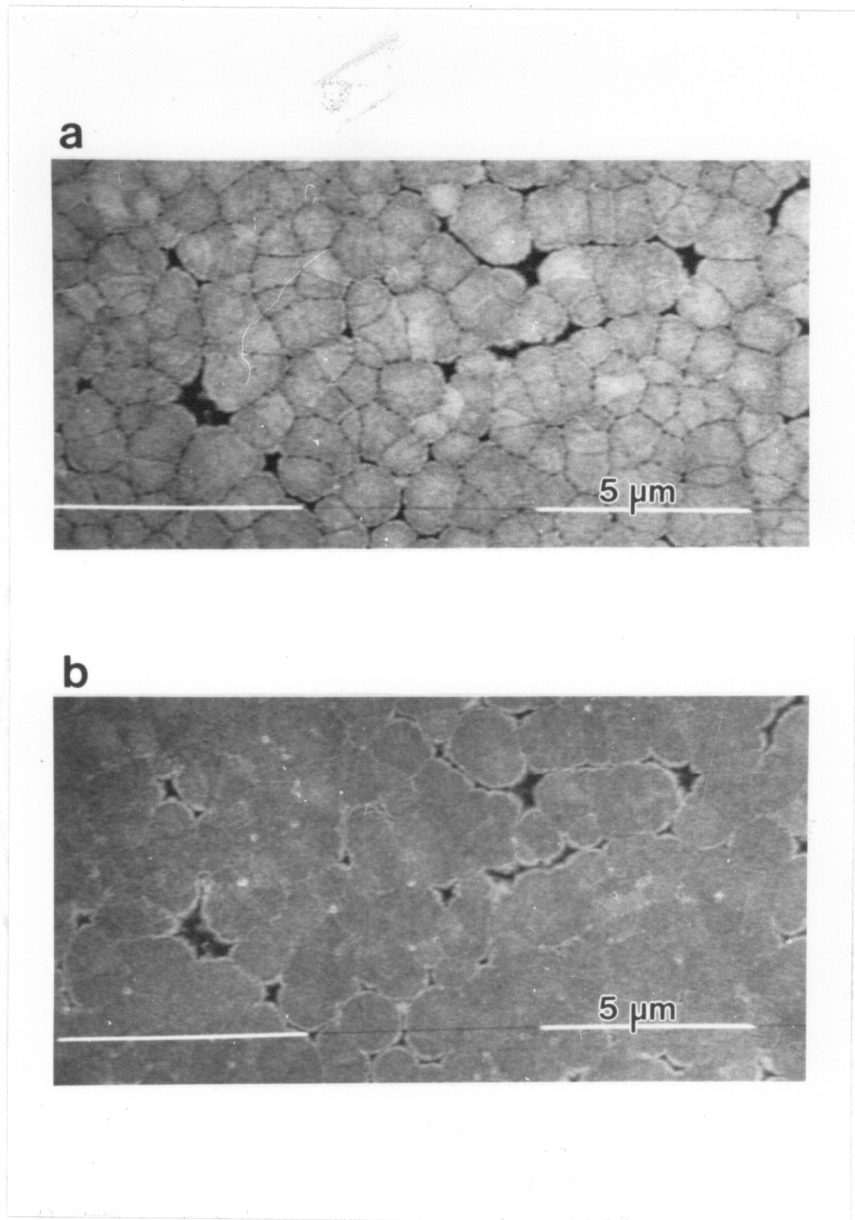


Figure 4.5 STEM micrographs of the PNZT (1/50/50) film on a Pt substrate, annealed at 700°C for 1 hour: (a) a combination image obtained from both backscattering electrons and secondary electrons and (b) a micrograph obtained from backscattering electrons.

image contrast between the interior perovskite grain and the surrounding pyrochlore phase. This indicates that the composition of the pyrochlore and perovskite phases are almost the same. Kwok et al. [38] also observed that there is essentially no change in the compositions between pyrochlore and perovskite phases in sputtered PZT films. These results imply that the MOD process offers a good stoichiometric control and the selection of starting materials in this study is satisfactory with respect to the compositional control requirements.

Energy dispersive x-ray analysis (EDX) of compositional heterogeneity indicates that there is no significant compositional difference between the interior of the grain and the grain boundary region. For the PLZT system, it is necessary to deconvolute the overlapping of Ti-K and La-L peaks to obtain compositional information. Since the probe size of EDX is very large compared to the grain boundary thickness, this investigation does not eliminate the possibility of grain boundary segregation in these films.

4.3 Microstructure

The microstructure of the PZT films was found to be dependent on the type of precursors, dopants and substrates used. Schwartz et al. [58] and Kwok [20] have observed that the mixing order of the individual components of the precursor solution dramatically affect the film microstructure. Desu et al. [65] observed a linear relationship between film thickness and average grain size in sputtered PZT films. The substrate effects have been found in our previous study [50] and will be discussed in detail later in the section 4.8.2. Other parameters such as thermal

processing conditions also have significant influence on the microstructure [66]. To minimize the effects of other parameters like substrate, thickness and thermal processing, films of the same thickness were made on sapphire substrates using the same thermal processing steps. The parameters varied were the dopant type and dopant concentration.

The effect of dopants on the average grain size and morphology of undoped and doped PZT films on sapphire substrates was determined by using optical microscopy and SEM. Detailed microstructure was examined in free-standing TEM samples by TEM. The phase identification in the TEM specimens was performed by using electron diffraction patterns. XRD was used to determine the structure changes of the film on sapphire substrates as a function of annealing temperature.

Figure 4.6 shows the typical XRD patterns of undoped PZT films on sapphire substrates annealed from 300°C to 700°C. All the films were annealed in a box furnace. The film thickness is about 300 nm thick as determined by the analysis of UV-VIS-NIR transmittance spectrum. As observed, at 500°C, only the pyrochlore phase is present while at 550°C both pyrochlore and perovskite phases are found. The transformation from pyrochlore to perovskite is completed between 575°C and 600°C, after which only the perovskite is present. Therefore, the T_i^{Per} and T_c^{Per} were determined to be 550°C and 600°C, respectively, under these conditions.

Figure 4.7 shows the average grain size as a function of dopant type and dopant concentration. All the films were annealed at 650°C to complete the

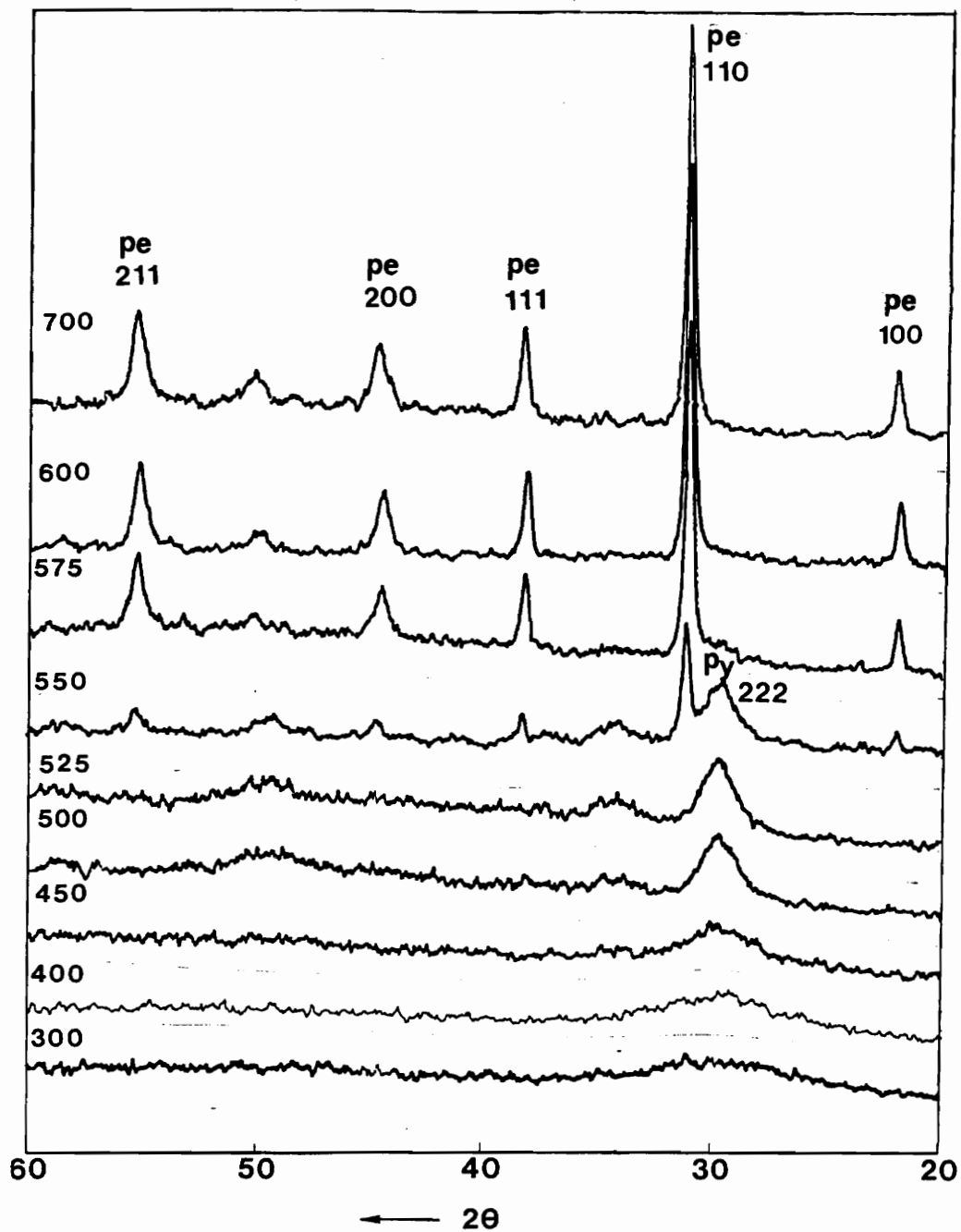


Figure 4.6 Typical XRD patterns of undoped PZT films on sapphire substrates annealed at the temperature ranged from 300°C to 700°C.

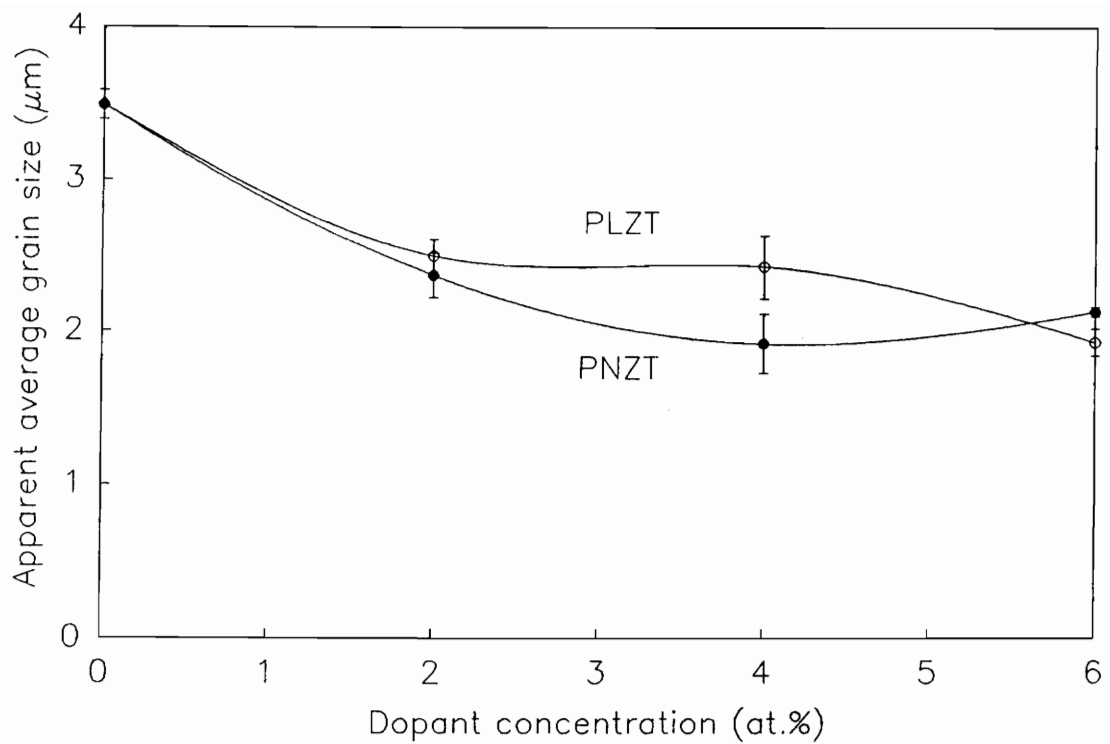


Figure 4.7 The average grain size as a function of dopant concentration in PLZT and PNZT thin films on sapphire substrates.

formation of perovskite. Grains having spherulite structure are observed in PLZT films and PNZT films with Nd content less than 4 at. % on sapphire substrates, whereas well-developed grains are found in Nd-doped PZT films above 4 at.% of Nd content. Similar to bulk materials, in PLZT thin films the average grain size also decreases with increasing La concentration. This result is expected because lanthanum is known to promote the uniform grain growth and homogeneous densification of a single phase. For Nd-doped PZT films, the average grain size is found to be decrease for Nd content up to 4 at.%. This observation is in contrast with the results of the study by Tandon et al. [24], where the average grain size of PNZT ceramics increased with increasing Nd concentration when small amount of Nd was added.

A TEM micrograph (Figures 4.8(a)) shows a bright field image of the coexistence of both pyrochlore and perovskite phases in the PNZT (2/50/50) film, annealed at 650°C for 15 minutes. The well-developed grains in Figure 4.8(a) are identified as the perovskite phase from its definite spot diffraction pattern, shown in Figure 4.8(b), whereas the fine grains as the pyrochlore phase from its ring diffraction pattern, shown in Figure 4.8(c). The measured d spacings of both pyrochlore and perovskite phases are similar to those data determined by the x-ray diffraction method. The incompleteness of perovskite phase as observed in TEM might be related to the size effect in the thin film. Since the film was made without any supporting substrate, the characteristics of this unstrained free-standing film are different from the film deposited on a substrate. Due to the fact that the strain relief can easily occur in the free-standing film by shrinkage or by formation of bending contours, the strain energy required for the phase transformation from

PNZT (2/50/50) 650°C, 15 min.

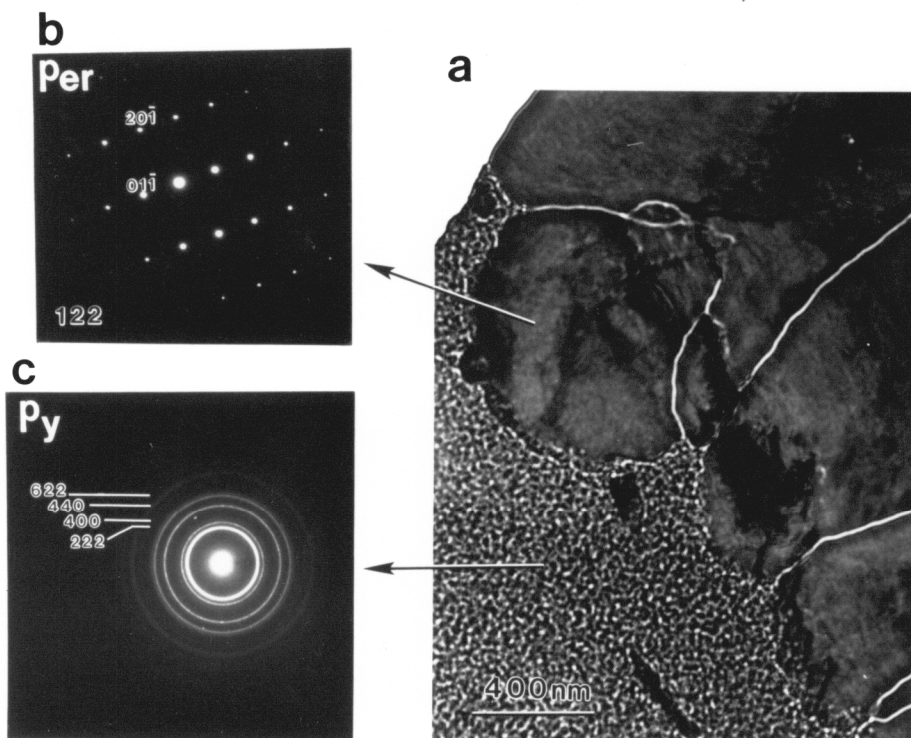


Figure 4.8 Transmission electron micrographs of the MOD PNZT (2/50/50) film, annealed at 650°C for 15 minutes, show the coexistence of pyrochlore and perovskite phases: (a) bright field image, (b) selected area diffraction patterns of perovskite and (c) pyrochlore phases.

pyrochlore to perovskite is reduced. Hence, the presence of pyrochlore was still observed in TEM specimens annealed at 650°C although the completion formation temperature of the perovskite phase is found to be 600°C for the film on sapphire substrates. This result is in a good agreement with the sol-gel film [31], for which the transformation temperature of perovskite phase in the free-standing film was found to be higher than that in the film with substrate. The TEM micrograph of the specimen annealed at 500°C for 15 minutes, for which only the pyrochlore phase with fine grains is present is shown in Figure 4.9. The measured pyrochlore grain size is around 8 nm, which is the same as that of sol-gel films (8 nm) [31] but larger than that of sputtered films (25 nm) [38]. Also, the lattice parameter of pyrochlore phase determined from the selected area ring diffraction pattern is about 10.47 Å.

The microstructure of the PZT film is also dependent on the annealing conditions such as temperature and temperature ramp. Figures 4.10(a) and (b) show the microstructures of PZT (50/50) films on sapphire substrates annealed at 650°C for 30 minutes in a box furnace (with a slow heating/cooling cycle) and a tube furnace (with a fast heating/cooling cycle), respectively. As can be seen, the low annealing cycles tends to form film with a spherulite perovskite structure with a second phase between grains, whereas homogeneous grain formation is observed in the case of fast annealing cycle. The second phase in Figure 4.10(a) is identified to be the pyrochlore phase from the results of the TEM study. Spierings et al. [67] have also shown that the morphology of the PZT film is strongly influenced by the heating cycle. One of the explanations for this behavior could be that the slow growth of perovskite gradually concentrated the impurities from the starting materials. Other possible source of impurities from the bottom electrode and/or the

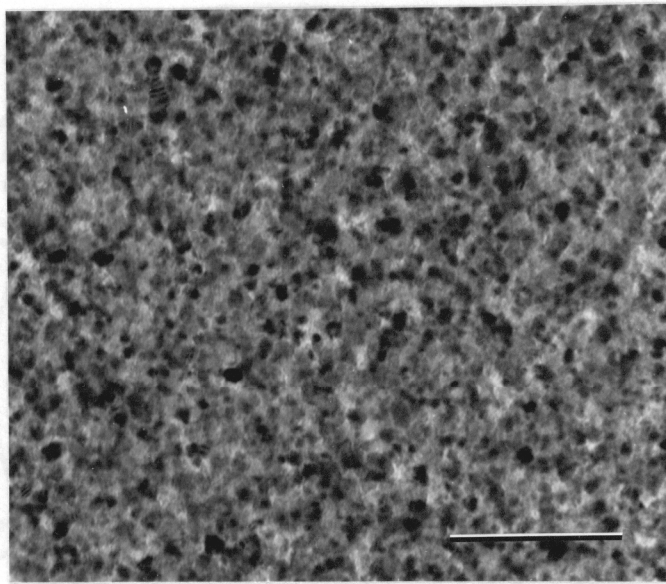
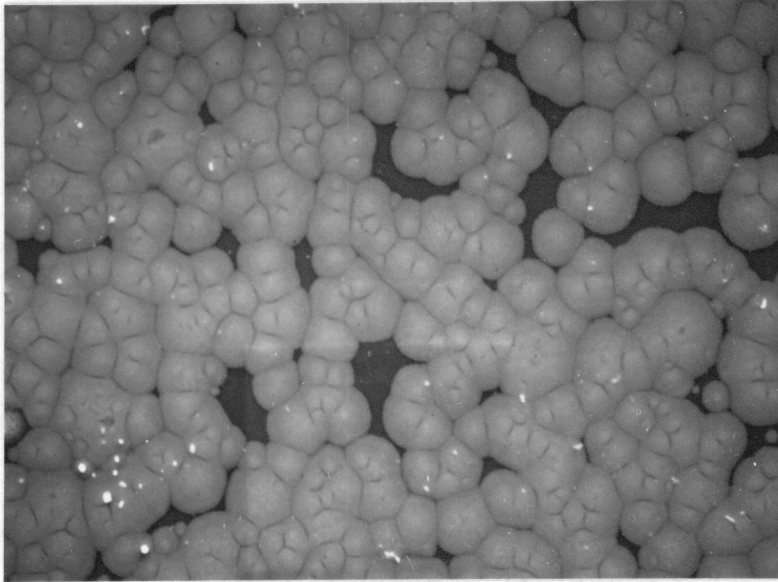


Figure 4.9 A transmission electron micrograph of PNZT (2/50/50) film, annealed at 500°C for 15 minutes (bar = 100 nm).

a



b

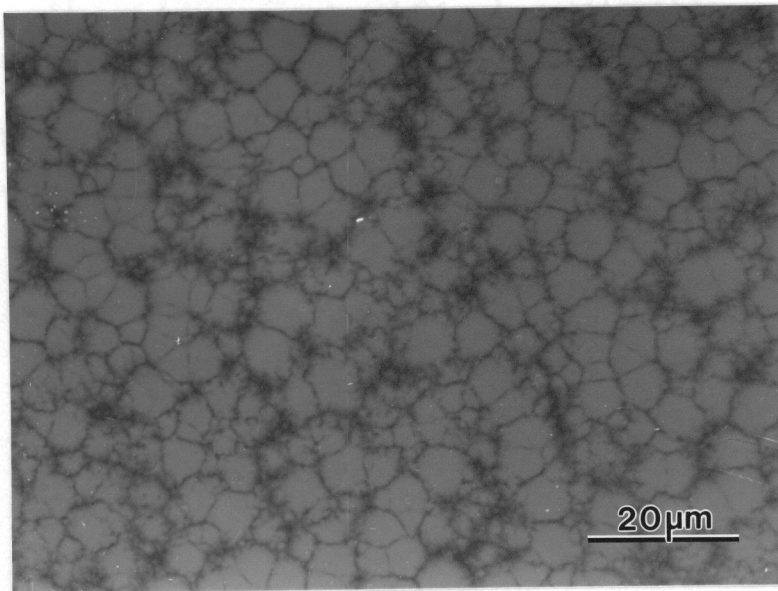


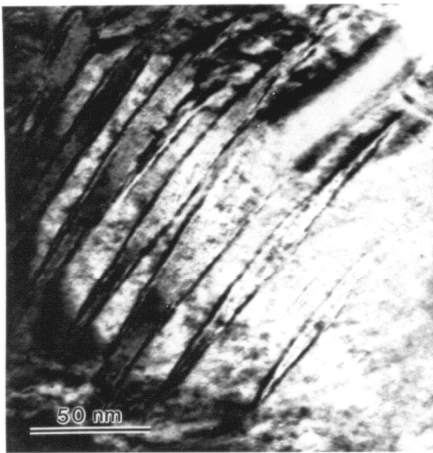
Figure 4.10 Microstructures of PZT (50/50) films on sapphire substrates annealed at 650°C for 30 minutes in (a) a box furnace and (b) a tube furnace.

buffer layer through any pinholes in the thin bottom electrode were eliminated in the film on sapphire substrate with the absence of electrodes. Further, smaller average grain size and more uniform grain size distribution were observed in fast-annealed films. Therefore, the fast heating rate has to be chosen as one of the key processing parameters in order to obtain the better microstructure of the film.

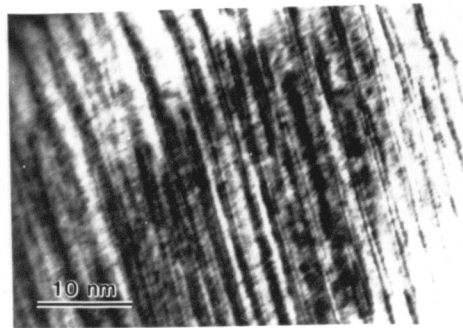
4.4 Domain Structure

The domain structure of doped and undoped PZT films was studied using TEM. Similar to most TEM studies on PZT films, we also only observed 90° domains in all TEM specimens. The typical domain structure of undoped PZT thin foils is shown in Figures 4.11(a). The measured average grain size and average domain width are 200 nm and 15 nm, respectively. For comparison, the domain structure of 2 at.% La and Nd-doped PZT thin foils was also investigated as shown in Figures 4.11(b) and (c). The measured domain width of PLZT (2/50/50) and PNZT (2/50/50) are 12 nm and 9 nm, respectively. From the observations of TEM studies, the decrease in the domain size of PZT thin foils by adding dopants might be related to the different crystal tetragonality factor (c/a ratio) of the tetragonal phase [68]. Hence, control of the domain structure can be achieved by the selection of substitutional impurities. However, since the domain size has to be measured when the domain is tilted parallel to the domain orientation, the image of inclined domain only reflects the projected value of the real domain width. Additionally, domain formation is energetically unfavorable when the grain size is below a certain value.

a PZT(50/50)



b PLZT(2/50/50)



c PNZT(2/50/50)

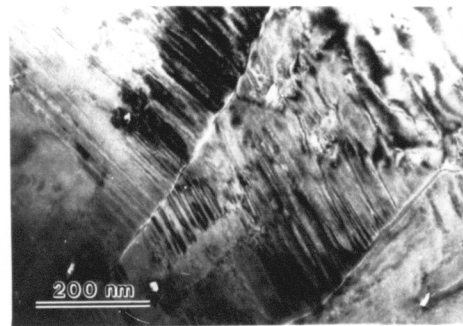


Figure 4.11 The domain structure of (a) PZT (50/50) (b) PLZT (2/50/50) and (c) PNZT (2/50/50) thin foils.

4.5 Dopant Effect on Curie Temperature and Crystal Tetragonality

Hot-stage TEM investigation of the thin foils was carried out to understand the effects of dopant concentration on both the Curie temperature and temperature variation of crystal tetragonality (c/a ratio).

4.5.1 Effect on Curie Temperature

Hot-stage TEM investigations have been used earlier for bulk ceramics in determining the Curie temperature for La-doped and undoped PbTiO_3 [68] and PZT [29,30] materials; however, very little has been applied to PZT films [38]. Using the fact that domains only exist in the ferroelectric phase, the Curie temperature was obtained by heating the ferroelectric film, in-situ in TEM, until the domain structure disappeared. Similarly, while cooling from above the domain structure reappeared below the Curie temperature. An example of the disappearance and appearance of domain during heating and cooling is shown in Figures 4.12(a)–(d) for PZT (50/50) thin foils. In in-situ TEM, the ferroelectric PZT thin foil, annealed at 650°C for 15 minutes, shows the domain structure at room temperature (Figure 4.12(a)). When the specimen was heated up to 305°C (Figure 4.12(b)), the domain started to disappear in the thinner area of the foil. The domain completely disappeared due to the film heated over the Curie temperature (390°C) (Figure 4.12(c)), but it reappeared upon cooling to room temperature (Figure 4.12(d)). The Curie temperature of the PZT (50/50) thin foil determined by the hot-stage TEM is 378°C . The domain configurations observed

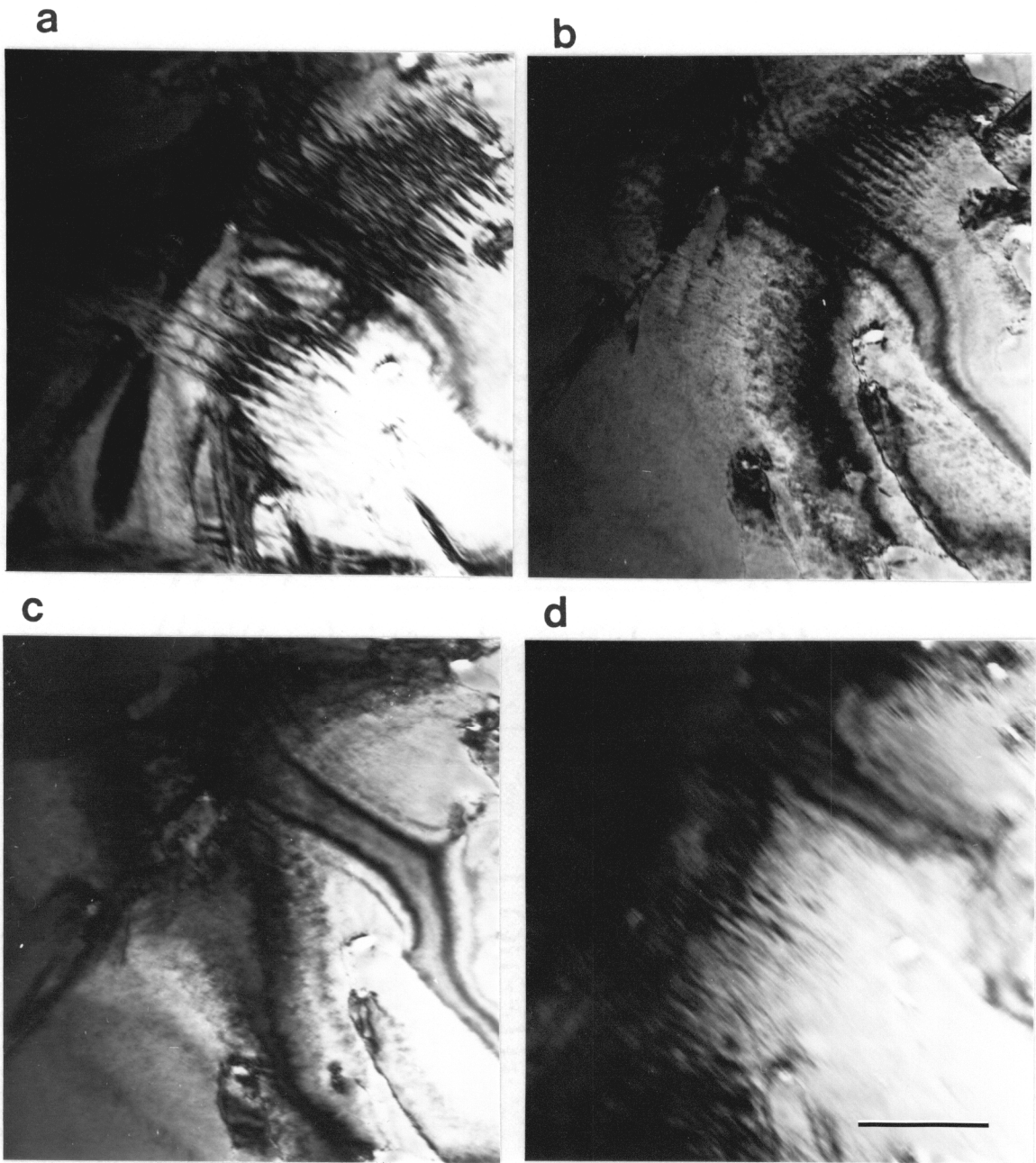


Figure 4.12 Transmission electron micrographs of the PZT (50/50) thin foil showing the presence of domain structure at (a) 25°C and (b) 305°C, the disappearance at (c) 390°C upon heating, and the reappearance at (d) 25°C after cooling (bar = 300 nm).

above and below the Curie temperature are similar, indicating a reversible behavior of the transformation.

Using the observation of the disappearance of the ferroelectric domain during heating, in-situ in TEM, the Curie temperatures of PLZT and PNZT thin foils with various dopant concentrations were determined and are listed in Table 4.3. For comparison, the Curie temperatures of corresponding bulk materials derived from MOD PLZT powders were determined by the traditional dielectric property measurement at frequencies of 1, 10 and 100 kHz, i.e. dielectric constant versus temperature, and are also shown in Table 4.3. Along with experimental data, Table 4.3 also lists the literature data for bulk samples reported by Haertling et al. [47] for PLZT (Table 4.3).

The following conclusions can be made from the data in Table 4.3: (1) the Curie temperature decreases with increasing dopant concentration for both thin foils and bulk ceramics, (2) for a given dopant concentration, Curie temperatures of Nd-doped samples are lower than those of La-doped specimens, (3) for a given composition, the Curie temperatures of thin foils are consistently lower than those of bulk ceramics, and (4) the experimental data agrees well with the available data from literature. The variation of Curie temperature with both the nature and the amount of the dopant is related to the crystal tetragonality factor; this will be discussed later in detail. The lower Curie temperatures for thin foils, when compared to corresponding bulk materials, may be related to the size effects and residual stresses present in the films [20,65]. Additionally, since the TEM specimens is very thin (about 5 to 10 nm), this investigation can not avoid the possibility of

Table 4.3 Comparison of Curie temperature of PLZT and PNZT thin foils obtained by hot-stage TEM method with those of PLZT bulk ceramics.

Curie temperature ($^{\circ}\text{C}$)						
La (at.%)		Bulk ceramics			Thin foils	
	[47]	1kHz	10kHz	100kHz	TEM	
0	407	396	395	394	378	
2	366	374	372	371	341	
4	324	356	355	354	316	
6	276	318	317	316	252	
Nd (at.%)					Thin foils	
2					335	
4					293	
6					236	

heating effects by electron beam in TEM.

4.5.2 Effect on Crystal Tetragonality

For thin foils, the values of the crystal tetragonality factor at room temperature, determined from the electron diffraction studies as a function of the nature and amount of dopant, are shown in Figure 4.13. The value of the crystal tetragonality factor decreased with increasing dopant concentration (Figure 4.13). It can also be seen from Figure 4.13 that for a given dopant concentration, the tetragonality factor is lower for Nd-doped samples than that of La-doped samples.

As in bulk materials, it is assumed that both La^{3+} and Nd^{3+} will act as donors and occupy the A sites of the ABO_3 perovskite lattice in PZT films. Additionally, it is expected that introducing La^{3+} and Nd^{3+} dopants will reduce the crystal tetragonality of PZT films on the basis of ionic radii values (1.32, 1.22 and 1.15 Å, respectively for Pb^{2+} , La^{3+} , and Nd^{3+}) [69]. Based on the relative ionic sizes, the decrease in the value of the tetragonality factor with increasing dopant concentration can be easily explained. Since the ionic size of Nd^{3+} is smaller than that of La^{3+} , it is understandable that, for a given concentration, the tetragonality factor for Nd-doped samples is smaller than that of La-doped specimens.

For bulk La-doped PbTiO_3 materials, Yamamoto et al. [70] have shown a linear relationship between the crystal tetragonality factor and the Curie temperature. Similar to their results on bulk materials, in this study, it has been also observed a linear relationship between Curie points and crystal tetragonality

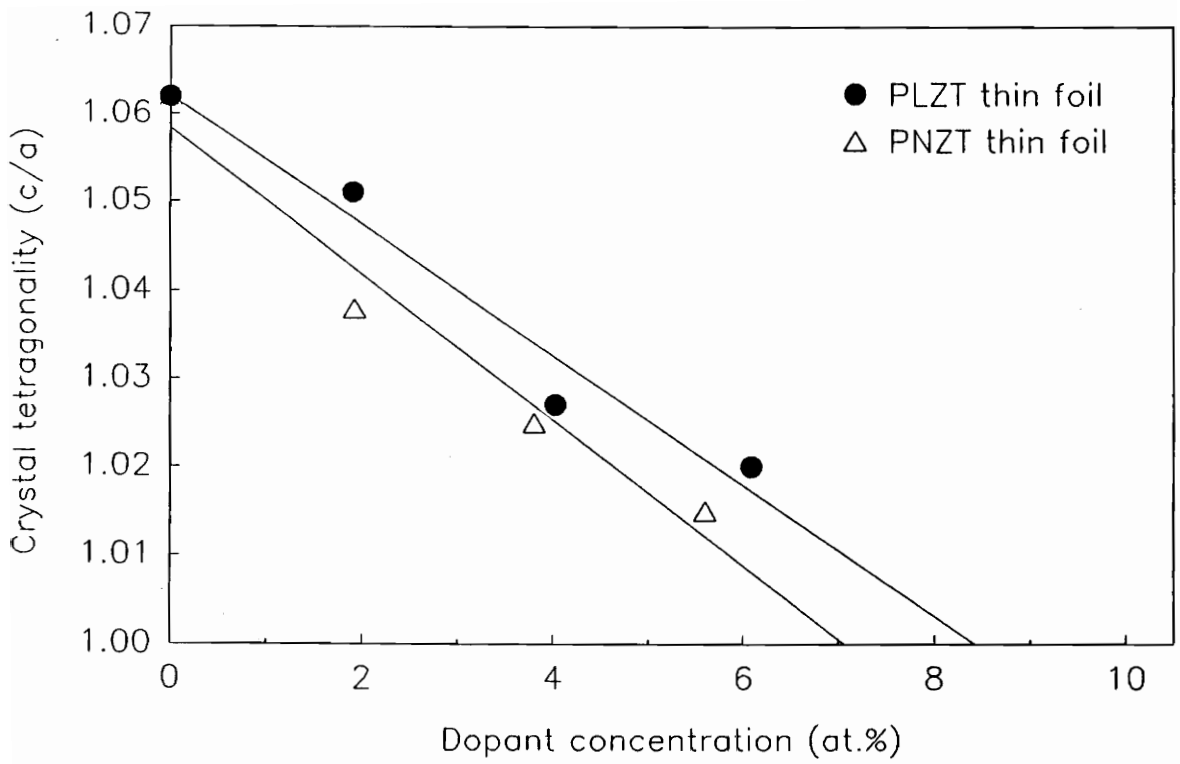


Figure 4.13 The crystal tetragonality factor of PLZT and PNZT thin foils at room temperature, determined from electron diffraction patterns, as a function of dopant concentration.

values (Figure 4.14) for both PLZT and PNZT thin foils. Based on this relationship, the lower Curie temperatures for Nd-doped samples when compared to La-doped ones can be easily understood.

For measuring the tetragonality factor as a function of temperature, a series of diffraction patterns along $\langle 110 \rangle$ zone axes at different temperatures were taken at the same area of the specimen, because the domain structure of the perovskite phase can be easily observed along $\langle 110 \rangle$ directions. The values of the crystal tetragonality factor (c/a) as a function of temperature for PLZT thin foils, determined from the diffraction patterns, are presented in Figure 4.15. As expected, the tetragonality factor smoothly decreases with increasing temperature and approaches a value of 1.00 at the Curie temperature. For all temperatures below the Curie point, the tetragonality factor decreases with increasing dopant concentration.

4.6 Optical Properties

The refractive index (at $\lambda = 633$ nm) of PLZT and PNZT films as a function of dopant concentration are shown in Figure 4.16. All the films were coated on sapphire substrates and subjected to a final annealing at 650°C for 30 minutes in a tube furnace. Both La and Nd-doped PZT films exhibit higher refractive indices than those of undoped PZT films. As seen in Figure 4.16, the refractive index of the doped PZT films is proportional to the dopant concentration. However, Thacher [71] reported that no significant variation was found on refractive indices of undoped and La-doped PZT ceramics. This implies that in both thin film and bulk

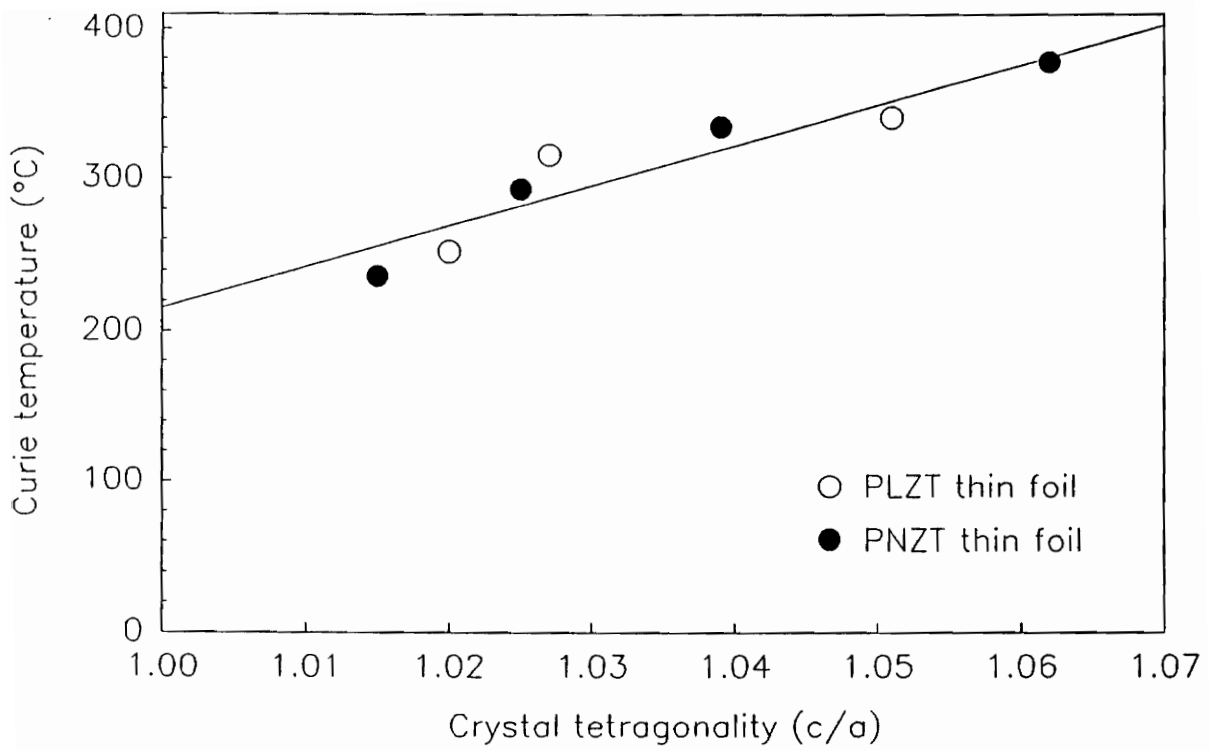


Figure 4.14 The linear relationship between the Curie temperature and the crystal tetragonality factor for PLZT and PNZT thin foils determined by hot-stage TEM.

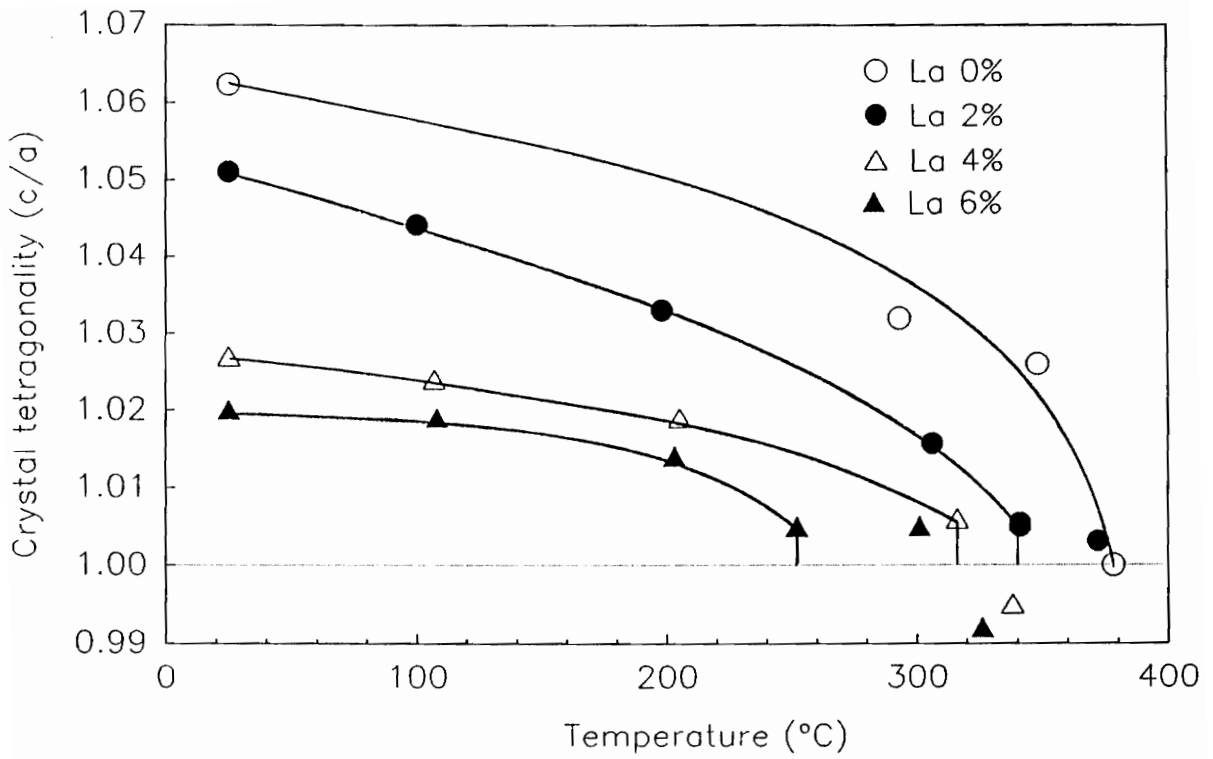


Figure 4.15 The crystal tetragonality factor as a function of temperature for PLZT thin foils determined from the electron diffraction patterns.

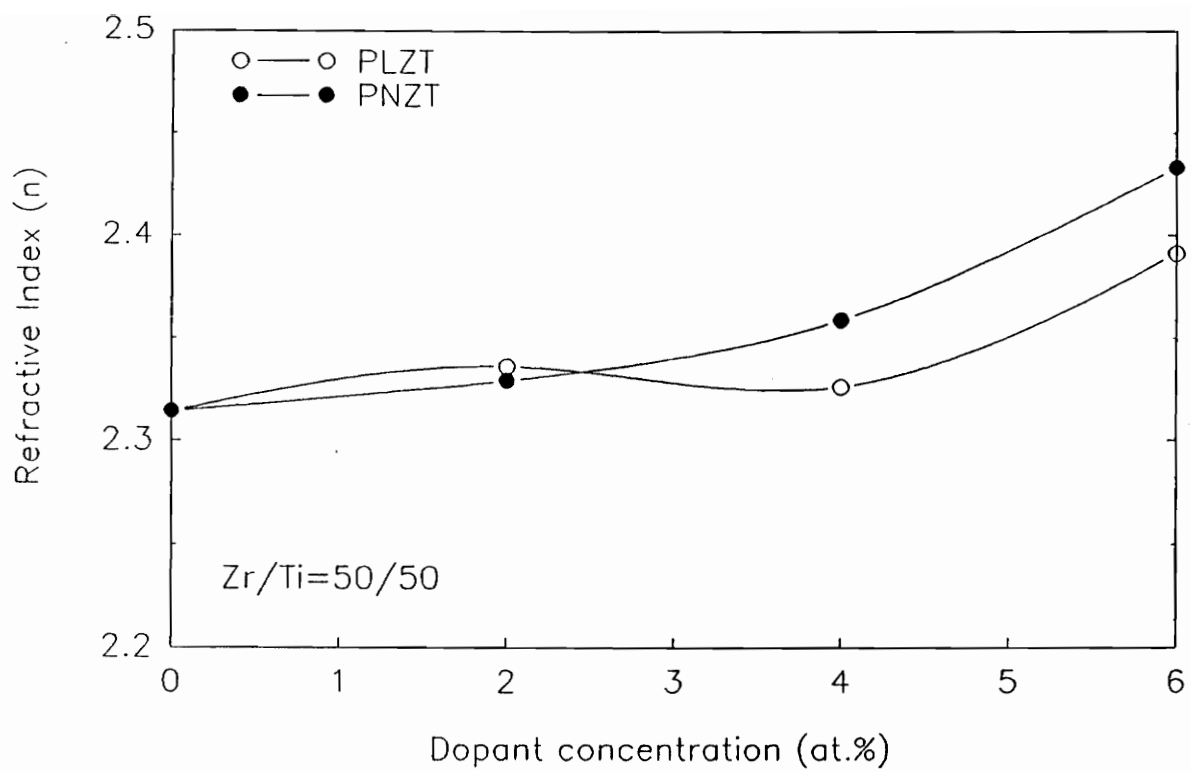


Figure 4.16 The refractive index of PLZT and PNZT films as a function of dopant concentration.

materials dopants do not affect refractive indices of PZT materials. Therefore, the increase in refractive indices with increasing dopant concentration in PLZT films is due to their higher packing densities. The packing densities of undoped and doped PZT films on sapphire substrates are listed in Table 4.4. The higher refractive index and higher packing density obtained in doped PZT films implies that both La^{3+} and Nd^{3+} ions promote the densification of the microstructure. The addition of these dopants may slow the grain growth due to impeding the grain boundary mobility, the grain size thus decreases and porosity removes more readily through grain boundary. This result also implied that the packing density of films prepared by MOD process is competitive with the films prepared by other methods [10]. For La-doped PZT films, the maximum refractive index value (2.43) is close to the value for bulk materials (2.54). The detailed calculations of refractive index, thickness and packing density are listed in Appendix A [59].

4.7 Electrical Properties

The variation of electrical properties with annealing temperature, dopant type, dopant concentration, and film thickness, was investigated in this study. The electrical properties of the films was found to strongly depend on the the parameters mentioned above. The effects of the individual parameter on the electrical properties will be discussed in detail in the subsequent sections.

4.7.1 Effects of Processing Conditions

4.7.1.1 Effect of Annealing Temperature

Table 4.4 Packing densities of undoped and doped PZT films.

	Dopant concentration (at.%)			
	0	2	4	6
PLZT	85.1	86.5	88.0	92.7
PNZT	85.1	86.1	85.9	90.0

Figure 4.17 shows the typical ferroelectric hysteresis loops for PZT thin films annealed at 550°C and 575°C. The applied voltage was 5 volts. The film annealed at 575°C shows a well-saturated hysteresis loop with remanent polarization of 30 $\mu\text{C}/\text{cm}^2$ and coercive field of 70 kV/cm while at 550°C a linear relationship between polarization and applied electric field is observed. The values of the ferroelectric properties obtained are typical of PZT films for the 300 nm thickness on Pt electrodes. The x-ray data have shown that the initiation and completion formation temperatures of the perovskite phase in these films were 500°C and 600°C, respectively. The better ferroelectric properties observed in the film annealed at 575°C with perovskite phase confirms that the tetragonal perovskite structure is highly desirable for ferroelectric materials. In other words, any small amount of nonferroelectric pyrochlore phase remanent in the film after annealing causes the degradation of the ferroelectric properties.

Figure 4.18 shows remanent polarization as a function of annealing temperature for PZT (50/50) films on Pt electrodes. As observed, P_r increases dramatically as the annealing temperature is increased from 550°C to 575°C due to the transformation from the nonferroelectric pyrochlore phase to the ferroelectric perovskite. Beyond 575°C, since the phase transformation is complete, no further improvement in P_r can be seen. In fact, there is slight degradation in P_r possibly due to the interdiffusion between the film and the electrode. Figures 4.19 and 4.20 show the effect of annealing temperature on ferroelectric properties of PZT films of 300 nm thickness on RuO_x electrodes. The increase in the remanent polarization and coercive field with increasing applied voltage is expected since P_r and E_c are strongly influenced by the nucleation, growth and switching characteristics of

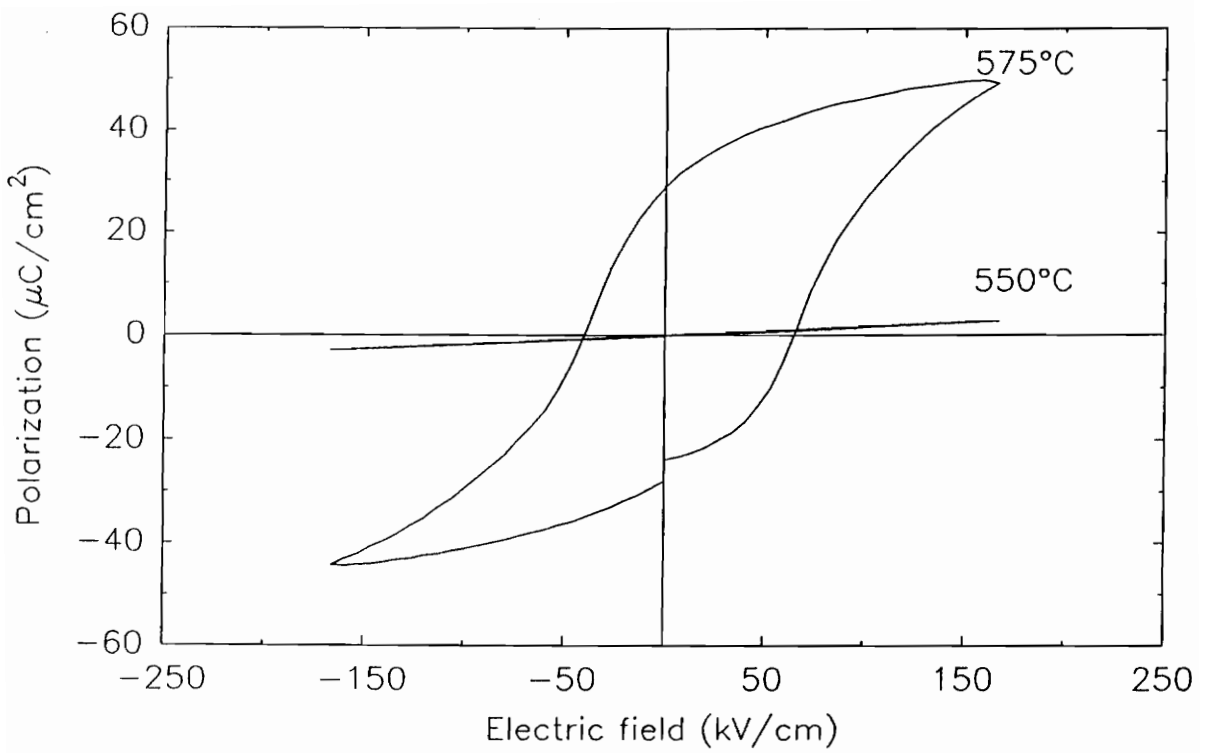


Figure 4.17 Comparison of hysteresis loops for PZT films annealed at 550°C and 575°C.

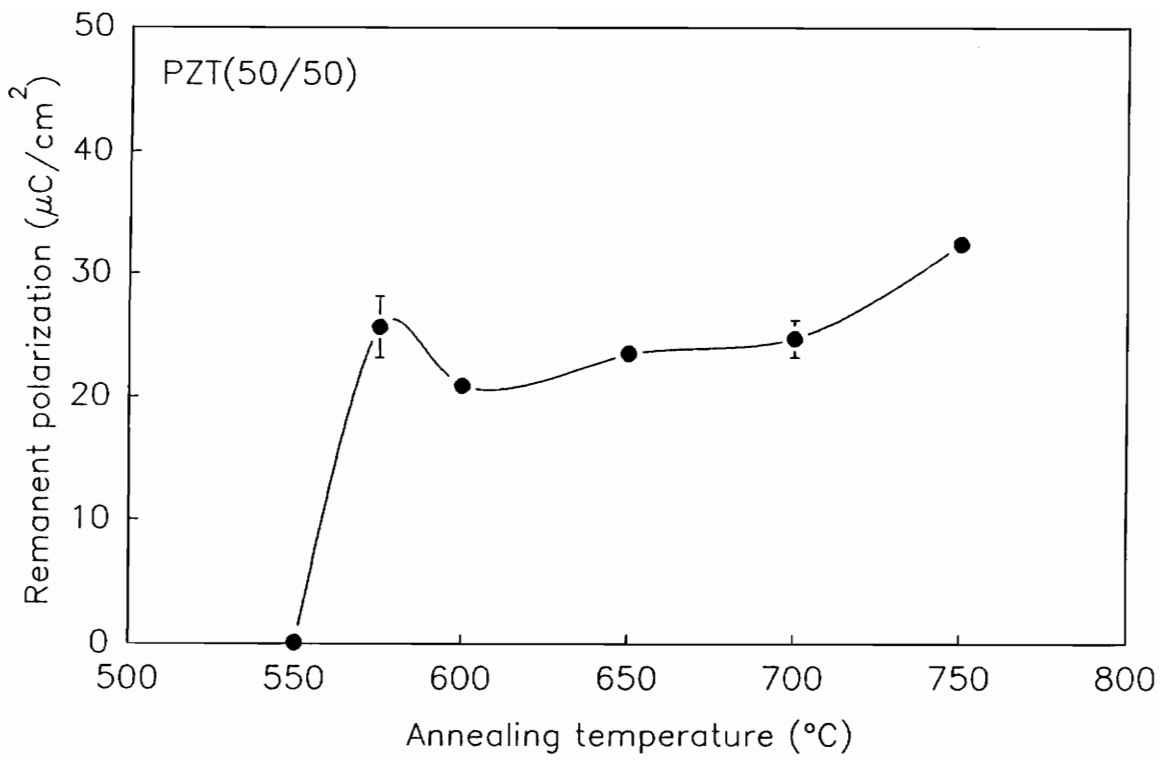


Figure 4.18 Remanent polarization as a function of annealing temperature for PZT films on Pt electrodes.

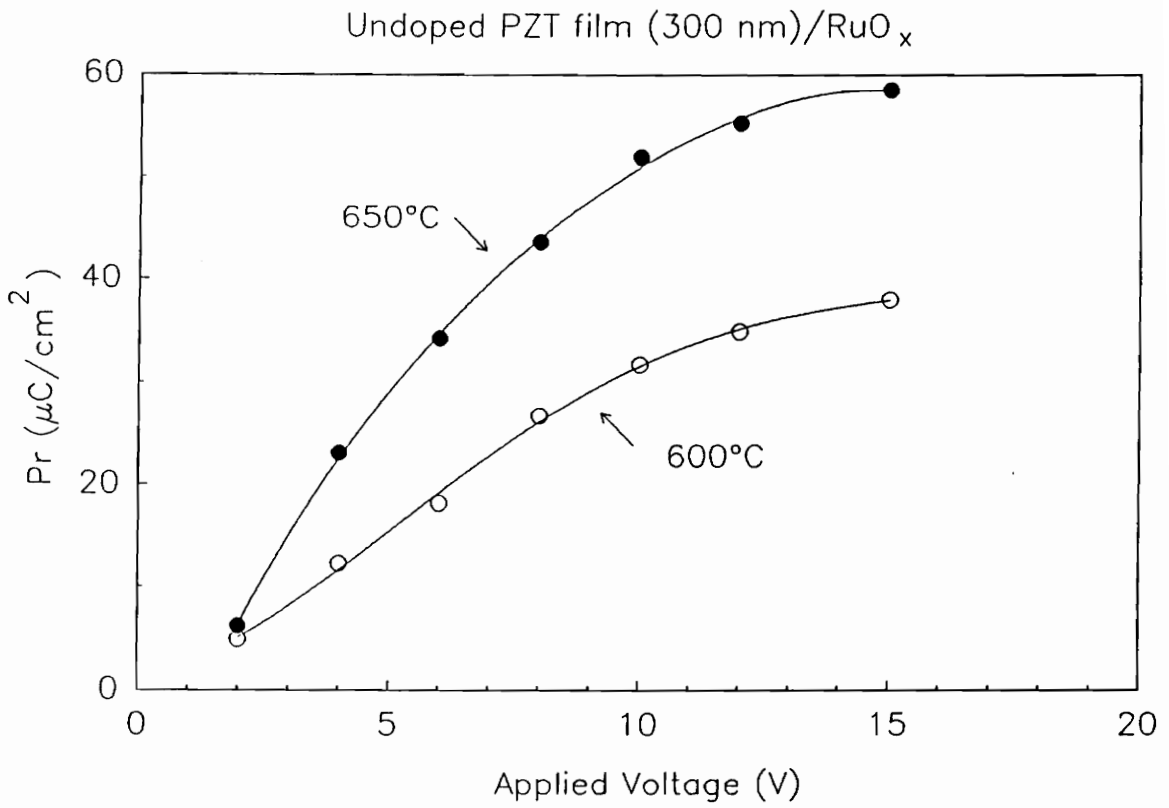


Figure 4.19 Comparison of remanent polarization as a function of applied voltage for PZT films annealed at 600°C and 650°C.

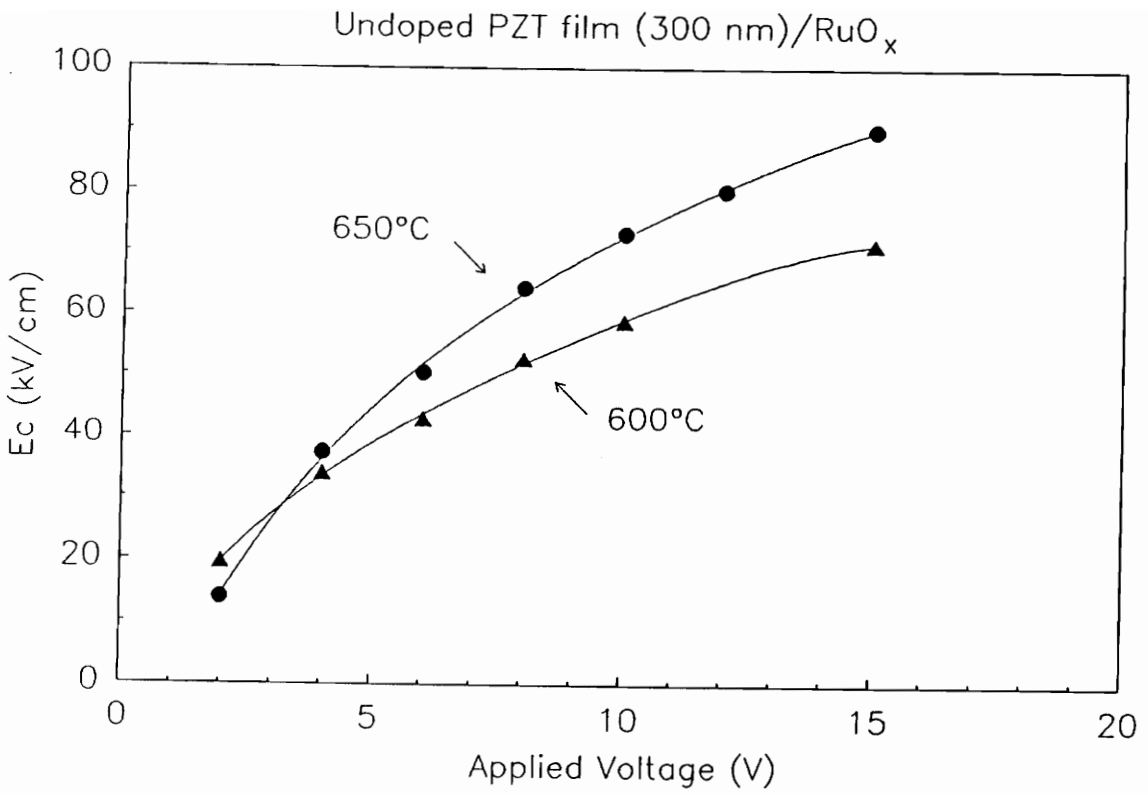


Figure 4.20 Comparison of coercive field as a function of applied voltage for PZT films annealed at 600°C and 650°C.

domains, which in turn are a function of the applied voltage. Higher remanent polarization and coercive field can be seen in the films annealed at 650°C compared to those at 600°C.

The effect of annealing temperature on leakage current was also studied and is shown in Figure 4.21. The 650°C sample exhibits lower leakage current and a gradual slope change in I/V as compared to the 600°C sample. From the view point of the degree of crystallinity, it is believed that the films with amorphous phase are preferable as far as the leakage current is concerned; in addition, the breakdown field of the amorphous films is much larger than that of polycrystalline films [33]. For the PZT films, the x-ray data shows that the film is entirely perovskite phase, without detectable pyrochlore or amorphous scattering when the samples are annealed above 600°C; therefore, it is expected both films annealed at 600°C and 650°C are polycrystalline. The results indicates that the slight improvement in P_r and leakage current is due to the higher density of the film annealed at 650°C. For the film annealed at 650°C, the increase in E_c can be due to following reasons: (1) the thickness variation arising from the annealing temperature and (2) the intermixing between Pb and RuO_x occurs above 650°C according to Rutherford backscattering spectrometry (RBS) results observed by Kwok et al. [18].

Therefore, the annealing temperature is chosen to be above and close to the transformation temperature to optimize the ferroelectric phase formation in the film and to reduce the interdiffusion problem. The annealing temperature of about 50°C above transformation temperature has been recommended to meet the requirements of low temperature processing in semiconductor industry [20].

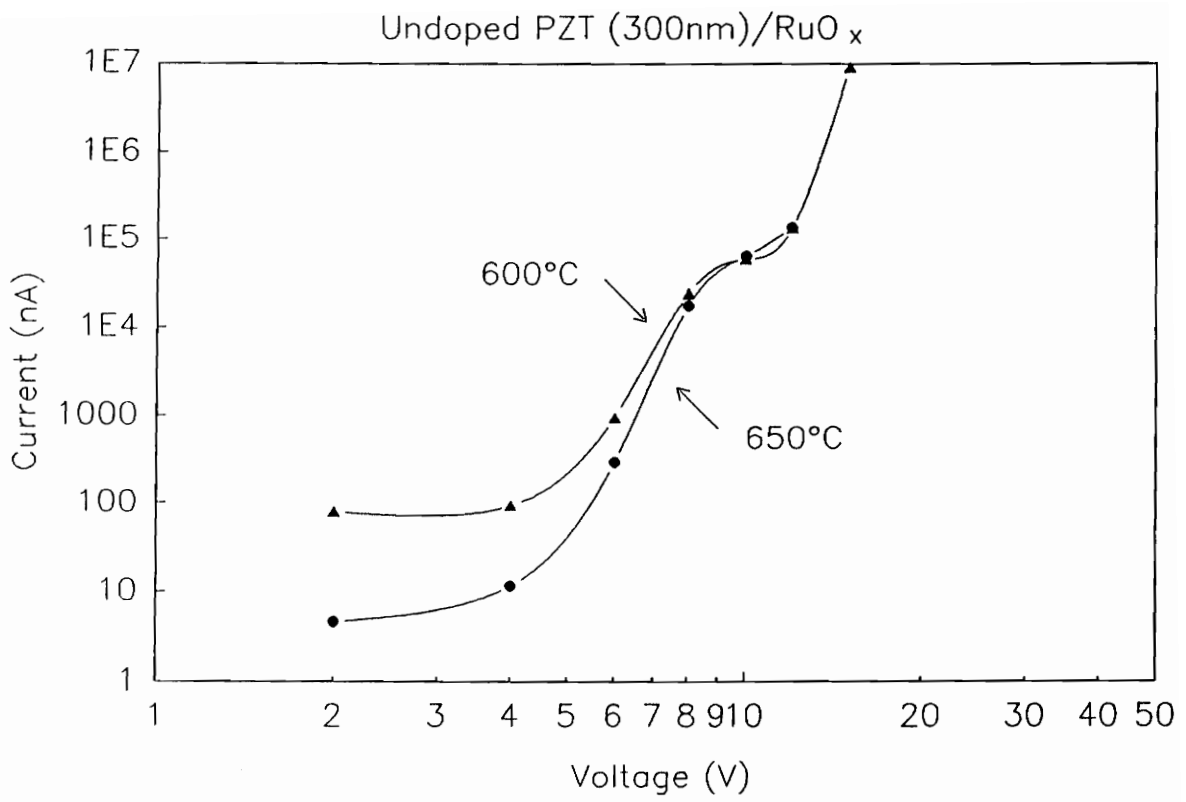


Figure 4.21 Log-log plot of current as a function of voltage for PZT films.

4.7.1.2 Effect of Film Thickness

Figures 4.22 and 4.23 show polarization and coercive field as a function of the thickness of PZT films, respectively. The film thickness ranging from 300 nm to 600 nm were fabricated by controlling the spin speed and the number of coatings. All the films were annealed at 650°C for 30 minutes in air. Both P_s and P_r are observed to be almost independent of film thickness while E_c increases with decreasing film thickness. The increase in the E_c with decreasing film thickness can be due to a number of reasons: (1) change in the nucleation and growth kinetics of the ferroelectric domains with changing thickness [72], (2) increasing interfacial effects in the film properties with decreasing thickness [65], and (3) exponential increase in stress of the thin film with decreasing thickness which in turn increases the residual strain energy. A relationship between coercive field (E_c) and film thickness (t) can be expressed by an empirical formula [72]:

$$E_c = a(t)^n \quad (4.1)$$

where E_c is the coercive field (kV/cm), t the film thickness (nm) and a the constant. The log–log plot of E_c as a function of film thickness is shown in Figure 4.24 and n is determined to be -0.7 . Both the leakage current and breakdown field are expected to increase with decreasing film thickness. Similarly, there are minor differences in the hysteresis loop shape with film thickness; for very thin films the loops are less square, and the P versus E slope near E_c is smaller.

4.7.1.3 Effect of Electrode

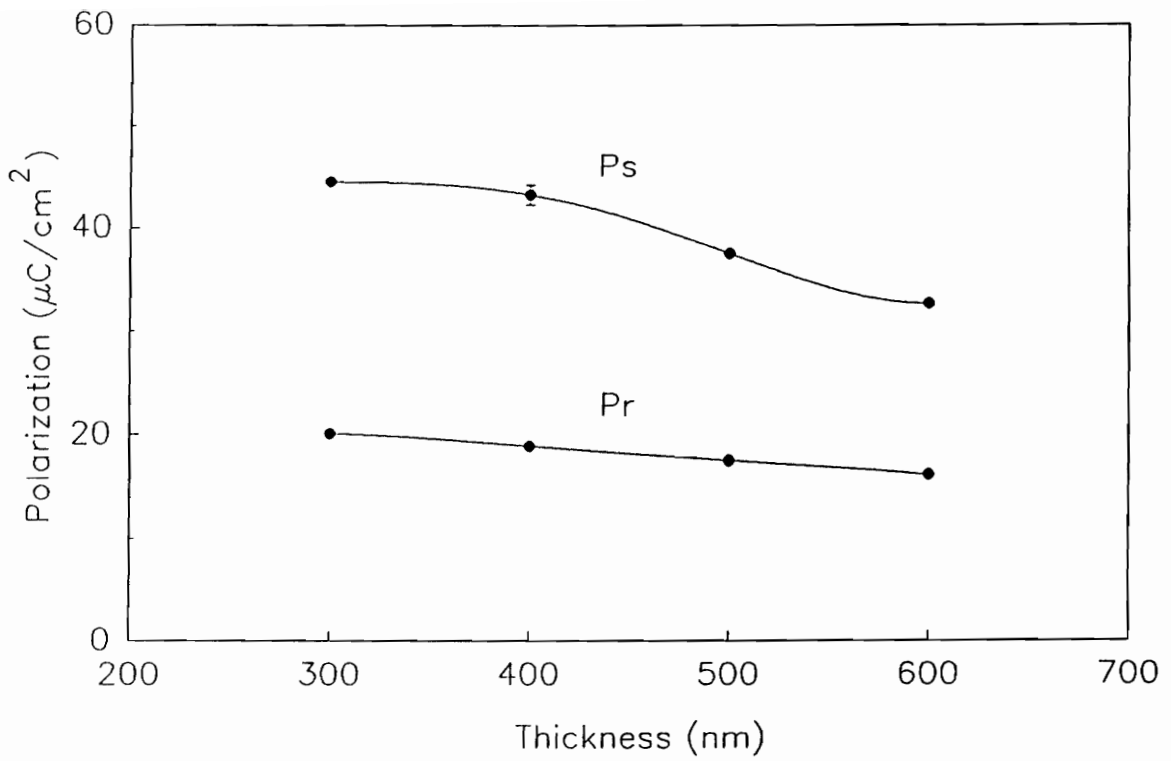


Figure 4.22 Polarization as a function of film thickness for PZT films.

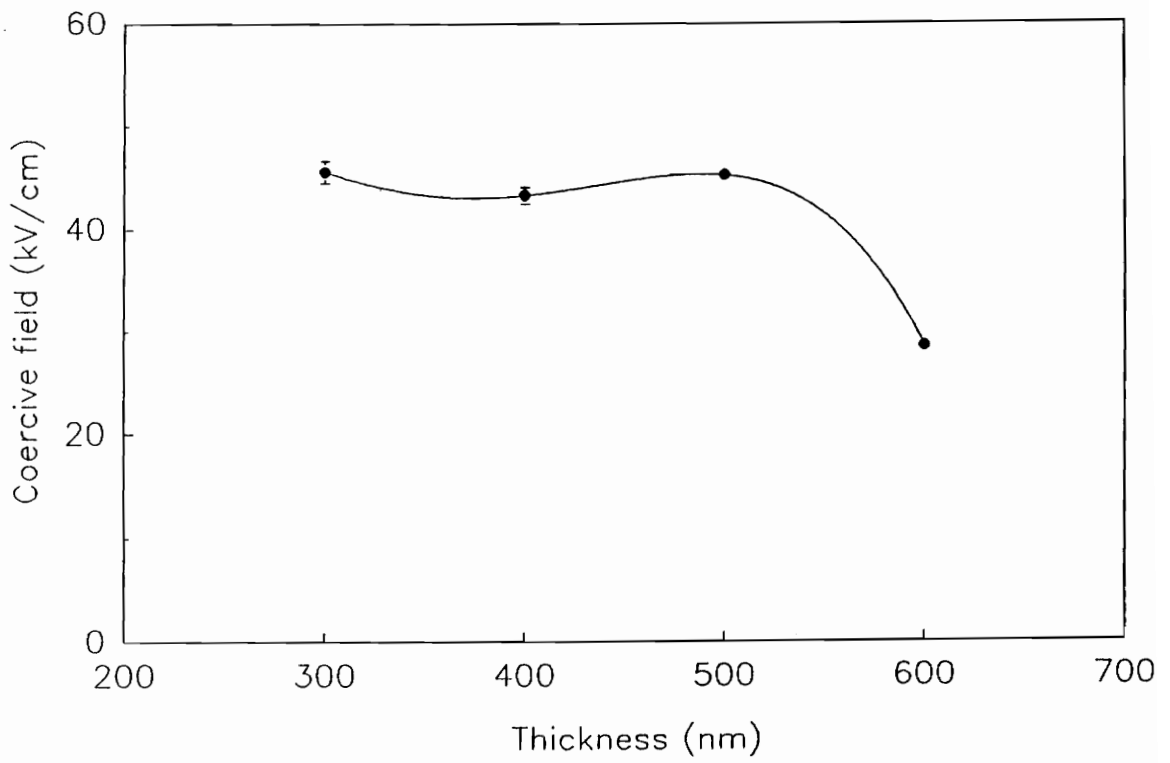


Figure 4.23 Coercive field as a function of film thickness for PZT films.

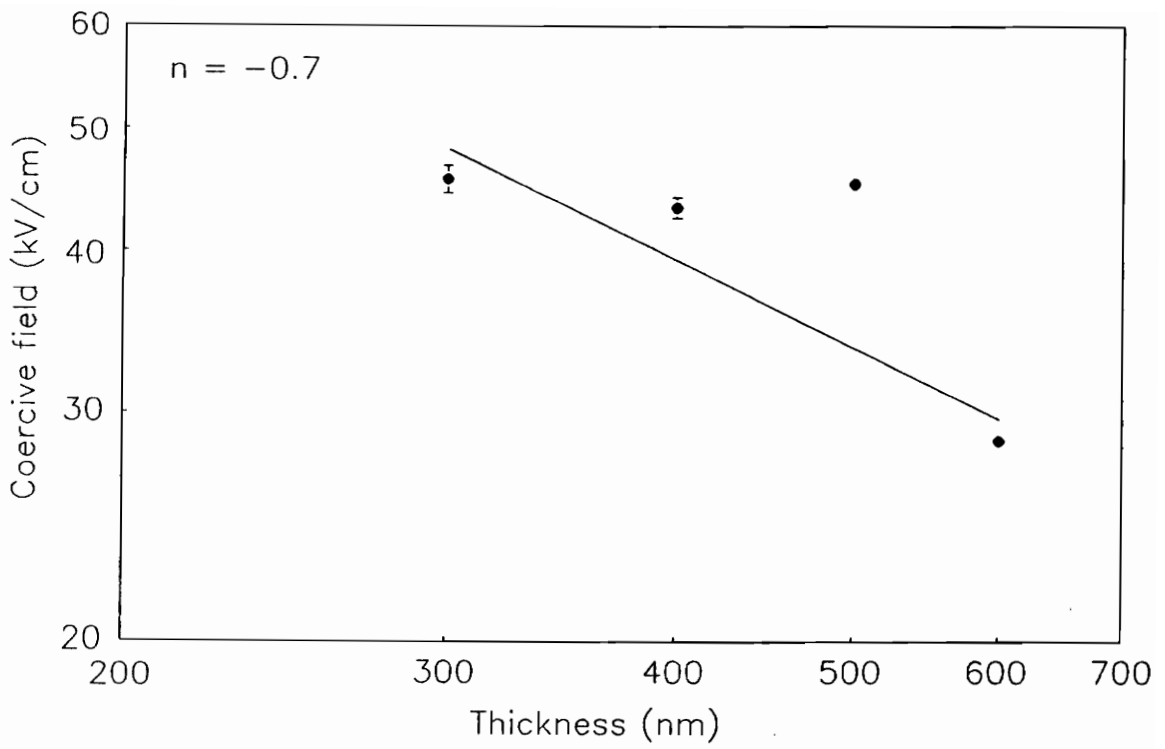


Figure 4.24 Log-log plot of coercive field as a function of film thickness for PZT films.

Figures 4.25 and 4.26 compare remanent polarization and coercive field as a function of applied voltage for undoped PZT films, annealed at 650°C, on RuO_x and Pt bottom electrodes, respectively. Both P_r and E_c are observed to be higher in the films on RuO_x than those on Pt electrodes. Similar results are also observed in Nd-doped PZT films. However, below the applied voltage of 6 volts the difference in the ferroelectric properties for various electrodes is very small. Possible reasons for the different ferroelectric characteristics of the films on RuO_x and Pt electrodes are microstructure variations and/or interfacial effects. Additionally, the effect of electrode on leakage current was studied and is shown in Figure 4.27. As seen in Figure 4.27, below the applied voltage of 5 volts the leakage current of the film on RuO_x is slightly higher than that on Pt electrodes. The film on RuO_x electrodes shows a gradual increase in leakage current above 4 volts while on Pt the leakage current increases slowly up to 9 volts, above which a rapid increase in the leakage current is observed. This result indicates that the films on RuO_x electrodes show improved leakage current characteristics. Higher breakdown voltage is thus expected for the film on RuO_x electrodes. Indeed, Kwok et al. [18] has found the fatigue-free behavior with polarization reversal up to 10⁹ cycles in the PZT films on RuO_x electrodes. For the film on RuO_x, the gradual increase in leakage current is thought to be one of reasons which attribute to the improvement of the fatigue properties.

4.7.2 Dopant Effects

4.7.2.1 Effect on Polarization and Coercive Field

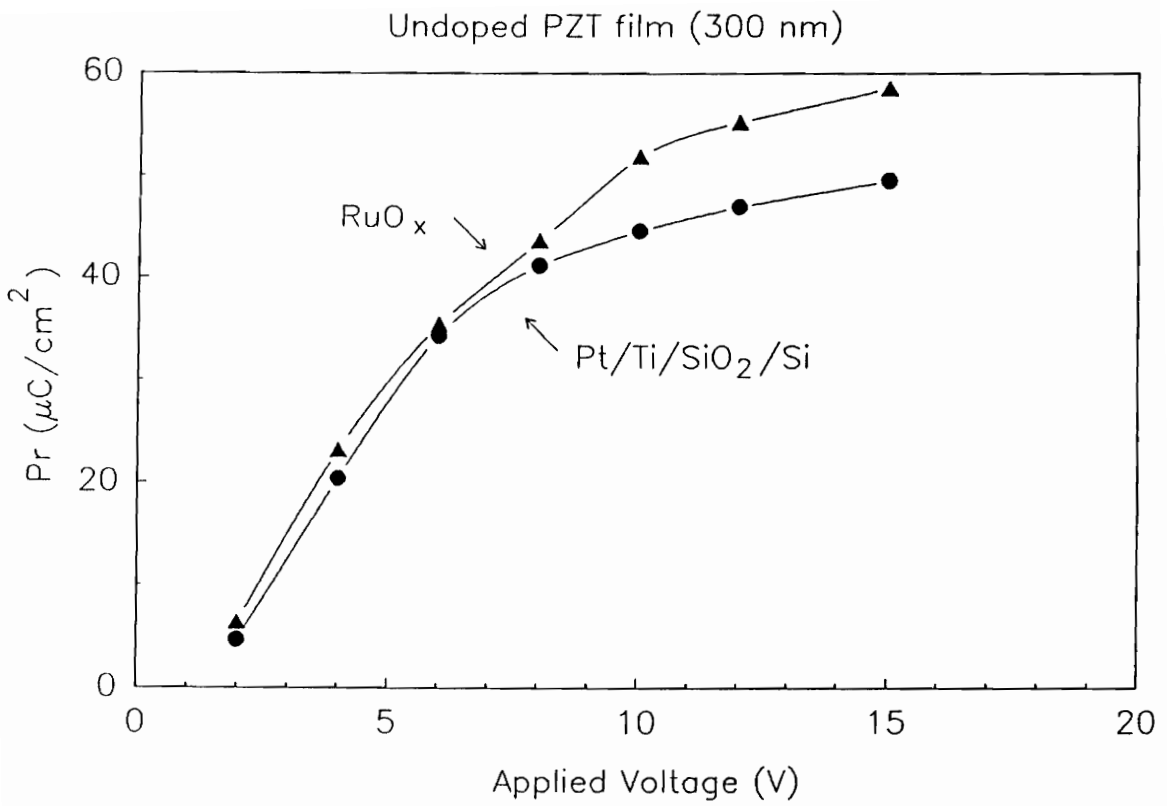


Figure 4.25 Comparison of remanent Polarization as a function of applied voltage for PZT films on RuO_x and Pt electrodes.

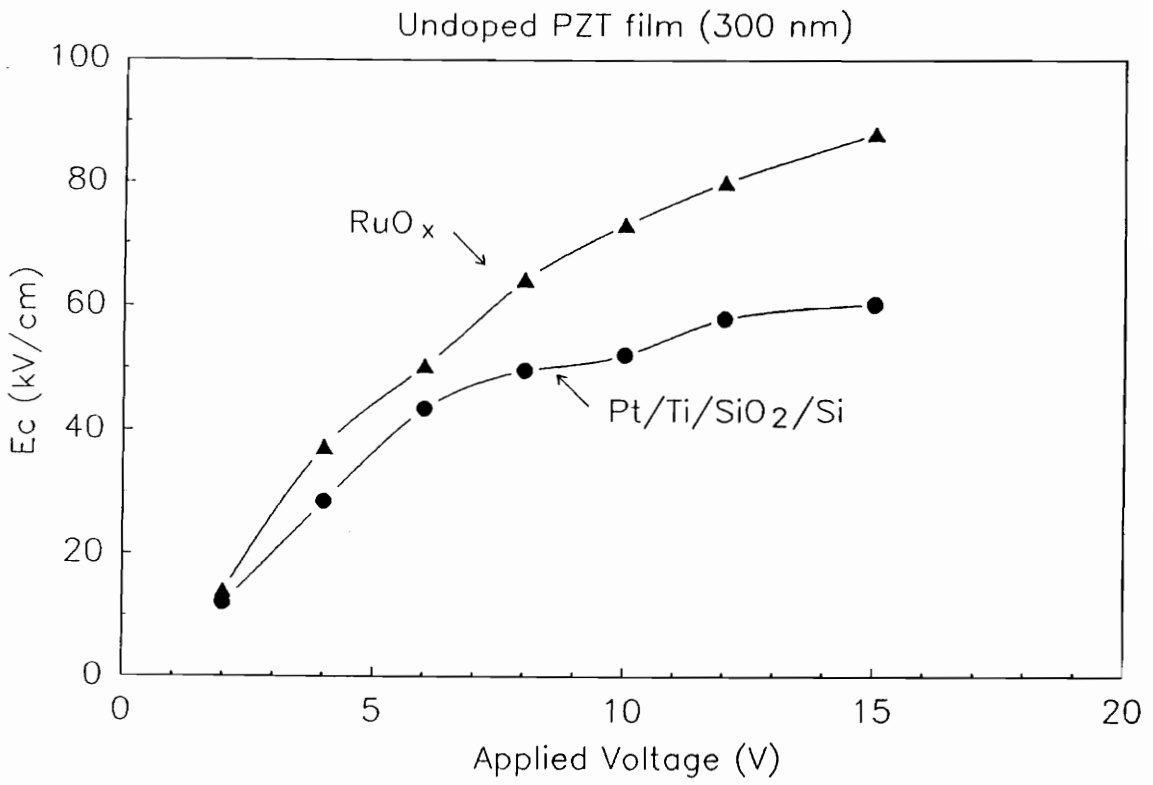


Figure 4.26 Comparison of coercive field as a function of applied voltage for PZT films on RuO_x and Pt electrodes.

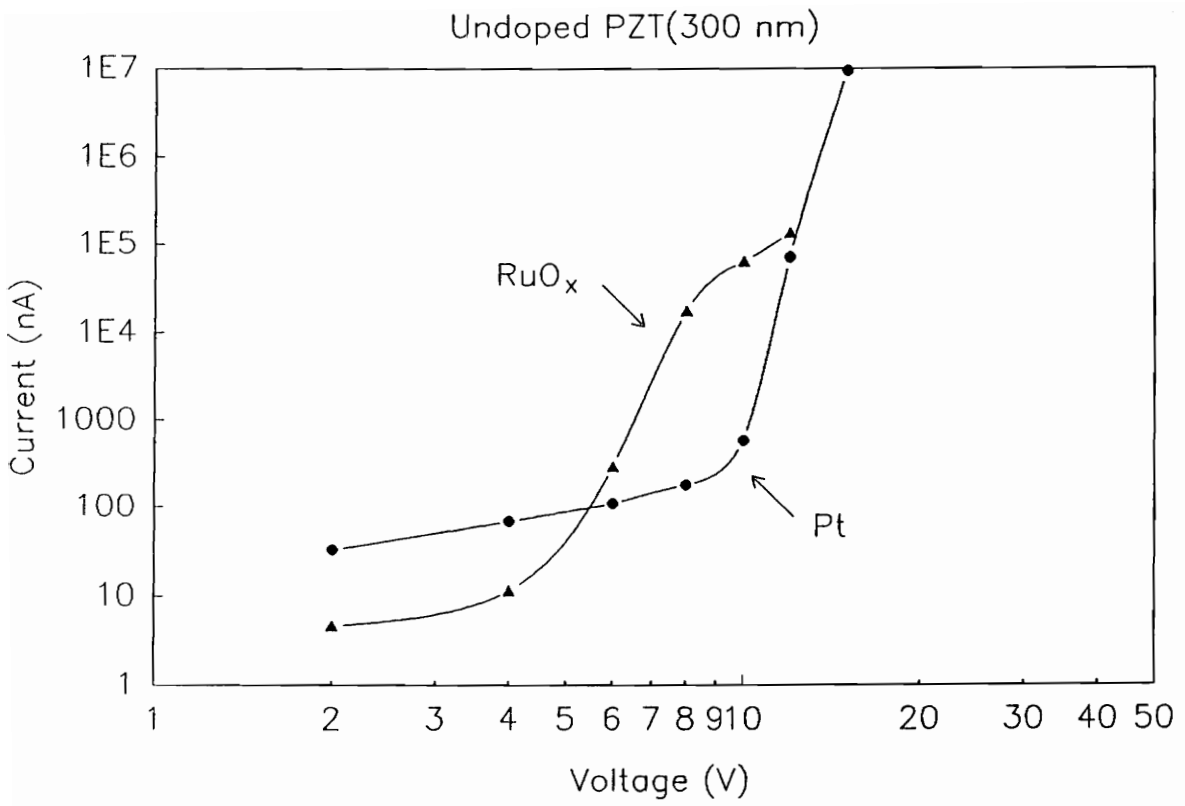


Figure 4.27 Log-log plot of leakage current as a function of applied voltage for PZT films on RuO_x and Pt electrodes annealed at 650°C.

Figures 4.28 compares the hysteresis loops of PZT (50/50) and PLZT (2/50/50) films on Pt electrodes annealed at 550°C with thickness of 300 nm. The higher values of P_r and E_c in PLZT films as compared with undoped PZT films indicates that lanthanum can increase the volume fraction of ferroelectric perovskite phase in PZT films under same annealing conditions. Similar behavior is also observed in Nd-doped PZT films. The decrease in the transformation temperature from pyrochlore to perovskite phase by the addition of La and Nd dopants in PZT films has been confirmed by XRD [50].

The effect of La concentration on ferroelectric properties in PZT films on Pt electrodes with 200 nm thickness, annealed 650°C for 15 minutes, was also investigated [50]. The results obtained from the hysteresis loops measured using applied voltage of 5 volts are listed in Table 4.5. Both saturation polarization (P_{sat}) and remanent polarization (P_r) increases with increasing La concentration, whereas the coercive field (E_c) decreases with increasing La concentration. Similar results have been found in PLZT bulk ceramics [21] and in some MOCVD PLZT thin films [73].

4.7.2.2 Effect on Leakage Current

Figure 4.29 shows the leakage current as a function of voltage for PZT and Nb-doped PZT (2/50/50) films on Pt electrodes annealed at 650°C. The addition of Nb dopants in PZT films is reduced the leakage current by about two orders of magnitude from 900 nA to 50 nA at 10 volts. Similar results are also observed in PLZT films. These dopants (La and Nb) act as compensating donors in

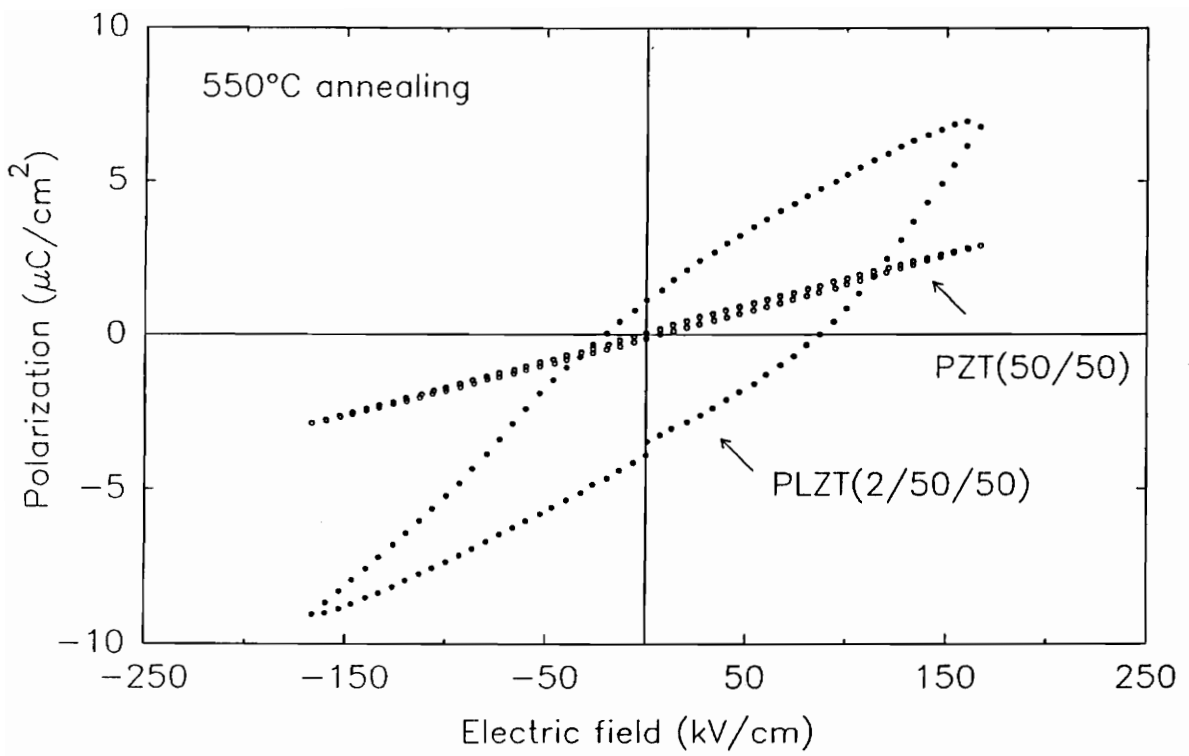


Figure 4.28 Comparison of hysteresis loops in PLZT and PZT films annealed at 550°C .

Table 4.5 A summary of electrical properties for PLZT films.

Compositions	$P_{\text{sat}}(\mu\text{C}/\text{cm}^2)$	$P_r(\mu\text{C}/\text{cm}^2)$	$E_c(\text{kV}/\text{cm})$
PZT (50/50)	12.65	5.17	36.00
PLZT (1/50/50)	19.31	9.62	9.75
PLZT (2/50/50)	23.48	13.14	7.58

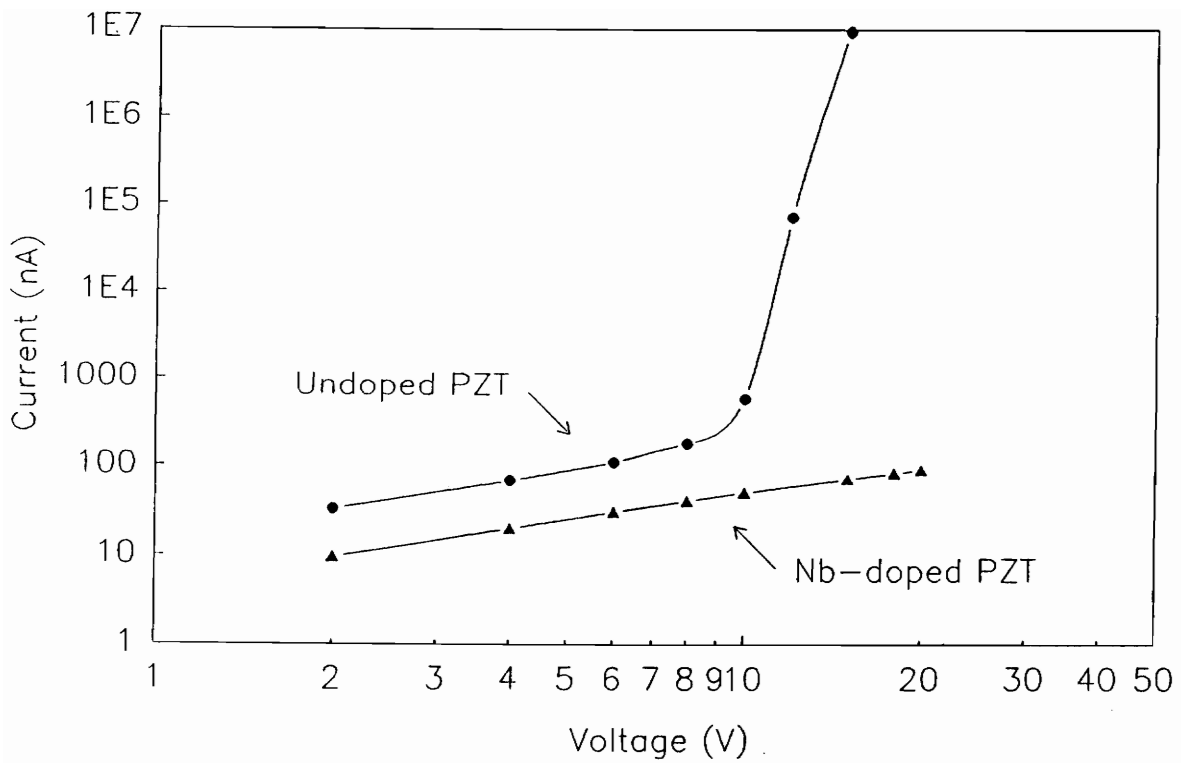


Figure 4.29 Log-log plot of leakage current as a function of voltage for PZT and Nb-doped PZT films.

PZT and PbTiO_3 materials, thereby reducing the p-type conductivity caused by the lead vacancies. The space charge current in vacuum calculated using the Langmuir–Child law for this capacitor configuration is found to be 0.545 nA.

4.7.2.3 Effect on Fatigue Properties

The most significant improvement of the dopant effects on PZT films is the reduction of fatigue rates by the Nb dopants. Usually, after the films were subjected to polarization reversal up to 10^9 cycles it was found that the hysteresis curves change shape corresponding to a decrease in P_r and an increase in E_c . Figures 4.30(a) and (b) compare the hysteresis loops before and after fatigue testing for undoped and Nb-doped PZT films on Pt electrodes, respectively. After 10^9 fatigue cycles, for the undoped PZT films (Figure 4.30(a)), P_r reduces from 25.6 to $12.4 \mu\text{C}/\text{cm}^2$ while E_c increases from 36.7 to 50 kV/cm; for the Nb-doped PZT films (Figure 4.30(b)), P_r reduces from 33.5 to $24.8 \mu\text{C}/\text{cm}^2$ while E_c increases from 49.1 to 53.1 kV/cm.

Figure 4.31 shows the comparison of fatigue properties of undoped and Nb-doped (2 at.%) PZT films on Pt electrodes. The films with thickness of 300 nm were fabricated on Pt electrodes under the same conditions. The measurements were conducted using an alternating pulse with a pulse width of 8.6 μsec , pulse period of 21 μsec and an electric field of 120 kV/cm. These conditions are sufficient to cause complete domain switching in the ferroelectric material during the cycling. A continuous loss in polarization in both undoped and Nb-doped PZT films implies that the fatigue rate increases with increasing number of cycles. The Nb-doped

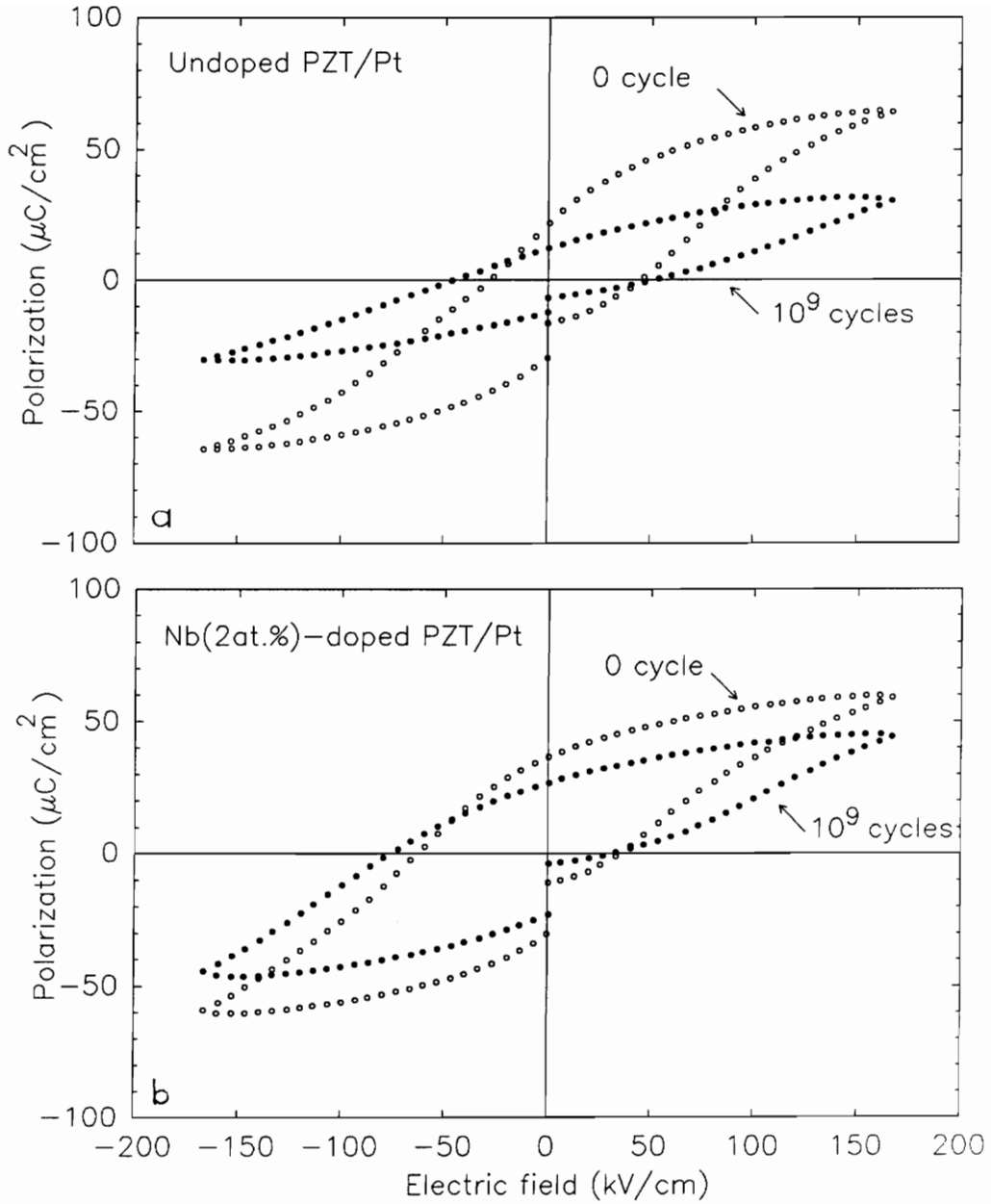


Figure 4.30 Comparison of hysteresis loops before and after fatigue testing for (a) undoped and (b) Nb–doped PZT films on Pt electrodes.

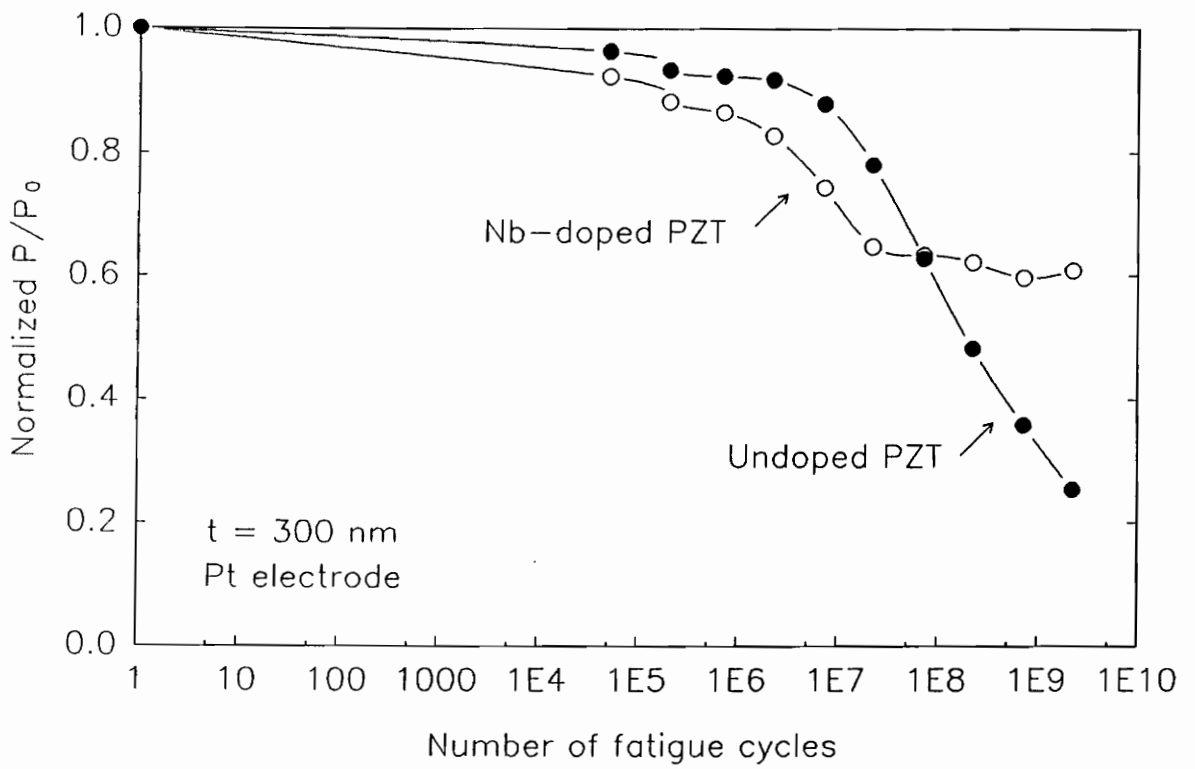


Figure 4.31 Comparison of fatigue properties of undoped and Nb-doped PZT films on Pt electrodes.

PZT films show a continuous initial polarization loss up to 10^7 cycles, beyond which no more loss in polarization is observed while in undoped PZT films the loss in polarization continues all the way up to 10^9 cycles. After 10^9 cycles, for the Nb-doped PZT films 60% of the initial polarization is remaining whereas for undoped PZT films the value reduces to about 25%. In addition, the value of E_c for undoped PZT films increases by about 36%, while for Nb-doped PZT films this increases only 9%. The less increase in E_c can be due to the decrease of oxygen vacancy content in Nb-doped PZT films. Although the initial fatigue rate of Nb-doped PZT films is slightly higher compared to undoped films, the constant fatigue rate after 10^7 cycles as observed in Nb-doped PZT films indicates the endurance and reliability of the PZT films is improved by this compositional modification. It is known that the electrode/ferroelectric interface plays a key role in determining the fatigue properties of the PZT films and the defect entrapment, e.g. oxygen vacancy, at the interface is thought to be the main source of the polarization loss during fatigue. Further, it is believed that introducing Nb dopants into PZT materials can reduce the oxygen vacancy content. Therefore, the improved fatigue properties, e.g. less polarization loss and less E_c increase, in PZT films indicates that defect entrapment can be reduced by the addition of Nb dopants. Other factors such as the densification of structure by the addition of 2 at.% niobium [25,26] can also lead to the improvement in fatigue properties.

4.8 Substrate Effects

The preferred orientation, microstructure and transformation temperature of the films were observed to be a function of the type of substrate used and of the

annealing temperature [50,61,62].

4.8.1 Effect on Preferred Orientation

Table 4.6 summarizes $\{100\}/\{110\}$ x-ray peak height ratio for PLZT and PNZT films, whose dopant concentrations range from 0.0 to 2.0 at.%, heat treated at 700°C for 1 hour on Pt/Ti/SiO₂/Si and sapphire substrates. The $\{100\}/\{110\}$ ratio for films on sapphire substrates was similar to that for films both powder samples from JCPDS (0.12) and for thin films (0.1987) with random grain orientation (Appendix B). The peak height ratio value for thin film with random grain orientation was obtained by using a computer program [74]. In contrast to the films on sapphire substrates, the films on Pt substrates show much greater values for $\{100\}/\{110\}$ ratio indicating $\{100\}$ preferred orientation. Additionally, the $\{100\}/\{110\}$ ratio for the films on Pt substrates increased with increasing annealing temperature as shown in Figure 4.32.

4.8.2 Effect on Microstructure

Figures 4.33(a) and (b) show typical microstructures of PNZT (1/50/50) films on both Pt and sapphire substrates subjected to a final annealing at 700°C for 1 hour. For the heat treatment at 700°C for 1 hour, only the perovskite phase with well-developed microstructure was present for the films on both Pt and sapphire substrates. The x-ray data (Figures 4.34(a) and (b)) also show that the film is entirely perovskite phase with preferred orientation and without detectable pyrochlore or amorphous scattering. However, the grain size of the perovskite film

Table 4.6 {100}/{110} x-ray peak height ratio for PLZT and PNZT films heat treated at 700°C for 1 hour on both Pt and sapphire substrates.

PLZT			
substrate	(0.5/50/50)	(1/50/50)	(2/50/50)
sapphire	0.197	0.201	0.195
Pt/Ti/SiO ₂ /Si	3.652	2.500	8.400

PNZT			
substrate	(0.5/50/50)	(1/50/50)	(2/50/50)
sapphire	0.141	0.209	0.117
Pt/Ti/SiO ₂ /Si	0.241	13.250	5.010

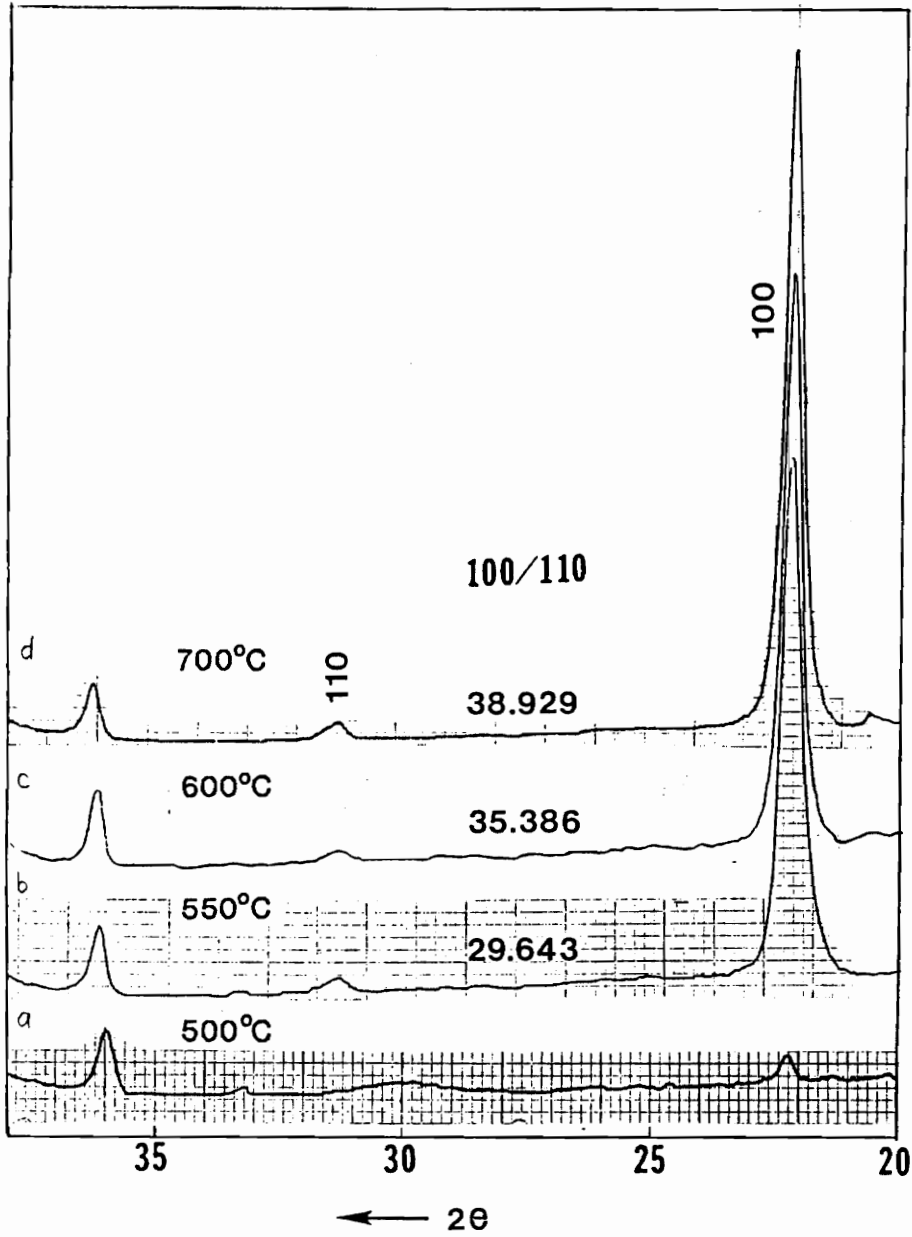


Figure 4.32 $\{100\}/\{110\}$ x-ray peak height ratio for PNZT (1/50/50) films on Pt substrate annealed at (a) 500°C, (b) 550°C, (c) 600°C, and (d) 700°C for 1 hour, respectively.

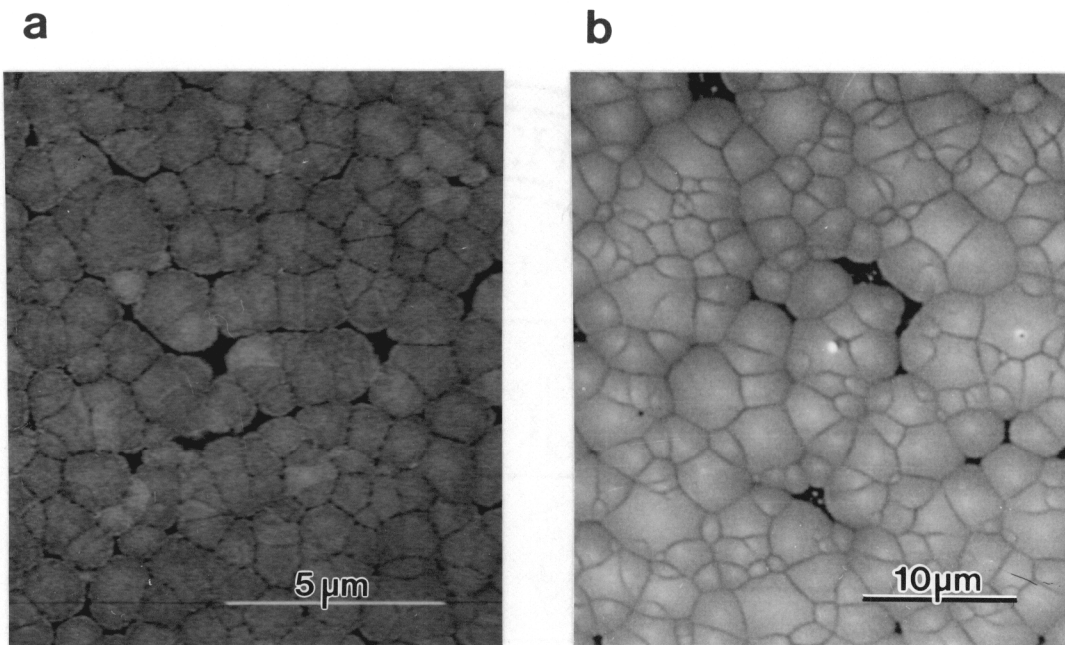


Figure 4.33 Typical microstructure of PNZT (1/50/50) films subjected to a final heat treatment at 700°C for 1 hour (a) on Pt substrate with a combination photograph of scanning electron and backscattering electron images (bar = 5 μm) and (b) on sapphire substrate with a SEM photograph (bar = 10 μm).

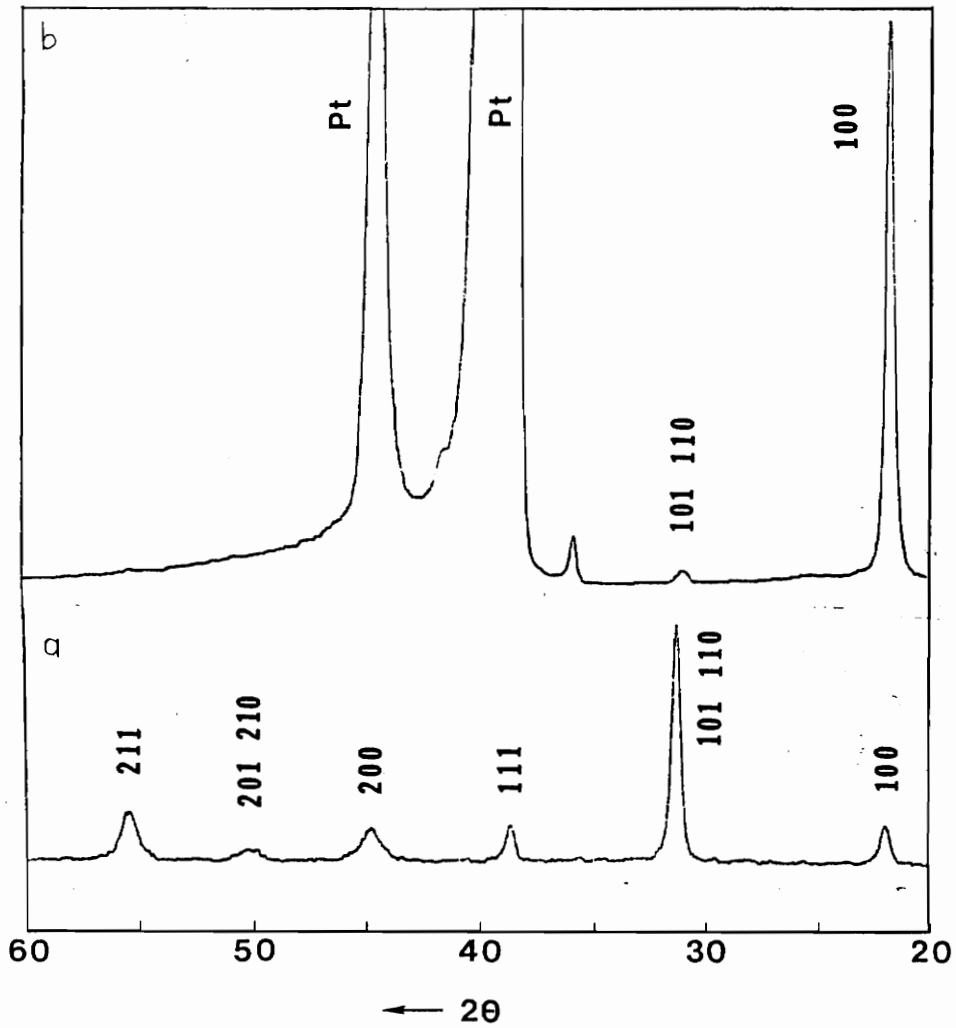


Figure 4.34 X-ray diffraction patterns of PNZT (1/50/50) films, annealed at 700°C for 1 hour, on (a) sapphire and (b) Pt substrates.

on Pt substrate ($0.6 \mu\text{m}$) was about 3 times smaller than that of the film on sapphire ($2 \mu\text{m}$). In addition, the grain size distribution of the film on Pt substrate was more uniform than that of the film on sapphire.

4.8.3 Effect on Transformation Temperature

Figures 4.35(a) and (b) show the x-ray diffraction patterns of PNZT (1/50/50) films, annealed at 500°C for 1 hour, on both Pt and on sapphire substrates, respectively. For the heat treatment at 500°C for 1 hour, both the perovskite and the pyrochlore phases were present in the films on Pt substrate, whereas only the pyrochlore phase was present for the films on sapphire substrate. In other words, the perovskite phase was formed at lower temperatures for the films on Pt substrate than that of the films on sapphire substrates.

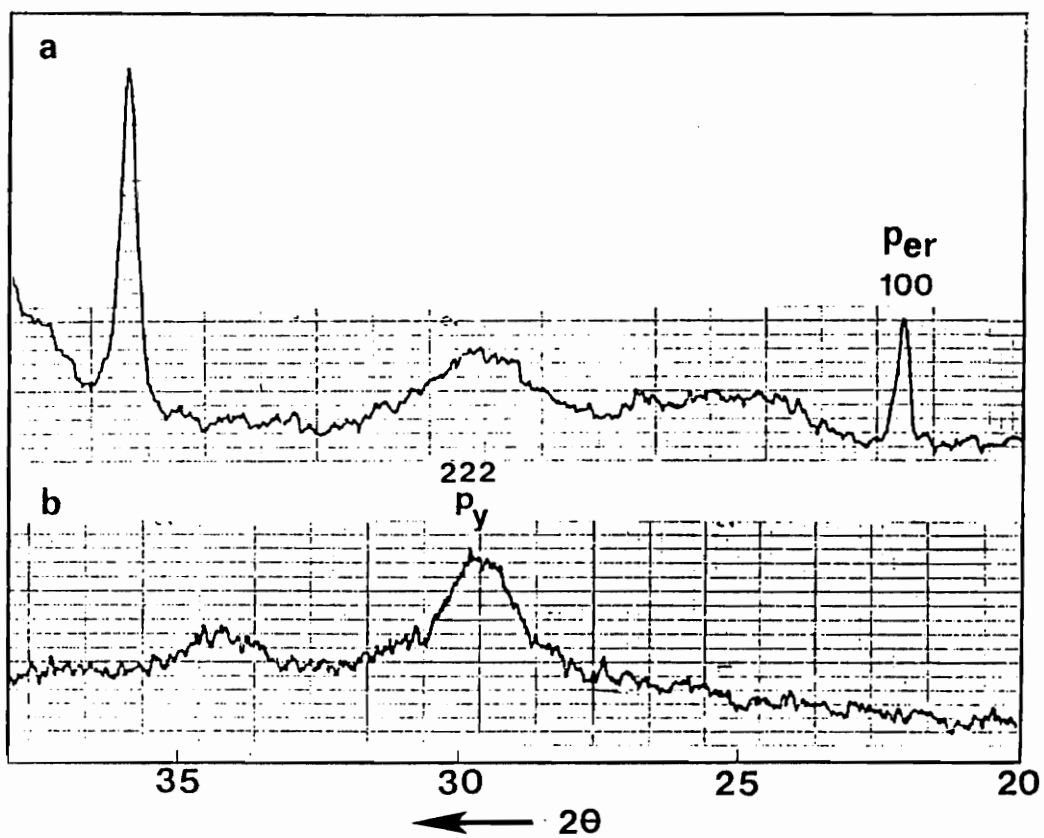


Figure 4.35 X-ray diffraction patterns of PNZT (1/50/50) films, annealed at 500°C for 1 hour, on (a) sapphire and (b) Pt substrates.

Chapter 5: SUMMARY

From the results and discussion given in chapter 4, the following conclusion can be made:

1. A modified MOD process with good composition control was developed and applied to the fabrication of both undoped and doped PZT films. The process parameters such as solution concentration, spin speed, drying temperature, annealing temperature, and heating ramp were studied and suggested in the improvements of film microstructures and properties.
2. The effects of dopants on PZT film properties were:
 - (1) The average grain size of PLZT thin films on sapphire substrates was found to decrease with increasing La concentration while for Nd-doped PZT films the average grain size decreased with Nd content up to 4 at.%, after which the grain size increased.
 - (2) Curie temperature of PLZT and PNZT thin foils decreased with increasing dopant concentration and with decreasing crystal tetragonality. For a given dopant concentration, Curie temperature of Nd-doped PZT films was lower than that that of La-doped PZT films. Generally, Curie temperature of thin foils was found to be less than that of corresponding bulk materials.
 - (3) The value of the crystal tetragonality factor in both PLZT and PNZT thin foils was found to decrease with increasing dopant concentration.

For a given dopant concentration, the crystal tetragonality was lower for Nd-doped PZT films than that of La-doped PZT films.

- (4) Both La and Nd-doped PZT films exhibited higher refractive indices than undoped PZT films. This also implies that the packing densities of PZT films improved by the addition of La and Nd dopants.
 - (6) The transformation temperature from pyrochlore to perovskite phase decreased as result of the addition of La or Nd dopants.
 - (7) With increasing La content, both saturation polarization and remanent polarization increased while the coercive field decreased.
 - (8) The leakage current of PZT films was observed to decrease by the addition of Nb and La dopants.
 - (9) The fatigue properties of PZT films was improved by 2 at.% Nb dopants.
3. The microstructure and preferred orientation of undoped and doped PZT films were observed to be a function of the type of substrate and of the annealing temperature.

APPENDIX A

A.1 Envelope Method

A.1.1 Calculation of Refractive Index (n) and Extinction Coefficient (k)

For a specimen consisting of a weakly-absorbing film on a complete transparent substrate with the conditions of $k^2 \ll (n - n_s)^2$, the transmittance of the specimen is

$$T = \frac{16n_0n_s n^2 A}{C_1^2 + C_2^2 A^2 + 2C_1 C_2 A \cos(4\pi n t / \lambda)} \quad (A1)$$

where

$$C_1 = (n + n_0)(n_s + n)$$

$$C_2 = (n - n_0)(n_s - n)$$

$$A = \exp(-4\pi k t / \lambda)$$

n_0 = refractive index of air

n_s = refractive index of substrate

n = refractive index of film

k = extinction coefficient

t = thickness of film

In equation (A1), at $\cos(4\pi n t / \lambda) = \pm 1$ the equation becomes

$$T_{\max} = 16n_0n_s n^2 A / (C_1 + C_2 A)^2 \quad (A2)$$

$$T_{\min} = 16n_0n_s n^2 A / (C_1 - C_2 A)^2 \quad (\text{A3})$$

From equation (A2) and (A3), solving for A and n

$$A = \{C_1[1 - (T_{\max}/T_{\min})^{0.5}]\} / \{C_2[1 + (T_{\max}/T_{\min})^{0.5}]\} \quad (\text{A4})$$

$$n = [N + (N^2 - n_0^2 n_s^2)^{0.5}]^{0.5} \quad (\text{A5})$$

where $N = 0.5(n_0^2 + n_s^2) + 2n_0n_s (T_{\max} - T_{\min}) / (T_{\max}T_{\min})$

A.1.2 Calculation of Film Thickness

From the interference fringes, the thickness of film can be calculated from the two adjacent peaks or valleys

$$t = \lambda_1 \lambda_2 / 2 [n(\lambda_1)\lambda_2 - n(\lambda_2)\lambda_1] \quad (\text{A6})$$

A.2 Effective Medium Approximation: calculation of Packing Density

$$\sum f_i \frac{\epsilon_i - \epsilon}{\epsilon_i + 2\epsilon} = 0 \quad (\text{A7})$$

where

- n = number of components in the specimen
- f_i = volume fraction of i^{th} component
- ϵ_i = dielectric constant of i^{th} component
- ϵ = measured dielectric function of the specimen

By neglecting the extinction coefficient (k), the refractive index (n) can be related to the dielectric function by $\epsilon = n^2$.

APPENDIX B

33-784

0 0000000
2.0000000

33-783

d	2.87	1.66	2.02	4.15	Pb(Zr _{0.82} Ti _{0.18})O ₃ 5 Lead Zirconium Titanium Oxide																																																																																																																							
1/1 ₁	100	25	16	9																																																																																																																								
Rad. CuKα λ 1.5418 Filter Ni Dia. Cutoff 1/1 ₁ Diffractometer 1/1 cor. Ref. Kakegawa, K. et al., Solid State Commun., 24 769 (1977)					<table border="1"> <thead> <tr> <th>d Å</th> <th>1/1₁</th> <th>hkl</th> <th>d Å</th> <th>1/1₁</th> <th>hkl</th> </tr> </thead> <tr> <td>4.146</td> <td>9</td> <td>001</td> <td>1.176</td> <td>5</td> <td>222</td> </tr> <tr> <td>4.036</td> <td>12</td> <td>100</td> <td>1.14</td> <td rowspan="3">4</td> <td>203</td> </tr> <tr> <td>2.89</td> <td rowspan="2">100</td> <td>101</td> <td>1.13</td> <td>302</td> </tr> <tr> <td>2.85</td> <td>110</td> <td>1.12</td> <td>320</td> </tr> <tr> <td>2.351</td> <td>15</td> <td>111</td> <td>1.10</td> <td rowspan="3">15</td> <td>123</td> </tr> <tr> <td>2.073</td> <td>9</td> <td>002</td> <td>1.09</td> <td>312</td> </tr> <tr> <td>2.018</td> <td>16</td> <td>200</td> <td>1.08</td> <td>321</td> </tr> <tr> <td>1.844</td> <td>5</td> <td>102</td> <td>1.0366</td> <td><1</td> <td>004</td> </tr> <tr> <td>1.81</td> <td>6</td> <td>201,210</td> <td>1.0091</td> <td><1</td> <td>400</td> </tr> <tr> <td>1.677</td> <td>12</td> <td>112</td> <td>1.004</td> <td><1</td> <td>104</td> </tr> <tr> <td>1.655</td> <td>25</td> <td>211</td> <td>0.9928</td> <td><1</td> <td>223</td> </tr> <tr> <td>1.446</td> <td>9</td> <td>022</td> <td>.9851</td> <td>1</td> <td>322</td> </tr> <tr> <td>1.427</td> <td>5</td> <td>220</td> <td>.9743</td> <td>2</td> <td>114</td> </tr> <tr> <td>1.382</td> <td>2</td> <td>003</td> <td>.9641</td> <td>2</td> <td>303</td> </tr> <tr> <td>1.361</td> <td rowspan="2">6</td> <td>212</td> <td>.953</td> <td rowspan="2">4</td> <td>411</td> </tr> <tr> <td>1.35</td> <td>221,300</td> <td>.951</td> <td>330</td> </tr> <tr> <td>1.308</td> <td>6</td> <td>103</td> <td>.9377</td> <td>1</td> <td>133</td> </tr> <tr> <td>1.28</td> <td>9</td> <td>301,310</td> <td>.9273</td> <td><1</td> <td>331</td> </tr> <tr> <td>1.244</td> <td>2</td> <td>113</td> <td>.9221</td> <td>2</td> <td>204</td> </tr> <tr> <td>1.220</td> <td>2</td> <td>311</td> <td colspan="3">11 reflections to 0.821</td> </tr> </table>	d Å	1/1 ₁	hkl	d Å	1/1 ₁	hkl	4.146	9	001	1.176	5	222	4.036	12	100	1.14	4	203	2.89	100	101	1.13	302	2.85	110	1.12	320	2.351	15	111	1.10	15	123	2.073	9	002	1.09	312	2.018	16	200	1.08	321	1.844	5	102	1.0366	<1	004	1.81	6	201,210	1.0091	<1	400	1.677	12	112	1.004	<1	104	1.655	25	211	0.9928	<1	223	1.446	9	022	.9851	1	322	1.427	5	220	.9743	2	114	1.382	2	003	.9641	2	303	1.361	6	212	.953	4	411	1.35	221,300	.951	330	1.308	6	103	.9377	1	133	1.28	9	301,310	.9273	<1	331	1.244	2	113	.9221	2	204	1.220	2	311	11 reflections to 0.821		
d Å	1/1 ₁	hkl	d Å	1/1 ₁	hkl																																																																																																																							
4.146	9	001	1.176	5	222																																																																																																																							
4.036	12	100	1.14	4	203																																																																																																																							
2.89	100	101	1.13		302																																																																																																																							
2.85		110	1.12		320																																																																																																																							
2.351	15	111	1.10	15	123																																																																																																																							
2.073	9	002	1.09		312																																																																																																																							
2.018	16	200	1.08		321																																																																																																																							
1.844	5	102	1.0366	<1	004																																																																																																																							
1.81	6	201,210	1.0091	<1	400																																																																																																																							
1.677	12	112	1.004	<1	104																																																																																																																							
1.655	25	211	0.9928	<1	223																																																																																																																							
1.446	9	022	.9851	1	322																																																																																																																							
1.427	5	220	.9743	2	114																																																																																																																							
1.382	2	003	.9641	2	303																																																																																																																							
1.361	6	212	.953	4	411																																																																																																																							
1.35		221,300	.951		330																																																																																																																							
1.308	6	103	.9377	1	133																																																																																																																							
1.28	9	301,310	.9273	<1	331																																																																																																																							
1.244	2	113	.9221	2	204																																																																																																																							
1.220	2	311	11 reflections to 0.821																																																																																																																									
Sys. Tetragonal S.G. a ₀ 4.036 b ₀ c ₀ 4.146 A C 1.027 α β γ Z [1] Dx[8.006] Ref. Ibid.																																																																																																																												
εα nωβ εγ Sign 2V D mp Color Pale yellow Ref. Ibid.																																																																																																																												
No compositional fluctuation. Si used as internal standard (a ₀ = 5.4301Å).																																																																																																																												

FORM M-2

REFERENCE

1. S. Dey and R. Zuleeg, "Integrated Sol-Gel PZT Thin Films on Pt, Si, and GaAs for Nonvolatile Memory Applications," *Ferroelectrics*, 108 37-46 (1990).
2. D. Bondurant and F. Gnadinger, "Ferroelectrics for Nonvolatile RAM," *IEEE Spec.*, 30-33 (1989).
3. C. D. Land, P. D. Thatcher, and G. H. Haertling, "Electrooptic Ceramics," in *Appl. Solid State Sci.*, 4 240-243, R. Wolfe, Ed. Academic, New York (1974)
4. G. H. Haertling, "Ferroelectric Thin Films for Electronic Applications," *J. Vac. Sci. Technol.*, A9 (3) 414-420 (1991),
5. M. Oikawa and K. Toda, "Preparation of Pb(Zr,Ti)O₃ Thin Films by an Electron Beam Evaporation Technique," *Appl. Phys. Lett.*, 29 491-492 (1976).
6. S. Krupanidhi, N. Maffei, M. Sayer, and K. El-Assal, "rf Planar Magnetron Sputtering and Characterization of Ferroelectric Pb(Zr,Ti)O₃ Films," *J. Appl. Phys.* 54 (11) 6601-6609 (1983).
7. R. Castellano, "Deposition of Thin Films of PZT by A Focus Ion Beam Sputtering Technique," *Ferroelectrics*, 28 387-389 (1980).
8. C. Chiang, C. Cook, P. Schenck, P. Brody, and J. Benedetto, "Lead Zirconate Titanate Thin Films Prepared by The Laser Ablation Technique," *Mat. Res. Soc. Symp. Proc.*, 200 133-137 (1991).
9. J. K. Saenger, R. Rpy, K. Etzold, and J. Cuomo, "lead Zirconate Titanate

- Films Produced by Pulse Laser Deposition," *Mat. Res. Soc. Symp. Proc.*, 200 115–200 (1991).
10. C. H. Peng and S. B. Desu, "Low-Temperature Metallorganic Chemical Vapor Deposition of Perovskite $\text{Pb}(\text{Zr}_x\text{Ti}_{1-x})\text{O}_3$ Thin Films, *Appl. Phys. Lett.*, 61 (1) 1–4 (1992).
 11. Y. Sakashita, T. Ono, and H. Segawa, "Preparation and Electrical Properties of MOCVD-Deposited PZT Thin Films, *J. Appl. Phys.*, 69 (12), 8352–8357 (1991).
 12. K. D. Budd, S. K. Dey, and D. A. Payne, "Sol-Gel Processing of PbTiO_3 , PbZrO_3 , PZT and PLZT Thin Films," *Proc. Brit. Cerm. Soc.*, 36 107–122 (1985).
 13. J. Fukushima, K. Kodaira and T. Marsushita, "Preparation of Ferroelectric PZT films by Thermal Decomposition of Organometallic Compounds," *J. Mater. Sci.*, 19 595–598 (1984).
 14. J. V. Mantese, A. L. Micheli, A. H. Hamdi, and R. W. Vest, "Metalorganic Deposition (MOD): A Nonvacuum, Spin-on, Liquid-Based, Thin Film Method," *MRS Bull.* 10 48–53 (1989).
 15. C. W. Turner, "Sol-Gel—Principles and Applications," *Ceram. Bull.*, 70 (9) 1487–1490 (1991).
 16. J. Blum, "Electronic Ceramics Made by the Sol-Gel Process," in *Sol-Gel Technology for Thin Films, Fibers, Preforms, Electronics, and Special Shapes*, 292–306, L. Klien, Ed., Noyes Publications, New Jersey (1988).
 17. G. Yi, A. Wu, and M. Sayer, "Preparation of $\text{Pb}(\text{Zr,Ti})_3$ Thin Films by Sol-Gel Processing: Electrical, Optical, and Electro-optic Properties," *J. Appl. Phys.*, 64 (5) 2717–2724 (1988).

18. C. K. Kwok, D. P. Vijay, S. B. Desu, N. R. Parikh, and E. A. Hill, "Conducting Oxide Electrodes for Ferroelectric Films," ISIF 92, in press.
19. G. Yi and M Sayer, "Sol-Gel Processing of Complex Oxide Films," *Ceram. Bull.*, **70** (7) 1173-1179 (1991).
20. C. K. Kwok, "Processing-Structure-Property Interrelationships of Ferroelectric Thin Films with Emphasis on Formation Kinetics," Ph.D. Dissertation, Virginia Polytechnic Institute and State University (1992).
21. B. Jaffe, W. R. Cook, Jr., and J. Jaffe, in *Piezoelectric Ceramics*, 115-181, Academic Press, New York (1971).
22. Y. Wu, in *Ferroelectric Materials and Their Application*, 101-159, North-Holland, New York (1991).
23. G. H. Haertling, "Piezoelectric and Electrooptic Ceramics," in *Ceramic Materials for Electronics: Processing, Properties, and Applications*, 130-225, R. C. Buchanan, Ed., Marcel Dekker, New York (1986).
24. R. P. Tandon, V. Singh, and N. N. Swami, "Dielectric and electromechanical Properties of Lead Zirconate Titanate Ceramics Containing Neodymium Ions," *J. Mat. Soc. Lett.*, **11**, 327-329 (1992).
25. A. H. Carim, B. A. Tuttle, D. H. Doughty, and S. L. Martinez, "Microstructure of Solution-Processed Lead Zirconate Titanate (PZT) Thin Films," *J. Am. Ceram. Soc.*, **74** [6], 1455-58 (1991).
26. E. M. Griswold, M. Sayer, D. T. Amm, and I. D. Calder, "The Influence of Niobium-Doping on lead Zirconate Titanate Ferroelectric Thin Films," *Can. J. Phys.*, **69**, 260 (1990).
27. J. F. Scott, C. A. Araujo, B. M. Melnick, L. D. McMillan, and R. Zuleeg, "Quantitative Measurement of Space-Charge Effects in Lead

- Zirconate–Titanate Memories," *J. Appl. Phys.* 70 [1], 382–388 (1991).
28. B. M. Melnick, C. A. Paz de Araujo, M. C. Scott, L. D. McMillan, "Anomalous Fatigue Free Behavior in Zn Doped PZT," ISIF 92, in press.
 29. E. K. W. Goo, R. K. Mishra, and G. Thomas, "Electron Microscopy Study of Ferroelectric Domains and Domain Wall Structure in $\text{PbZr}_{0.52}\text{Ti}_{0.48}\text{O}_3$," *J. Appl. Phys.*, 52 (4) 2941–2943 (1980).
 30. M. L. A. Dass, U. Dahman and G. Thomas, "Electron Microscopy Characterization of Lead Zirconate Titanate Ceramics at the Morphotropic Phase Boundary Composition," *Proc. 6th. IEEE Int. Symp. on Appl. of Ferroelectric (ISAF)*, 146–149, Bethlehem, PA (1986).
 31. C. K. Kwok and S. B. Desu, "Pyrochlore to Perovskite Phase Transformation in Sol–Gel Derived Lead–Zirconate–Titanate Thin Films," *Appl. Phys. Lett.* 60 (12), 1430–1432 (1992).
 32. K. D. Budd, "Structure Evolution in Sol–Gel–Derived Lead Titanate Materials, and Applications to the Processing of Thin Dielectric Layers," Ph.D. Dissertation, University of Illinois at Urbana–Champaign (1986).
 33. L. H. Parker and A. F. Tasch, "Ferroelectric Materials for 64 Mb and 256 Mb DRAMs," *IEEE Circuit and Devices*, 17–26 Jan. (1990).
 34. W. D. Kingery, H. K. Bowen and D. R. Uhlmann, in *Introduction to Ceramics*, 237–279, J. Wiley & Son Co. (1976).
 35. F. S. Galasso, "Structure, Properties and Preparation of Perovskite–Type Compounds," Pergamon Press, New York (1969).
 36. Powder Diffraction File, Inorganic Phase, JCPDS (International Center for Diffraction Data, Swarthmore, PA 1986) #33–784.
 37. J. M. Herbert, "Ceramic Dielectrics and Capacitors," 128–187, Gordon &

- Breach Sci. Publishers (1985).
38. C. K. Kwok and S. B. Desu, "Transmission Electron Microscopy Study of PZT Films," *Ceram. Trans.: Ferroelectric Films*, 25, A. Bhalla, ed., ACS, Westerville, OH, 85–94 (1992).
 39. P. G. Lucuta and V. Teodorescu, "SEM, SAED and TEM Investigations of Domain Structure in PZT Ceramics at Morphotropic Phase Boundary," *Appl. Phys.*, A37 237–242 (1985).
 40. P. G. Lucuta, "Ferroelectric–Domain Structure in Piezoelectric Ceramics," *J. Am. Ceram. Soc.*, 72 (6) 933–937 (1989).
 41. B. G. Demczyk, R. S. Rai, and G. Thomas, "Ferroelectric Domain Structure of Lanthanum–Modified Lead Titanate Ceramics," *J. Am. Ceram. Soc.*, 73 (3) 615–620 (1990).
 42. G. Arlt and P. Sasko, "Domain Configuration and Equilibrium Size of Domains in BaTiO₃ Ceramics," *J. Appl. Phys.*, 51 (9) 4956–4960 (1980).
 43. A. G. Khachaturyan, *Theory of Structural Transformations in Solid*, 368–401, Wiley, New York (1983).
 44. H. M. Duiker, P. D. Beale, J. F. Scott, C. A. Araujo, B. M. Melnick, J. D. Cuchiaro, and L. D. McMillan, "Fatigue and Switching in Ferroelectric Memories: Theory and Experiment," *J. Appl. Phys.*, 68 (11) 5783–5791 (1990).
 45. I. Yoo and S. B. Desu, "Fatigue Modeling of Lead Zirconate Titanate Thin Films," *Mat. Sci. Eng.*, B13 319–322 (1992).
 46. R. Moazzami, C. Hu, and W. H. Shepherd, "A Ferroelectric DRAM Cell for High–Density NVRAM's," *IEEE Elec. Device Lett.*, 11 (10) 454–457 (1990).
 47. G. H. Haertling and C. E. Land, "Hot Pressed (Pb,La)(Zr,Ti)O₃

- Ferroelectric Ceramics for Electrooptic Applications," *J. Am. Ceram. Soc.*, **54** [1] 1–10 (1971).
48. B. A. Tuttle, D. H. Doughty, R. W. Schwartz, T. J. Garino, S. L. Martinez, D. Goodnow, C. L. Hernandez, R. G. Tissot, and W. F. Hammetter, "Chemical Prepared PZT Films with Niobium Additions," *Ceram. Trans.: Microelectronic Systems*, **15** 179–191 (1990).
49. S. S. Chandratreya, R. M. Fulrath, and F. A. Pask, "Reaction Mechanisms in the Formation of PZT Solid Solutions," *J. Am. Ceram. Soc.*, **68** (11) 422–425 (1981).
50. J. F. Chang and S. B. Desu, "Characterization of MOD PLZT and PNZT Films," *Ceram. Trans.: Ferroelectric Films*, **25**, A. Bhalla, et., ASC, Westerville, OH, 155–167 (1992).
51. K. D. Budd, S. K. Dey, and D. A. Panye, "The Effect of Hydrolysis Conditions on the Characteristics of PbTiO_3 Gels and Thin Films," *Mat. Res. Soc. Symp. Proc.*, **72** 317–323 (1986).
52. R.W. Schwartz, R. A. Assink, and T. J. Headley, "Spectroscopic and Microstructural Characterization of Solution Chemistry Effects in PZT Thin Film Processing," *Mat. Res. Soc. Symp.*, Vol. 243 (1991), in press.
53. A. S. Shailh and G. M. Vest, "Kinetics of PbTiO_3 Formation from Metallo–organic Precursors," *J. Am. Ceram. Soc.*, **69** (9) 682–688 (1986).
54. R. Jones, *Fundamental Principles of Sol–Gel Technology*, Institute of Metal, London (1989).
55. D. C. Bradley, "Meatal Alkoxides as Precursors for Electronic and Ceramic Materials," *Chem. Rev.*, **89** 1317–1322 (1989).
56. S. D. Tamamurthi and D. A. Payne, "Structural Investigation of

- Prehydrolyzed Precursors Used in the Sol–Gel Processing of Lead Titanate," *J. Am. Ceram. Soc.*, 73 (8) 422–425 (1990).
57. T. W. Dekleva, J. M. Hayes, L. E. Cross, and G. L. Geoffroy, "Sol–Gel Processing of Lead Titanate in 2–Methoxyethanol: Investigation into the Nature of the Prehydrolyzed Solutions," *J. Am. Ceram. Soc.*, 71 (5) C280–C282 (1988).
 58. R. Schwartz, B. Bunker, D. Dimos, R. Assink, B. Tuttle, and I. Weinstock, "Solution Chemistry Effect in $\text{Pb}(\text{Zr},\text{Ti})\text{O}_3$ Thin Film Processing," *Ferroelectrics*, preprint (1991).
 59. C. H. Peng and S. B. Desu, "Investigation of Structure Development in MOD $\text{Pb}(\text{Zr},\text{Ti})\text{O}_3$ Films by an Optical Method," *Mat. Res. Soc. Symp. Proc.*, Vol. 243 (1992), in press.
 60. B. A. Tuttle, R. W. Shwartz, D. H. Doughty, and J. A. Voigt, "Characterization of Chemically Prepared PZT Thin Films," *Mat. Res. Soc. Symp.*, 200 159–165 (1990).
 61. N. Tohge, S. Talahashi, and T. Minami, "Preparation of PbZrO_3 – PbTiO_3 Ferroelectric Thin Films by the Sol–Gel Process," *J. Am. Ceram. Soc.*, 74 (1) 67–71 (1991).
 62. Y. Xu, C. J. Chen, R. Xu, and J. D. Mackenzie, "The Self–Biased Heterojunction Effect of Ferroelectric Thin Film on Silicon Substrate," *J. Appl. Phys.*, 67 (6) 2985–2991 (1990).
 63. D. E. Bornside, C. W. Macosko, and L. E. Scriven, "Spin Coating of a PMMA/Chlorobenzene Solution," *J. Electrochem. Soc.*, 138 (1) 317–320 (1991).
 64. R. A. Lipeles, N. A. Ives, and M. S. Leung, "Sol–Gel Processig of Lead

- Zirconate Titanate Films," in *Ultrastructure Processing of Advanced Ceramics*, 320–326, J. Mackenzie, Ed., Wiley, New York, (1986).
65. S. B. Desu, C. Peng, L. Kammerdiner, and P. Schuele, "Size Effects in Sputtered PZT Thin Films," *Mat. Res. Soc. Symp. Proc.*, Vol. 200, 319–214 (1990).
 66. C. K. Kwok and S. B. Desu, "Effect of Thermal Processing Conditions on Ferroelectric PZT Thin Films," *Mat. Res. Soc. Symp. Proc.*, Vol. 200, 83–89 (1990).
 67. G. Spierings, M. Ulenaers, G. Kampschoer, H. van Jal, and P. Larsen, "Preparation and Ferroelectric Properties of $\text{PbZr}_{0.53}\text{Ti}_{0.47}\text{O}_3$ Thin Films by Spin Coating and Metalorganic Decomposition," *J. Appl. Phys.*, 70 (4), 2290–2297 (1991).
 68. B. G. Demczyk, "Domain Structure of Lanthanum Modified Lead Titanate Ceramics," M. S. Thesis, University of California at Berkeley (1985).
 69. T. R. Gururaja, S. Kumarakrishnan and E. C. Subbarao, "Modified PLZT High Voltage Dielectrics," *Ferroelectrics*, 27 277–280 (1980).
 70. T. Yamamoto, H. Igarashi, and K. Okazaki, "Dielectric Electromechanical, Optical, and Mechanical Properties of Lanthanum–Modified Lead Titanate Ceramics," *J. Am. Ceram. Soc.*, 66 (5) 363–366 (1983).
 71. P. D. Thacher, "Refractive Index and Surface Layers of Ceramic $(\text{Pb},\text{La})(\text{Zr},\text{Ti})\text{O}_3$ Compounds," *Applied Optics*, 16 (12) 3210–3213 (1977).
 72. H. Kay and J. Dunn, "Thickness Dependence of the Nucleation Field of Triglycine Sulfate," *Phil. Mag.*, 7 2027 (1962).
 73. M. Okada and K. Tominaga, "Preparation and Properties of PLZT Thin Films by MOCVD," ISIF 92, in press.

74. K. E. Wiedemann, "Diffusion of Oxygen and Nitrogen in Titanium and the Use of Ti_3Al as an Oxidation Inhibitor," M.S. Thesis, Virginia Polytechnic Institute and State University (1983).

VITA

Jhing–Fang Chang was born in 1967 and raised in Taipei, Taiwan. She entered National Taipei Institute of Technology in Taipei, Taiwan in 1982 and received her diploma in Metallurgical Engineering in 1987. Thereafter, she joined National Tsing Hua University as a research assistant; in the mean time, she successfully passed the 1987 High Examination for Civil Service in Metallurgical Engineering. In 1988, she was appointed by the ROC government and then joined one of the Taiwan provincial institutes, Tang Eng Iron Works, Inc., as an assistant engineer. In 1989, she received the certificate of qualification for civil service appointment from Examination Ministry of ROC. Later, she joined National Taiwan University as a research assistant in electron microscopy laboratory.

In August 1990, she entered the Department of Materials Science and Engineering at Virginia Polytechnic Institute and State University and started her master research under the supervision of Dr. S. B. Desu. She had two published articles in the field of ferroelectric films.

She is a member of Materials Research Society and American Ceramic Society.